

The Pennsylvania State University
The Graduate School
College of Engineering

**HYPERThERMAL OXIDATION AND PYROLYSIS OF CARBON BASED
MATERIALS: CHEMISTRY AND DYNAMICS USING THE ReaxFF REACTIVE
FORCE FIELD**

A Dissertation in
Mechanical Engineering
by
Sriram Goverapet Srinivasan

© 2014 Sriram Goverapet Srinivasan

Submitted in Partial Fulfillment
of the requirements
for the Degree of

Doctor of Philosophy

December 2014

The dissertation of Sriram Goverapet Srinivasan was reviewed and approved* by the following:

Adri C T van Duin

Associate Professor of Mechanical Engineering

Dissertation Adviser

Chair of Committee

Zoubeida Ounaies

Associate Professor of Mechanical Engineering

Randy L. Vander Wal

Professor of Energy and Mineral Engineering and Materials Science and Engineering

Lasse Jensen

Associate Professor of Chemistry

Daniel Haworth

Professor of Mechanical Engineering

Professor-In-Charge of MNE Graduate Programs

Department of Mechanical and Nuclear Engineering

*Signatures are on file in the Graduate School

ABSTRACT

The primary focus of this work was to study the chemistry and dynamics of hyperthermal collisions of oxygen atoms with carbon based materials of the kind witnessed in the Low Earth Orbit (LEO) environment and their pyrolysis through atomistic simulations using the ReaxFF reactive force field and to develop ReaxFF potentials for such applications. In particular, ReaxFF was used to study the oxidative erosion of graphene, graphite and diamond subjected to collisions with energetic oxygen atoms at elevated surface temperatures. Prior to these simulations, the ReaxFF C/H/O potential was validated against quantum chemical (QC) data for the energetics associated with the loss of a CO₂ molecule from a model graphitic system and for various other chemical reactions occurring during the collision of a hyperthermal oxygen atom with a pristine and defective graphene sheet and a diamond slab. ReaxFF based simulations suggested that the breakup of a graphene sheet and graphite structure upon hyperthermal oxygen atom impact could be divided into distinct regimes. Graphene erosion proceeded through the formation of epoxides on the surface followed by the creation and growth of vacancy defects while the breakup of graphite occurred through the formation of epoxides on the top layer, creation and growth of vacancy defects on the top layer followed by epoxide formation on the bottom layer, creation of defects and their growth on the bottom layer. As such the breakup of graphite was observed to be a layer by layer event with the rate of growth of defects much larger along the basal plane directions compared to the axial direction. With increase in temperature, the rate of mass loss from graphite was observed to increase. While the impact of the oxygen atoms occurred at hyperthermal energies, the chemical reactions leading to mass loss from graphite were thermal in nature. Furthermore, molecular dynamics simulations of carbon loss from graphite at various surface temperatures upon hyperthermal oxygen atom collisions were used to obtain an Arrhenius type rate law for the carbon atom loss rate under such conditions. Further, the direction dependent etching properties of graphite exposed to hypothermal atomic oxygen collisions were also investigated. These simulations revealed that graphite basal planes are poorly resistant to energetic oxygen atom etching while the armchair and zigzag edge surfaces are an order of

magnitude more resistant to energetic oxygen atom etching. To compare the response of diamond surfaces with graphite, energetic oxygen atom etching of low index diamond surfaces namely, diamond (100), diamond (111) and diamond (110) were carried out at various surface temperatures using the ReaxFF C/H/O potential. ReaxFF simulations on small oxygen terminated diamond slabs indicated that a variety of functional groups such as ethers, peroxides, oxy radicals and dioxetanes can form on the surface, in agreement with earlier experiments and first principles based calculations. Successive oxygen collisions on larger reconstructed diamond surfaces showed that all the low index surfaces can be etched by hyperthermal atomic oxygen with diamond (100) showing the lowest etching rate and diamond (110) presenting the largest etching rate. The erosion yield of these surfaces is in good agreement with experimental results. The simulations performed here have been used to obtain an Arrhenius type rate law for the mass loss from these surfaces under such conditions. Although diamond surfaces can be etched by energetic oxygen atoms, they were found to be more than two orders of magnitude more resistant to oxidative erosion as compared to graphite basal planes. These simulations suggest that diamond thin films are promising materials for the surface of space crafts exposed to LEO conditions and in general, the ability of ReaxFF to be used as an effective tool to screen or characterize materials for applications in extreme environments.

In order to study the interaction of hyperthermal atomic oxygen with silica surfaces, a widely used material for the thermal protection system of high speed aircrafts, the ReaxFF_{SiO} potential was extended to describe oxygen – silica gas surface interactions by harvesting model clusters representative of a reconstructed (001) silica surface and surface defects on silica, obtaining density functional theory (DFT) based potential energy curves for the approach of an atomic and molecular oxygen to these clusters followed by re-parametrization of the ReaxFF_{SiO} potential against this data. The new potential, ReaxFF_{SiO}^{GSI}, can be employed for accurate molecular dynamics simulations of oxygen – silica gas surface interactions.

The thermal fragmentation of a large fullerene molecule was studied through molecular dynamics simulations in order to understand the mechanisms underlying the pyrolysis of carbon based materials. While the performance of the ReaxFF C/H/O potential for the chemistry of graphite and diamond oxidation was very good, its description of the mechanical deformation of carbon condensed phases was not satisfactory. Thus ReaxFF C/H/O was re-parameterized against DFT data for the equation of state of graphite, diamond, the formation energies of defects in graphene and amorphous carbon phases from fullerenes. The newly developed ReaxFF potential (ReaxFF_{C-2013}) was used in the molecular dynamics simulation of the thermal fragmentation of a C₁₈₀ molecule. The simulations indicated that the thermal fragmentation of these giant fullerenes can be classified into two distinct regimes – an exponential regime followed by a linear regime. In the initial exponential regime, the molecule shrinks in size but retains the cage like structure while in the final linear regime, the cage opens up into an amorphous phase, resulting in an acceleration of the decay process. Arrhenius parameters for the decay of the molecule in both the regimes were obtained by carrying out simulations at various temperatures. While the decay of the molecule occurred primarily via the loss of C₂ units, with increase in temperature, the probability of loss of larger fragments was found to increase. The newly developed potential along with the methods used in this study can readily be extended towards the full computational chemical modeling of the high temperature erosion of graphitic rocket nozzles and ablation of carbon based spacecraft materials during atmospheric reentry.

Finally, to explore the possibility of developing carbon based materials resistant to oxidative erosion through the impact of hyperthermal oxygen atoms, oxygen interaction with boron doped graphene was considered. Model clusters representative of boron doped graphene were used to obtain DFT based potential energy curves for the approach of an atomic oxygen to these clusters. This dataset can now be used to parameterize ReaxFF to describe oxygen – boron doped graphene gas surface interactions.

The research work reported in this dissertation lays out a clear strategy to develop a ReaxFF reactive potential and to apply it to study the oxidative degradation and pyrolysis of materials subjected to

extreme conditions. Further it provides a straightforward way to extract Arrhenius type parameters from molecular dynamics simulations for the erosion of materials under such conditions. These parameters can be used directly in mesoscale simulation schemes such as Direct Simulation Monte Carlo (DSMC), thereby providing the vital link between atomic scale and macro scale in bottoms up materials design approach.

Contents

List of Figures.....	viii
List of Tables	xiii
Acknowledgement	xiv
1 Introduction.....	1
2 ReaxFF Reactive Force Field	4
3 Graphene / Graphite Oxidation	5
3.1 Introduction	5
3.2 Force Field Validation	7
3.3 Molecular Dynamics Simulations.....	11
3.4 Results and Discussions	15
3.5 Summary.....	26
4 Direction dependent oxidative etching of diamond	28
4.1 Introduction	28
4.2 Computational Methods and Details	30
4.3 Results and Discussions	33
4.4 Summary.....	49
5 Development of ReaxFF – SiO/GSI for Oxygen–Silica Gas Surface Interactions	51
4.1 Introduction	51
4.2 Gas – Surface Model Systems and DFT based Binding Energy Curves.....	52
4.3 Retraining ReaxFF reactive force field	54
4.4 Results and Discussions	57
4.5 Summary.....	61
6 Thermal Fragmentation of a Large Fullerene	62
6.1 Introduction	62
6.2 Parameterizing ReaxFF _{C-2013} Reactive Force Field.....	64
6.3 Simulation Methods and Details.....	71
6.4 Results and Discussion	72
6.5 Summary.....	79
7 Initial Validation of ReaxFF_{CHOB} Potential for Oxygen – Boron-Doped Graphene/Graphite Gas Surface Interactions	81
7.1 Introduction	81
7.2 Cluster models, DFT based binding energy curves and Performance of ReaxFF _{CHOB}	81
8 Conclusions	88
References.....	91

List of Figures

Figure 1: Sequence of reactions leading to the loss of a CO ₂ molecule from a naphthoxy radical upon exposure to an oxygen atom. The oxygen atom adsorbs at an edge carbon atom neighboring the semiquinone group in the naphthoxy radical.	8
Figure 2: Sequence of reactions leading to the loss of a CO ₂ molecule from a naphthoxy radical upon exposure to an oxygen atom. The oxygen atom adsorbs at a bridge position on the basal carbon atoms neighbouring the semiquinone group in the naphthoxy radical.	9
Figure 3: Oxygen functionalized pristine and defective graphene models	10
Figure 4: Structure of graphene and graphite surfaces used in NVE simulations. Carbon atoms in the top layer of graphite are colored blue while those in the bottom layer are colored gray	12
Figure 5: Structure of Graphite surfaces used in successive energetic oxygen atom collision simulations. (a) Graphite basal plane, (b) Armchair (AC) edges, (c) Zigzag (ZZ) edges. Carbon atoms are colored green while hydrogen atoms are colored white.	14
Figure 6: Sequence of events leading to the breakup of a graphene sheet upon energetic oxygen atom collision. Carbon atoms are colored gray while oxygen atoms are colored red.....	16
Figure 7: Sequence of events leading to the breakup of graphite. Carbon atoms on the top layer are colored gray, carbon atoms in the bottom layer are colored blue and oxygen atoms are colored red.	17
Figure 8: Variation of the system temperature with time upon successive energetic oxygen atom impacts.	18
Figure 9: Number of carbon atoms lost from graphite basal plane upon hyperthermal atomic oxygen etching, expressed as a ratio of the number of carbon atoms lost to the initial number of carbon atoms...	19
Figure 10: Number of carbon atoms lost from armchair (AC) edges upon hyperthermal atomic oxygen etching, expressed as a ratio of the number of carbon atoms lost to the initial number of carbon atoms...	19
Figure 11: Number of carbon atoms lost from zigzag (ZZ) edges upon hyperthermal atomic oxygen etching, expressed as a ratio of the number of carbon atoms lost to the initial number of carbon atoms...	20

Figure 12: Arrhenius fits to graphite mass loss rate upon energetic oxygen atom collision.....	22
Figure 13: Erosion yield of graphite surfaces upon hyperthermal atomic oxygen etching.....	23
Figure 14: Mode of mass loss from graphite surfaces upon energetic atomic oxygen etching	24
Figure 15: A few 'large' molecules lost from graphite basal planes at 1100K surface temperature. Carbon atoms are colored brown while oxygen atoms are colored red.....	25
Figure 16: Mechanism of loss of a CO ₂ molecule from graphite basal plane.....	26
Figure 17: Structure of the diamond surfaces used in individual energetic oxygen atom collisions simulations. Carbon atoms are colored gray, oxygen atoms are colored red and hydrogen atoms are colored white. (a) Diamond (100) surface, (b) Diamond (111) surface and (c) Diamond (110).....	31
Figure 18: Structure of the diamond surfaces used in successive energetic oxygen atom collisions simulations. Carbon atoms are colored gray and hydrogen atoms are colored white. (a) Diamond (100) surface, (b) Diamond (111) surface and (c) Diamond (110) surface.	32
Figure 19: Some structures resulting from ReaxFF simulations of individual hyperthermal oxygen atom collisions with model diamond surfaces	36
Figure 20: A sequence of states through which a diamond (100) surface proceeds upon hyperthermal atomic oxygen collision at 1000K.	39
Figure 21: A sequence of states through which a diamond (111) surface proceeds upon hyperthermal atomic oxygen collision at 1000K.	40
Figure 22: A sequence of states through which a diamond (110) surface proceeds upon hyperthermal atomic oxygen collision at 1000K.	40
Figure 23: Number of carbon atoms lost from diamond (100) upon hyperthermal atomic oxygen etching, expressed as a ratio of the number of carbon atoms lost to the initial number of carbon atoms	42
Figure 24: Number of carbon atoms lost from diamond (111) upon hyperthermal atomic oxygen etching, expressed as a ratio of the number of carbon atoms lost to the initial number of carbon atoms	43
Figure 25: Number of carbon atoms lost from diamond (110) upon hyperthermal atomic oxygen etching, expressed as a ratio of the number of carbon atoms lost to the initial number of carbon atoms	44

Figure 26: Etching of a layer of diamond (111) surface by hyperthermal atomic oxygen. Oxygen atoms are colored red while carbon atoms in the 1st surface layer are colored yellow, carbon atoms in the 2nd layer are colored blue, carbon atoms in the 3rd layer are colored white and carbon atoms in the subsequent layers underneath are colored green..... 45

Figure 27: Arrhenius fit to the rate of carbon atom loss from diamond surfaces subject to hyperthermal atomic oxygen etching. In all the plots, the blue circles correspond to data from our simulations while the red line corresponds to the Arrhenius fit to the data..... 47

Figure 28: Erosion yield of diamond surfaces upon hyperthermal atomic oxygen etching plotted along with the erosion yield of graphite basal plane. The points correspond to the data from the simulations while the solid lines correspond to the Arrhenius fit to the erosion yield..... 48

Figure 29: (a) Cleaved (001) α -quartz surface. (b) Reconstructed (001) α -quartz surface. Oxygen atoms are red, and silicon atoms are gray..... 53

Figure 30: Non-defective clusters. (a) T2-B1, (b) T2-B1+O, (c) T5-S1+O, (d) T8-B1 53

Figure 31: Defective Clusters: (a) T4-O, (b) T4-O+O, (c) T4-O₂||, (d) T4-O₂⊥, (e) T4-O₂||+O, (f) T4-O+O₂||..... 54

Figure 32: Binding energy curves for T2B1-O..... 57

Figure 33: Binding energy curves for T5S1-O 58

Figure 34: Binding energy curves for T8B1 58

Figure 35: Binding energy curves for T4-O 58

Figure 36: Binding energy curves for T4-O+O 59

Figure 37: Binding energy curves for T4-O₂||..... 59

Figure 38: Binding energy curves for T4-O₂⊥..... 59

Figure 39: Binding energy curves for T4-O₂||+O..... 60

Figure 40: Binding energy curves for T4-O+O₂||..... 60

Figure 41: Equation of state data for the isotropic variation of the lattice constant along graphite basal plane directions.	66
Figure 42: Equation of state data for the variation of the lattice constant normal to the graphite basal plane directions.	66
Figure 43: Equation of state data for the cubic expansion of a 2x2x2 diamond super cell containing 16 atoms.	67
Figure 44: Equation of state data for the uniaxial expansion of a 2x2x2 diamond super cell containing 16 atoms in the (001) direction.	68
Figure 45: Relative energies (in kcal/mol) of vacancy and stone - wales defect in graphene with respect to pristine graphene expressed on a per atom basis.	69
Figure 46: Relative energies (in kcal/mol) on a 'per atom' basis of amorphous phases with respect to fullerenes of corresponding sizes.	70
Figure 47: (a)-(e) Decay of a C ₁₈₀ fullerene as a function of time from the 10 independent trajectories at each target temperature. (f) Curve fit to the exponential and linear regime of the decay process at 4300K.	74
Figure 48: A sequence of states through which a C ₁₈₀ molecule proceeds upon thermal fragmentation at 4100K.	75
Figure 49: The average probability for the shrinking of the C ₁₈₀ fullerene through the loss of a C _n molecule at temperatures between 4100K and 4500K.	78
Figure 50: Models considered for oxygen - boron doped graphene gas surface interactions. Carbon atoms are colored gray, boron atoms are colored orange and hydrogen atoms are colored white.	82
Figure 51: Oxygen binding to various positions on boron doped coronene molecule.	82
Figure 52: Binding energy curve for model A.	84
Figure 53: Binding energy curve for model B.	84
Figure 54: Binding energy curves for model C.	85
Figure 55: Binding energy curves for model D.	85

Figure 56: Binding energy curves for model E..... 86
Figure 57: Binding energy curves for model F..... 86

List of Tables

Table 1: Comparison of ReaxFF and DFT based simulations on the graphene model	10
Table 2: Rate of carbon atom loss from graphite surfaces upon energetic oxygen atom etching.....	21
Table 3: Percentage of trajectories leading to various reactions on model diamond (100) surface using various methods	34
Table 4: Percentage of trajectories leading to various reactions on model diamond (111) surface using various methods	35
Table 5: Percentage of ReaxFF trajectories leading to various reactions on diamond (110) surface.....	35
Table 6: Rate of carbon atom loss from diamond surfaces and their Arrhenius parameters	46
Table 7: Formation energy of various fullerenes expressed on a 'per atom' basis with respect to C ₆₀ molecule	70
Table 8: Rate of mass loss from the C ₁₈₀ fullerene at various temperatures in both the exponential and linear regimes of decay.....	77
Table 9: Binding energy of oxygen atom in models A - F.....	83

Acknowledgement

Firstly, I would like to express my sincere thanks and deep felt gratitude to my advisor Dr. van Duin for all his time, support, encouragement and guiding me through the course of this work. His immense knowledge in the field of computational chemistry was instrumental in the completion of this work. He has been a constant source of motivation during the course of my PhD studies. Thank you, professor.

Secondly, I would like thank the sponsoring agency, Air Force Office of Scientific Research (AFOSR), for the financial support without which it would have been impossible to perform this work.

I would like to thank my family for their constant support and encouragement all through my life. All that I have achieved in my life is mainly because of this support and motivation. Thank you. I shall remain greatly indebted to you forever.

I would like to thank my office mates for a number of insightful discussions we had during the course of this work. It was a great experience to work with you all.

Finally, I would like to thank the Penn State University for giving me the opportunity to pursue graduate studies.

1

Introduction

Space crafts and satellites orbiting in the Low Earth Orbit (LEO) are exposed to an environment consisting of atomic and molecular oxygen, helium, nitrogen, hydrogen, argon and other ionized species such as O^{+1} . Dominant amongst these species is atomic oxygen ($O(^3P)$) with a number density of $\sim 10^9$ cm^{-3} . A space craft traveling in LEO at an orbital velocity of ~ 8 km/s is subjected to collisions with these highly corrosive species in addition to exposure to vacuum ultraviolet radiation (VUV) and X-rays. A combination of the orbital velocity of the space craft and the number density of atomic oxygen yields a flux of 10^{15} O atoms $cm^{-2}s^{-1}$ at mean collision energy of 5eV. These energetic collisions induce chemical and physical changes in the material through erosion and oxidation. Further, atmospheric reentry vehicles and capsules enter earth's atmosphere at hypersonic speeds ranging from 21 km/s for reentry from Mars² to about 7 km/s for space shuttle reentry³. In addition, the next generation high speed aerospace vehicles are envisaged to fly at hypersonic speeds larger than Mach 6 (e.g. NASA – X43⁴ or Boeing waverider⁵ research vehicles). At such high speeds, a strong bow shock forms in front of the vehicle with the temperature of the gas in the layer between the shock and the surface of the vehicle reaching several thousands of degrees kelvin. High speed vehicles are equipped with Thermal Protection System (TPS) to protect the vehicle and the crew from the tremendous heat load. Extreme temperatures in the gas layer cause vibrational excitation and dissociation of diatomic gas molecules (mainly O_2 and N_2). These molecules reach the surface of the vehicle in a dissociated nonequilibrium state. The surface of the vehicle often acts a catalyst for the exothermic recombination of these radicals, increasing the heat load on the vehicle⁶. Carbon based materials are often used as TPS (e.g. space shuttle TPS) materials⁷ and on the surfaces of vehicles/objects in LEO owing to their low weight and desirable mechanical properties. These materials react with energetic radical species (O and N) to form a range of products (CO , CO_2 , CN etc.) resulting in their erosion. To characterize the damage due to the high energy collisions with radicals

and ablation, and predict, improve and develop suitable oxidation resistant materials, a fundamental understanding of the processes involved in these gas surface interactions is essential.

Ground based experiments are unable to elucidate the fundamental chemical events associated with these gas (high energy) – surface (high temperature) interactions owing to the difficulty in replicating the conditions witnessed in actual hypersonic flight or in the LEO environment. Thus, one has to resort to theoretical modeling, through molecular dynamics simulations, to obtain atomistically detailed insight into these collision events. Density Functional Theory (DFT) based modeling is capable of providing such detailed information on the chemical events. However, the associated computational cost limits the size of the systems that can be studied using DFT. As an alternative to DFT, classical potentials allow for simulations for very large systems (millions of atoms), however, they are usually incapable of describing chemical reactions due to rigid atomic connectivity requirements (e.g. AMBER⁸, MM3⁹⁻¹¹ etc.). ReaxFF¹² is an empirical potential that allows for the simulation of chemical reactions on large systems while retaining most of the accuracy of DFT. Similar to the bond-order based force fields pioneered by Abel¹³, Tersoff¹⁴ and Brenner¹⁵, and to more contemporary reactive potentials like AIREBO¹⁶ and COMB¹⁷⁻¹⁹, ReaxFF employs a bond distance/bond order relation to enable formation and dissociation of chemical bonds during a simulation. However, in contrast to other bond order based potentials, ReaxFF is highly transferrable in nature with a particular emphasis on capturing transition states in reactions, in addition to the reaction energies themselves. A detailed description of the ReaxFF potential is provided in the next chapter. In this work, ReaxFF potential has been used to study the oxidation of graphene, graphite and diamond subject to high energy oxygen atom bombardment. Further, ReaxFF potentials have been developed using high quality DFT data to describe oxygen – silica gas surface interactions (ReaxFF_{SiO}^{GSI}) and carbon condensed phases (ReaxFF_{C-2013}) accurately. The newly developed ReaxFF_{C-2013} potential has been used to study the thermal decomposition of a large fullerene molecule. ReaxFF_{C-2013} and ReaxFF_{SiO}^{GSI} can now be used in the full computational chemical modeling of the pyrolysis of carbon rich materials and energetic oxygen collision events on silica surfaces

respectively. Finally a set of DFT based potential energy curves have been computed for the interaction of atomic oxygen with boron doped graphite. Details of the ReaxFF reactive force field are described in chapter 2 followed by the molecular dynamics simulations of graphene and graphite oxidation upon energetic oxygen atom impact in chapter 3, and diamond oxidation in chapter 4. Chapter 5 describes the development of a ReaxFF potential ($\text{ReaxFF}_{\text{SiO}}^{\text{GSI}}$) to describe oxygen – silica gas surface interactions while chapter 6 discusses the development of $\text{ReaxFF}_{\text{C-2013}}$ and its application to fullerene decomposition simulations. Chapter 7 describes the DFT data obtained for the development of a potential for oxygen – boron doped graphene gas surface interactions and finally, conclusions from this work are presented in chapter 8.

ReaxFF¹² is a general bond-order-dependent potential that uses a relationship between bond distance and bond order on one hand and a relationship between the bond order and bond energy on the other to describe bond formation and bond dissociation realistically. This formulation allows ReaxFF to describe under- and over-coordinated systems properly. The bond orders are combined with functions of valence coordinates such as bond angles and torsion angles so that the energy contributions from bonding terms vanish upon bond dissociation. The ReaxFF potential uses central field formalism wherein nonbonded interactions, namely Coulomb and van der Waals interactions, are calculated between every atom pair. Excessively close range interactions are avoided by using a shielding term²⁰ in the energy expression for the nonbonded interactions. Atomic charges are calculated using the geometry-dependent charge calculation scheme (EEM scheme) of Mortier et al²¹. Instead of Ewald summation to calculate long-range Coulomb interactions, ReaxFF uses a seventh-order taper function²² with an outer cutoff radius of 10 Å. The system energy in ReaxFF is calculated as the sum of a number of energy terms as:

$$E_{sys} = E_{bond} + E_{over} + E_{under} + E_{lp} + E_{val} + E_{pen} + E_{tors} + E_{conj} + E_{vdWaals} + E_{Coulomb}$$

A detailed description of each of these terms and their energy expressions can be found in the original work¹². ReaxFF parameters are optimized against Quantum Chemical (QC) data based on Density Functional Theory (DFT) on relevant systems. Typically, this data consists of atomic charges, geometric parameters such as bond lengths, bond angles, torsions and lattice constants, heats of formations, equation of state data and reaction energies. Once the ReaxFF parameters are developed, they can be employed in molecular dynamics simulations to study the chemistry and dynamics under varied conditions in systems of our interest. An important aspect of ReaxFF potential is that it can be systematically improved by fitting to new DFT data in an iterative manner as research on a specific problem proceeds.

3

Graphene / Graphite Oxidation

3.1 Introduction

(Parts of this chapter were published in Goverapet Srinivasan and van Duin²³)

Owing to their light weight and desirable chemical and mechanical properties, carbon based materials like organic thin films, polymers and carbon fiber reinforced composites are commonly used as ablatives and heat shield in spacecraft applications. In the Low Earth Orbit (LEO) altitudes, ranging from ~200 km to ~700 km, the rarefied atmosphere consists of various chemical species that include atomic and molecular oxygen, helium, nitrogen, atomic hydrogen, argon etc. Dominant amongst these species is atomic oxygen with an O atom number density of $\sim 10^9 \text{ cm}^{-3}$ ¹. A spacecraft traveling at an orbital velocity of ~8 km/s in LEO is subject to collisions with atomic oxygen in addition to exposure to vacuum ultraviolet light, X rays, charged species such as O^+ and other chemical species¹. These highly energetic collisions result in chemical and physical changes in the material due to erosion and oxidation. A combination of O atom density and orbital velocity of the spacecraft yields a flux of approximately $10^{15} \text{ O atoms cm}^{-2} \text{ s}^{-1}$ at a mean collision energy of $\sim 5 \text{ eV}$ ¹. In order to characterize the damages due to these high energy collisions, predict the long term behavior of these materials and improve them, a fundamental understanding of the chemical reactions and dynamics involved in these processes is essential.

Experimental works done in the past have frequently used Highly Ordered Pyrolytic Graphite (HOPG) as the model surface to study these highly energetic reactions. Kinoshita et al²⁴ characterized the surface of HOPG after it was exposed to atomic O with a translational energy of 5eV at room temperature using X-ray photo-electron spectroscopy (XPS) and Scanning Tunneling Microscopy (STM). They found from the XPS spectra that the oxygen coverage reached a saturation value of 0.94 with oxygen fluence of approximately $4 \times 10^{17} \text{ atoms cm}^{-2}$. Analysis of the C 1s peak by XPS revealed the presence of C-O, C=O, O-C=O. Ngo et al²⁵ found that a carbon atom was etched for every 8 impinging oxygen atoms from their measurements on an HOPG sample placed aboard the space shuttle Atlantis (mission STS46). Nicholson

et al²⁶⁻²⁸ conducted a series of experiments to study the morphological evolution of HOPG upon exposure to hyperthermal O atoms. They found that the erosion rate was strongly dependent on the surface temperature of HOPG. Atomic force microscopy images revealed embedded cylindrical erosion pits whose diameters spanned nanometer through micrometer length scales while their depths ranged from a few to tens of nanometers. The pits were found to have convex curvature at the pit bottom. These effects were attributed to the anisotropic kinetics involved in the lateral vs downward reactivity of HOPG. These experiments, however, did not elucidate the reaction mechanisms. Theoretical work aiming to describe the oxidation of graphite has been done by a few researchers in the past. Cohen²⁹ attempted to estimate the loss function of graphite subject to oxygen collisions using classical trajectory. It was suggested that the erosion of graphite is a two-step process, the first step involving epoxide functionalization of the surface followed by the removal of this group as CO due to the impact of another O atom. It has been observed in combustion and gasification chemistry that the rate determining step in the gasification of graphite involves a reaction that produces CO initially. The production of CO/CO₂ is believed to occur due to the migration of an epoxide oxygen to defect sites that are functionalized by semiquinones and/or contain chemisorbed O₂ molecules³⁰. The epoxide groups neighboring semiquinones are known to weaken carbon – carbon bonds and facilitate this reaction³¹⁻³³. The direct loss of a CO₂ molecule from graphene basal surface was shown to proceed via a lactone intermediate. The presence of a neighboring epoxide or ether group was shown to facilitate this reaction by weakening the C-C bond between the lactone and graphene basal plane³⁴. Using ReaxFF based molecular dynamics (MD) simulations on defect free graphene oxide (GO), Bagri et al³⁵ observed that CO and CO₂ evolution occurred due to the desorption of epoxy groups in close proximity to other saturated *sp*³ carbon bonds. This led to the creation of vacancies within the basal plane. Defects formed on high temperature reduction of GO were always found to be decorated with carbonyl groups³⁶. While a lot of effort has been expended in understanding the reaction mechanisms leading to the oxidation and CO / CO₂ desorption from graphene / graphite and the associated energetics, these calculations do not provide information on the dynamics of CO / CO₂

evolution from graphene / graphite, particularly due to hyperthermal oxygen atom impact as witnessed in LEO environment and in hypersonic flight.

Experimental research^{24,26-28} works provide very valuable information about the atom / molecule scattering phenomena in such high energy collision processes and detailed information about the morphology of the eroded graphite specimen. However, these experiments are unable to provide information on the dynamic evolution (*in situ*) of the surface upon energetic oxygen atom impact. DFT based calculations are particularly useful in this regard. However, the size of the systems that can be simulated using these methods is small. Use of periodic boundary conditions with a small system may introduce artificially high levels of symmetry in the system. Force field based molecular dynamics simulations offer the flexibility to simulate both the small time scale reactive events and larger system sizes simultaneously, thereby providing the ability to capture the dynamic evolution of the surface. In the present work, hyperthermal collisions of atomic oxygen with a graphene sheet are studied through molecular dynamics simulations using the ReaxFF reactive force field.

3.2 Force Field Validation

In this work, the ReaxFF C/H/O parameter set developed by Chenoweth et al³⁷ has been used to study the oxidation of graphene and graphite subject to hyperthermal atomic oxygen atom impact. Since its development this parameter set has been used to study a diverse set of phenomena like the combustion of various fuels³⁸⁻³⁹, fullerene self – assembly from a benzene precursor⁴⁰, graphene oxide reduction³⁵, graphite oxidation⁴¹ etc. Specific to the problem of graphene oxide chemistry, this parameter set has been shown to reproduce experimentally observed chemical changes during the reduction of graphene oxide³⁵. To further validate the force field, a set of simulations were performed to compare the ReaxFF results against *ab-initio* data for prototypical systems. The loss of carbon atoms from a graphene (graphite) sheet as CO₂ or CO molecules is a particularly relevant chemical event with regard to this study. In tune with this objective, we consider the heterogeneous evolution of a CO₂ molecule from a naphthoxy radical upon

exposure to atomic oxygen. Figures 1 and 2 show the sequence of reactions leading to the loss of a CO₂ molecule. These two reaction mechanisms correspond to the adsorption of an oxygen atom to the two carbon atoms neighboring the semiquinone group of the naphthoxy radical. The reference system was taken to be a naphthoxy radical and an oxygen atom far away from it. The ReaxFF based relative energies (in eV) of all the intermediates and the final product, with respect to the chosen reference is shown underneath each image while the *ab-initio* based energies (in eV)⁴² are shown in parentheses next to the ReaxFF based energies. The *ab-initio* based energies were obtained at the QCISD(T)/6-31G(d)//B3LYP/6-31+G(d) level of theory⁴².

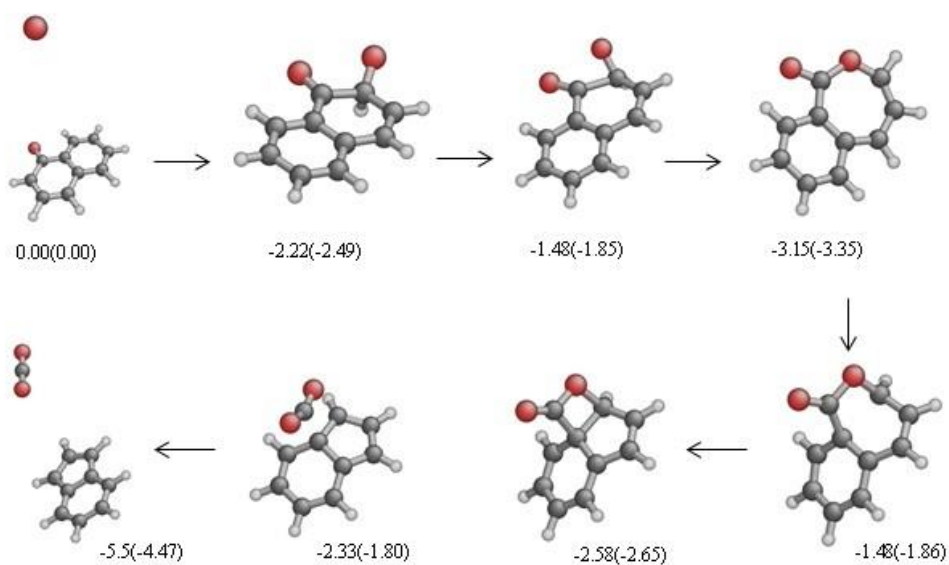


Figure 1: Sequence of reactions leading to the loss of a CO₂ molecule from a naphthoxy radical upon exposure to an oxygen atom. The oxygen atom adsorbs at an edge carbon atom neighboring the semiquinone group in the naphthoxy radical.

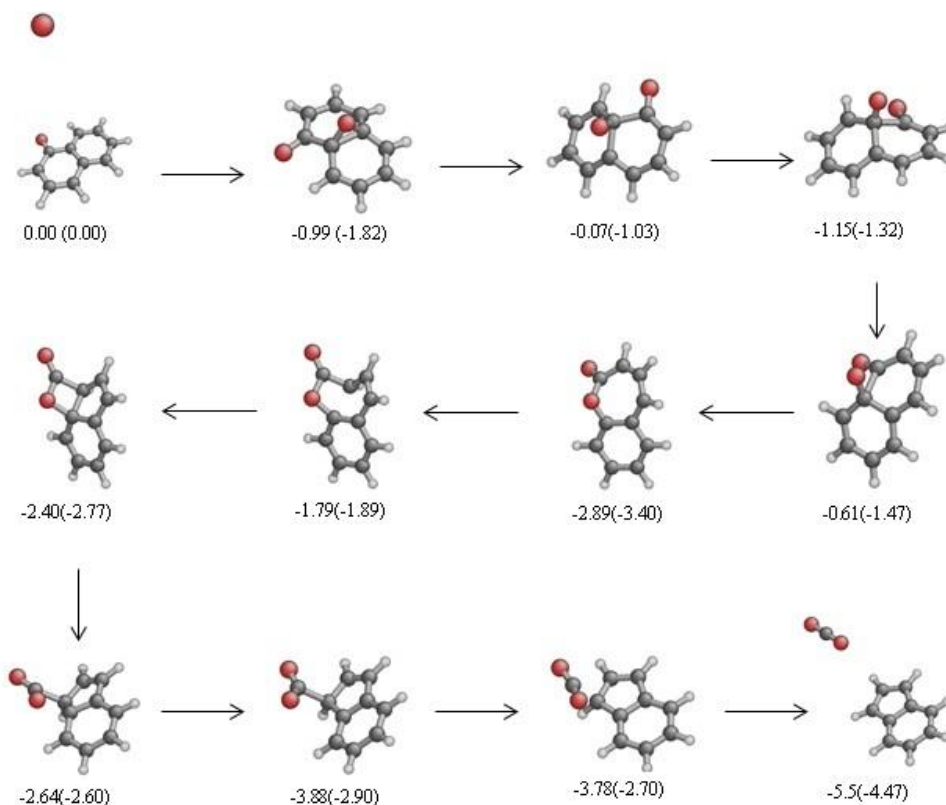


Figure 2: Sequence of reactions leading to the loss of a CO₂ molecule from a naphthoxy radical upon exposure to an oxygen atom. The oxygen atom adsorbs at a bridge position on the basal carbon atoms neighbouring the semiquinone group in the naphthoxy radical.

It is clear from the figure that the ReaxFF based energies (both reaction barriers and reaction energies) for all the stages in the chemical reaction leading to the loss of a CO₂ molecule from a naphthoxy radical are in good agreement with the DFT data. In a recent article, Paci et al⁴³ reported direct dynamics calculations of the hyperthermal impact of an oxygen atom with a model graphene surface based on DFT using the Perdew-Burke-Ernzerhof (PBE)⁴⁴ generalized gradient approximation (GGA) functional with a double- ζ polarization (DZP) basis set. Following Paci et al⁴³, two different sheets, a pristine and a defective graphene sheet with varying degrees of oxygen functionalization were considered. Figure 3 shows the various models considered.

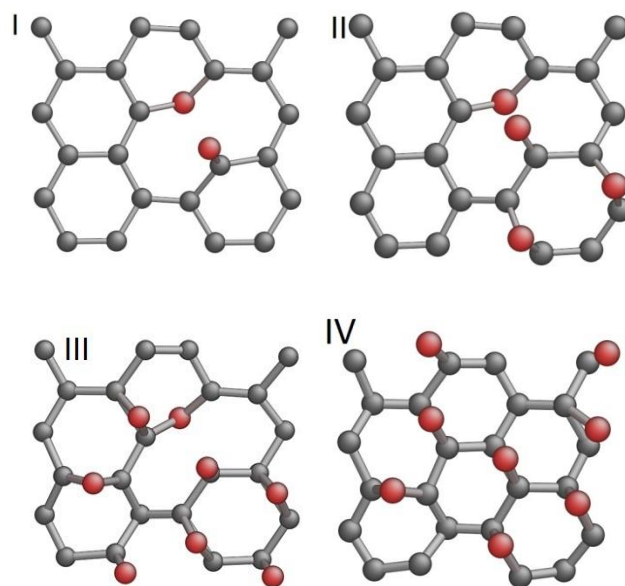


Figure 3: Oxygen functionalized pristine and defective graphene models

Each of these models was geometry optimized and equilibrated at 525 K before being subjected to 100 independent 5eV energetic oxygen atom impacts. The trajectory of the oxygen atom originated at around 5Å above the surface. Table 1 below shows the comparison between ReaxFF and DFT in terms of the number of different chemical events observed in the simulations. O¹ and O³ indicate trajectories run on singlet and triplet surfaces respectively.

Reaction	Model I		Model II			Model III			Model IV			
	DFT		DFT	ReaxFF		DFT	ReaxFF		DFT	ReaxFF		
	O ¹	O ³	O ¹	O ³		O ¹	O ³		O ¹	O ³		
Ring Opening	36	32	16	9	17	26	9	16	13	0	0	0
Epoxide Formation	76	75	94	77	70	88	33	29	57	7	17	19
Epoxide Migration	37	21	3	34	46	0	11	20	17	21	17	25
Carbonyl Formation	3	2	2	1	0	3	0	0	15	0	0	14
O ₂ Formation	1	0	2	17	17	2	55	53	20	79	76	72
CO ₂ Formation	0	0	0	1	3	2	2	1	6	0	0	6
CO Formation	0	-	0	1	-	0	6	-	1	0	-	0
Dioxirane Formation	0	0	0	2	0	0	1	1	0	0	0	0
Inelastic O	0	0	0	1	7	2	1	13	11	0	4	0
Sheet Damage	0	0	1	0	0	0	0	0	4	3	2	14

Table 1: Comparison of ReaxFF and DFT based simulations on the graphene model

From the above table, it is clear that ReaxFF is able to capture all the reactions observed in the DFT based trajectories. O₂ formation occurred almost always via an Eley-Rideal (ER) type direct reaction mechanism wherein the incoming oxygen atom plucked out an epoxide oxygen from the surface to form an O₂ molecule. This observation is consistent with the DFT based trajectories reported by Paci et al⁴³. Paci et al⁴³ concluded that the steady state surface coverage of oxygen atoms was between those in models II and III since the probability of O₂ formation was higher in model III than the probability of epoxide formation while ReaxFF based trajectories suggest that the probability of O₂ formation was higher in all the three models (model I – III) with a vacancy defect. From the above tests it can be seen that the present C/H/O force field parameters are well suited to study the oxidation and erosion of graphene / graphite upon hyperthermal oxygen atom impact. Details of the molecular dynamics simulations of oxygen bombardment are provided in the next section.

3.3 Molecular Dynamics Simulations

Molecular dynamics simulations using the ReaxFF reactive force field were carried out to investigate the outcome of successive hyperthermal oxygen atom collisions on graphene and graphite. Two sets of molecular dynamics simulations were carried out, one in micro-canonical (NVE) ensemble and the other in canonical (NVT) ensemble. Figure 4 below shows the structures used in the NVE simulations. The carbon atoms in the bottom layer of graphite are colored blue to distinguish them from the atoms on the top layer.

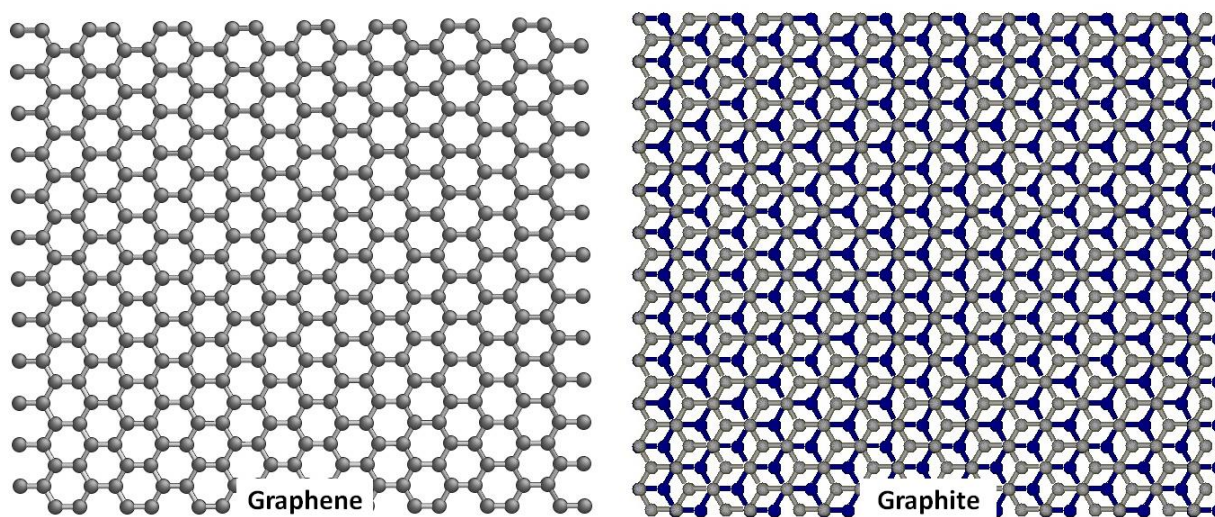


Figure 4: Structure of graphene and graphite surfaces used in NVE simulations. Carbon atoms in the top layer of graphite are colored blue while those in the bottom layer are colored gray. The graphene sheet had a total of 384 carbon atoms while the graphite stack had twice as many. The inter-layer separation between the graphene sheets in the graphite model was 3.2\AA . Before performing the oxygen collision simulations, the structures were geometry optimized, allowing for the lattice parameters in the in-plane (X and Y) directions to change, to obtain a strain free initial configuration. The resulting structures had a periodic cell dimension of $30.08\text{\AA} \times 34.76\text{\AA}$ (X and Y directions) in the basal plane of graphene. The direction normal to the graphene basal plane (Z direction) had a cell dimension of 240\AA . Reflective boundary conditions were imposed in the Z direction. These boundary conditions reverse the Z component of the velocity of any species that reaches the top (or bottom) face of the periodic cell (it acts like a virtual wall). Thus, any species leaving from the top side of the graphene sheet is confined to the space between the graphene sheet and the top face of the periodic cell. These conditions were used because it would be unrealistic if the species leaving from the top side of the graphene sheet were to enter from the bottom of the periodic cell and participate in the surface chemistry. In addition, the bulk side of the graphite specimen is inaccessible in experiments. An oxygen atom trajectory was initiated every picosecond. The oxygen atom was assigned a linear velocity corresponding to 5eV energy ($\sim 8\text{km/s}$). The

initial separation between the oxygen atom and the graphene sheet was around 7 Å. Only normal impact of the oxygen atom with the graphene sheet was considered in this study.

The impact of an energetic oxygen atom with the graphene sheet causes the C-C bonds in the vicinity of the impact to be vibrationally excited⁴⁵. This local vibrational excitation enables the breaking and creation of new bonds associated with impact of an energetic oxygen atom⁴⁵. Continuous bombardment of oxygen atoms imparts a significant amount of translational energy to the sheet. Consequently, the sheet is expected to get displaced downward from its initial position. This would increase the initial vertical separation between the graphene basal plane and the point of origin of the oxygen atom trajectory. To avoid this scenario, four dummy atoms were placed coplanar with the graphene sheet. A center of mass restraint between the atoms in the graphene sheet and the dummy atoms in the z coordinate direction was imposed with a weak coupling. A weak coupling allows for the buckling of the graphene sheet under the impact of the energetic oxygen atom while approximately holding the z coordinate of the center of mass of the graphene sheet at its original value. For the graphite stack, eight dummy atoms were used, 4 in each of the graphene layers. Two sets of mass center restraints were specified, one between the dummy atoms in the top layer and the carbon atoms in that layer while the other restraint was specified between the dummy atoms in the bottom layer and the carbon atoms in the bottom layer. The simulations employed a time step of 0.1fs.

The second set of simulations was aimed at quantifying the effect of surface temperature on the rate of mass loss from graphite upon successive energetic oxygen atom impacts. Further, these simulations were also used to investigate the effect of the orientation of graphite on the oxidative erosion rates. Towards this end, the simulations were carried out in a canonical ensemble (NVT ensemble) at surface temperatures varying between 500K and 2000K. At each surface temperature, three different graphite surfaces namely, graphite basal plane, armchair (AC) edge surface and zigzag (ZZ) edge surface, were exposed to energetic oxygen atom collisions normal to the surface. Figure 5 below shows the initial configuration of graphite surfaces used in these simulations.

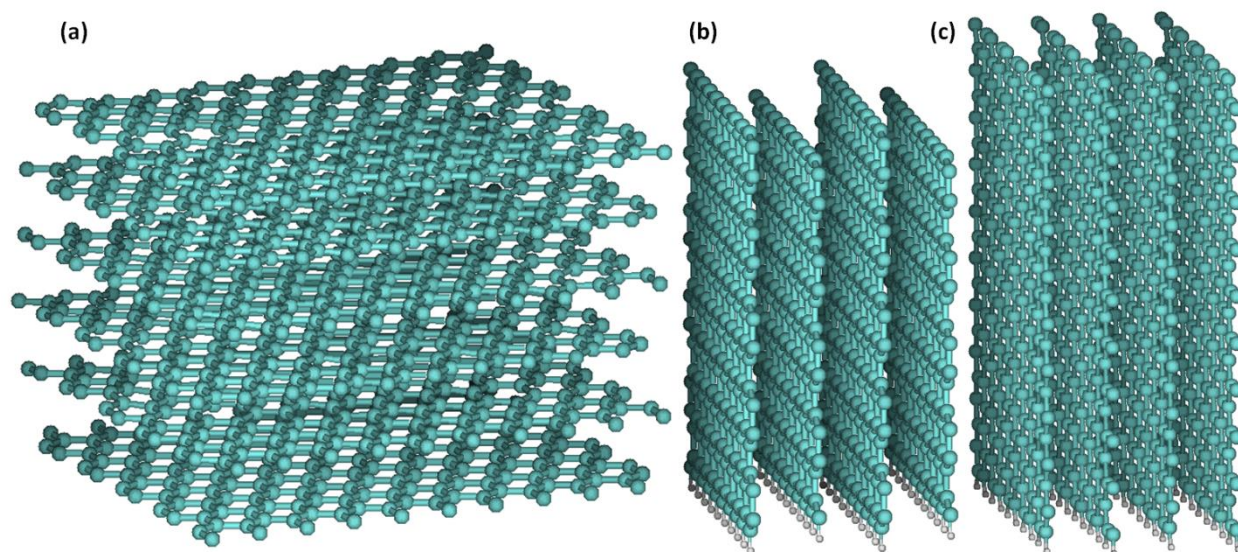


Figure 5: Structure of Graphite surfaces used in successive energetic oxygen atom collision simulations. (a) Graphite basal plane, (b) Armchair (AC) edges, (c) Zigzag (ZZ) edges. Carbon atoms are colored green while hydrogen atoms are colored white.

Graphite basal plane consisted of six graphene layers containing 200 carbon atoms each (a total of 1200 C atoms). AC edge surface consisted of 760 carbon atoms while ZZ edge surface consisted of 800 carbon atoms. The bottom side of both AC and ZZ edge surfaces were hydrogen terminated as shown in figure 5. Molecular dynamics simulations were carried out at 10 different surface temperatures; 500K to 1000K in intervals of 100K, 1100K, 1400K, 1700K and 2000K. Prior to molecular dynamics simulations, the systems were relaxed, allowing for the lattice vectors in the in-plane directions (X and Y directions for basal plane, Y and Z directions for AC edge, X and Z for ZZ edge) to change, resulting in a zero strain structure. The lattice parameter in the surface normal direction was held fixed at a value of 100\AA . All our molecular dynamics simulations were performed in NVT ensemble using a time step of 0.1fs. The temperature of the surface was controlled using a Berendsen thermostat⁴⁶ with a damping constant of 100fs. Post minimization, the surfaces were first equilibrated at 300K for a duration of 60 ps. However, the potential energy and temperature values indicated that the surfaces had well equilibrated by 15 ps. Thus, post equilibration, temperature ramping simulations were initiated from 300K to the target temperature (between 500K and 2000K) using atomic positions, velocities and accelerations from the

equilibration simulation, harvested at 5ps intervals beginning at 15ps till 60 ps, giving us a total of 10 independent trajectories for every target temperature (i.e., a total of 100 trajectories). All the trajectories were further equilibrated at the target temperature for a duration of 15 ps before oxygen atom collisions were initiated.

In all the 100 simulations, oxygen atom trajectories were initiated 5\AA above the surface while the in-plane coordinates of the oxygen atom were chosen randomly. The oxygen atoms were given a translational energy of 5eV directed normal to the surface. In all the simulations, one oxygen atom trajectory was initiated every 250fs, with the total simulation lasting for a maximum duration of 1.125ns (i.e. a maximum of 4500 5eV energetic oxygen atom collisions were simulated). Similar to the simulations in NVE ensemble, reflective boundary conditions were used in the surface normal directions and to avoid the downward displacement of the surface due to energetic oxygen atom impact, the bottom layer of the graphite basal plane and hydrogen atoms in the AC and ZZ edge surfaces were held fixed. Every 15ps (i.e., after 60 oxygen atom collisions), all the gas phase molecules were removed from the simulation cell. A discussion of the results from these simulations is presented in the next section.

3.4 Results and Discussions

Two sets of independent molecular dynamics simulations of energetic oxygen atom collisions with graphene and graphite stack were carried out using the ReaxFF reactive force field. The successive bombardment of oxygen atoms eventually led up to the breakup of the graphene sheet into gaseous species consisting of CO and CO₂ molecules primarily. The sequence of events leading to the breakup of the graphene sheet is shown below in figures 6.

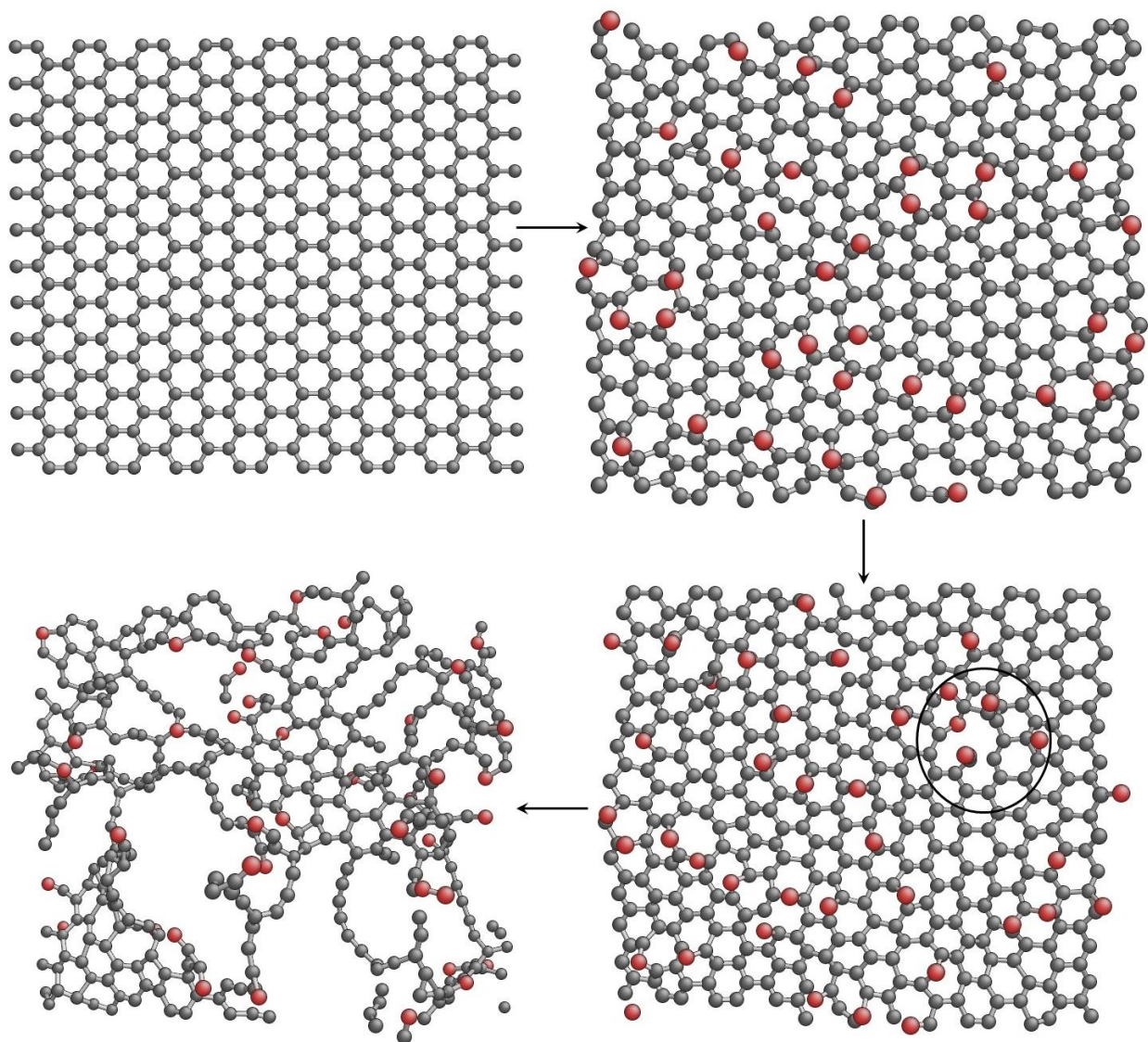


Figure 6: Sequence of events leading to the breakup of a graphene sheet upon energetic oxygen atom collision. Carbon atoms are colored gray while oxygen atoms are colored red.

The breakup of the graphene sheet can be divided into distinct regimes. The first regime corresponds to surface epoxide / ether formation wherein the incoming oxygen atoms bind to the graphene sheet in the form of epoxides and/or ethers. At some point in time, the first vacancy defect appears on the graphene sheet due to the loss of CO / CO₂ molecule. Once a vacancy defect is created, it expands rapidly resulting in the breakup of the sheet. Thus the final regime corresponds to one of defect growth through the loss of CO / CO₂ molecules. In the NVE simulations on graphene and graphite stack, C atom loss from the sheet

occurred primarily in the form of CO molecules and to a much lesser extent in the form of CO₂ and other molecules. The molecules leaving the surface were found to desorb from both the top and bottom sides of the graphene sheet. Figure 7 shows the sequence of events leading to the disintegration of the graphite stack.

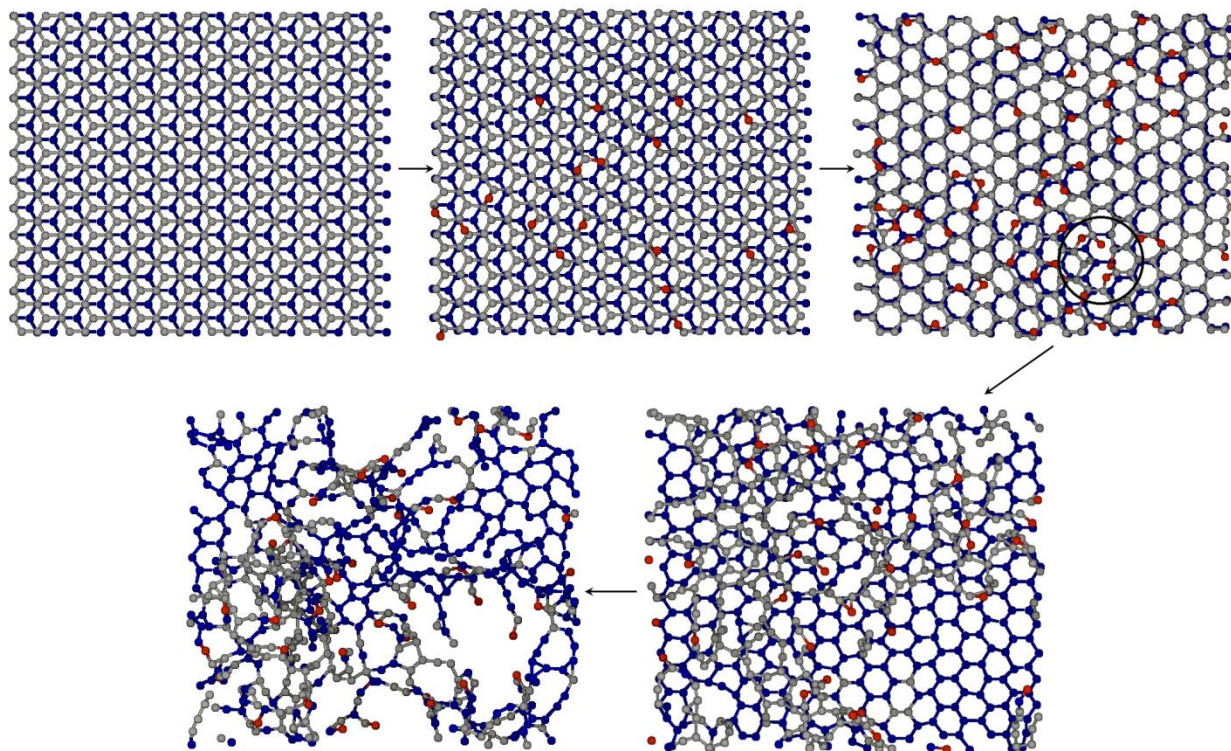


Figure 7: Sequence of events leading to the breakup of graphite. Carbon atoms on the top layer are colored gray, carbon atoms in the bottom layer are colored blue and oxygen atoms are colored red.

Like graphene, the breakup of a graphite stack can also be divided into distinct regimes. The first regime corresponds to the formation of epoxide / ether groups on the top layer of the graphite stack upon the impingement of an oxygen atom. At some point in time, the first vacancy defect is created on the top layer due to the loss of a CO / CO₂ molecule after which the defect grows laterally in the top layer. As the defect on the top layer grows larger, it exposes the carbon atoms in the second layer to energetic oxygen atom collisions. This leads to the formation of epoxides / ethers on the bottom layer which later goes through the same process of vacancy defect creation and its growth. As such, the erosion of a graphite

stack upon energetic oxygen atom impacts is a layer by layer sequential process. This observation is consistent with the experimental findings on the thermal oxidation of graphite⁴⁷. The growth of vacancy defects was observed to be anisotropic in nature with the defects growing more rapidly along the basal plane directions in comparison to the axial (depth wise) direction, an observation consistent with the molecular beam experiments on graphite²⁶⁻²⁸.

NVE simulations of oxygen bombardment gave useful information on the process of oxidative erosion of graphene / graphite. However, one does not have any control over the temperature of the system in NVE ensemble. Successive bombardment of 5eV energetic oxygen atoms leads to a buildup of energy in the simulation box which results in a dramatic increase in the system temperature. As shown in figure 8, within the course of the NVE simulation of the graphene sheet, the system temperature rose to around 4500K.

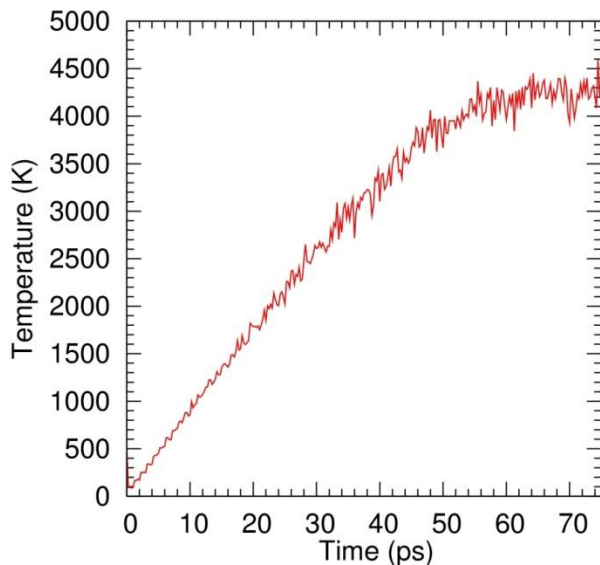


Figure 8: Variation of the system temperature with time upon successive energetic oxygen atom impacts.

The effect of surface temperature on the rate of mass loss from graphite was studied through the simulations performed in NVT ensemble. The simulations also investigated the effect of orientation of the graphite slab on the rate of mass loss upon energetic oxygen atom collisions. Figures 9 to 11 show the

number of carbon atoms lost from graphite basal plane, AC and ZZ edge surfaces respectively, expressed as a ratio of the number of atoms lost to the initial number of carbon atoms on the surface ($1-N/N_0$, $N_0 = 1200$ for basal plane, 760 for AC edges and 800 for ZZ edges). Results from all the 100 trajectories (10 surface temperatures, 10 independent trajectories at each surface temperature) for each surface orientation are plotted in these figures.

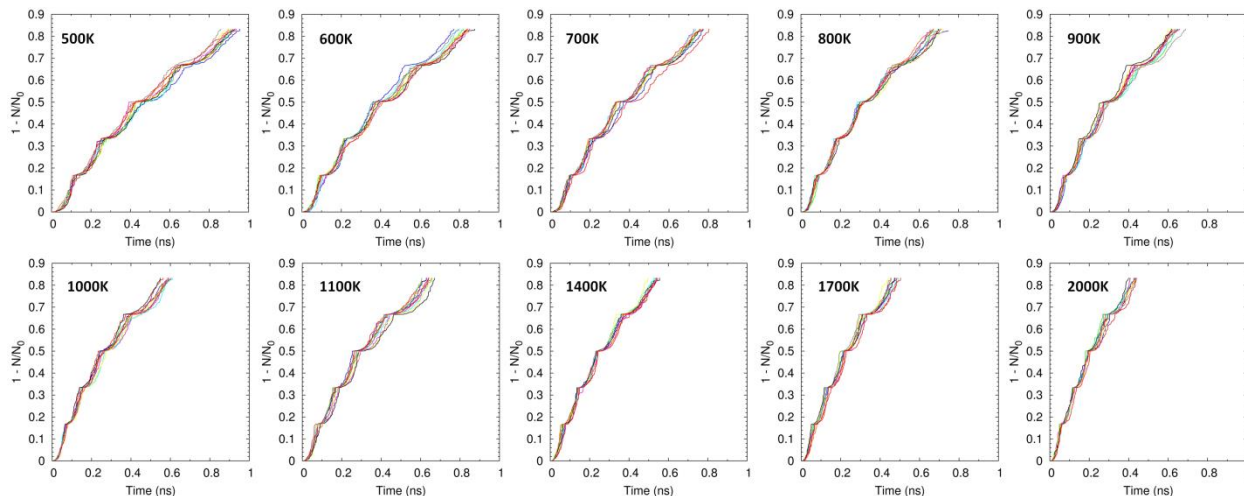


Figure 9: Number of carbon atoms lost from graphite basal plane upon hyperthermal atomic oxygen etching, expressed as a ratio of the number of carbon atoms lost to the initial number of carbon atoms.

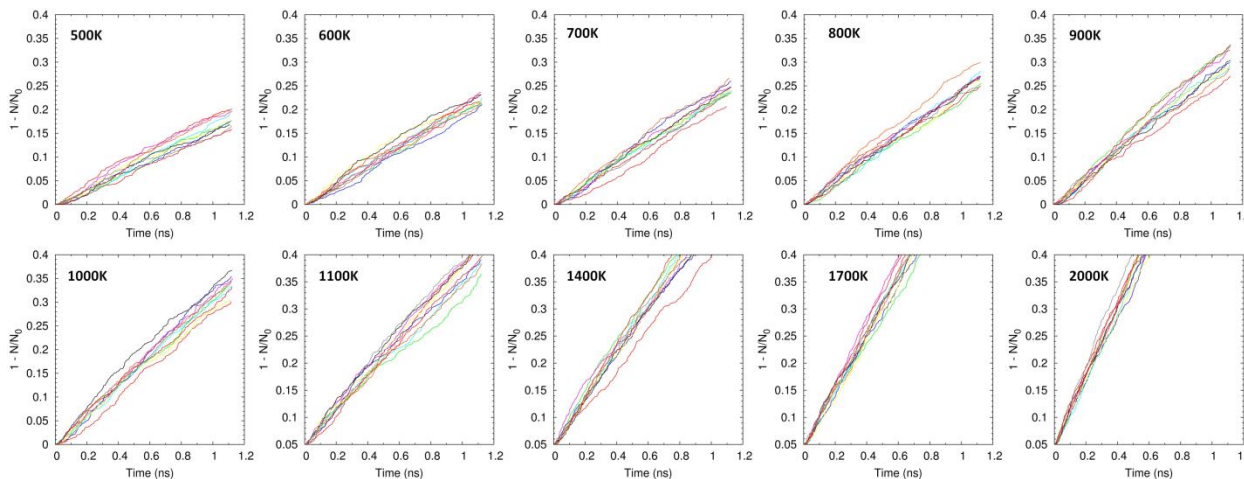


Figure 10: Number of carbon atoms lost from armchair (AC) edges upon hyperthermal atomic oxygen etching, expressed as a ratio of the number of carbon atoms lost to the initial number of carbon atoms.

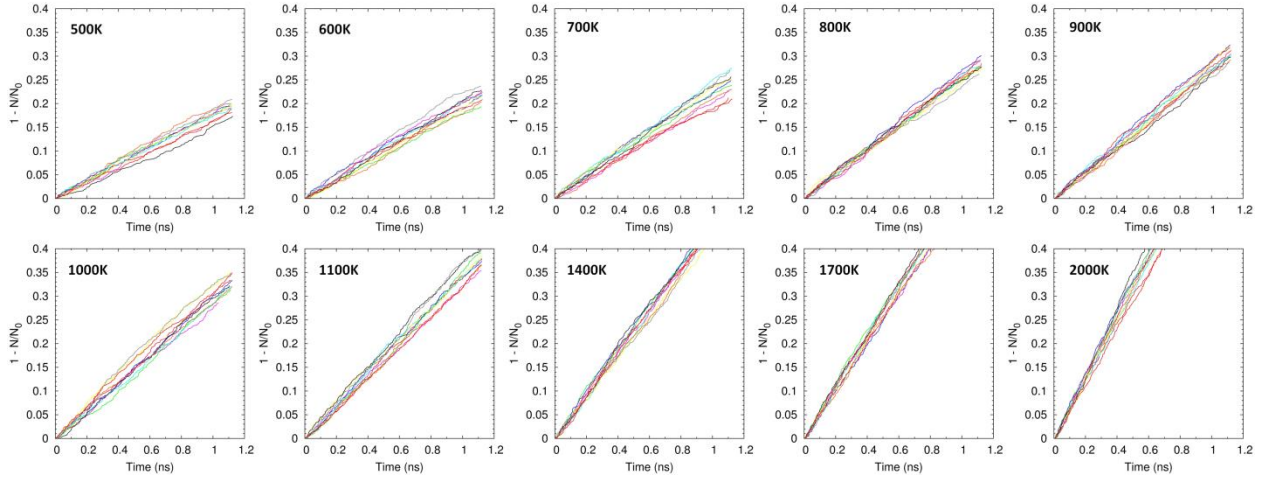


Figure 11: Number of carbon atoms lost from zigzag (ZZ) edges upon hyperthermal atomic oxygen etching, expressed as a ratio of the number of carbon atoms lost to the initial number of carbon atoms.

We see from figures 10 and 11 that the rate of loss of carbon atoms from both AC and ZZ edge surfaces are linear functions of time while a ‘wavy’ pattern (see fig 9) is observed for the basal plane due to the oxidative erosion of the basal planes being a ‘layer by layer’ phenomenon. The sequence of events leading to the loss of C atoms from the graphite basal planes is the same as those explained earlier. From the above figures, it is clear that an increase in the surface temperature causes an increase in the number of carbon atoms lost from the surface. This indicates that whilst the impact of oxygen atom occurs at hyperthermal energies, the loss of the carbon atoms from the surface is due to the thermal events taking place on the surface. In order to obtain the rate of loss of carbon atoms from graphite surface, a linear equation of the form $1 - N/N_0 = k \cdot t$ was fit to each of the curves in figures 9 to 11. The rate of carbon atom loss from each surface orientation at any simulated temperature was taken to be the average of rates of carbon atom loss obtained from the ten independent trajectories at that temperature. These rates were then used in an Arrhenius type expression to obtain the activation energy and the frequency factor for carbon atom loss from graphite surface. Table 2 below lists the rates obtained for each surface orientation while figure 12 shows the Arrhenius fit to the rates computed at each temperature for all the three surfaces.

Surface Temperature (K)	Rate of loss (ns⁻¹)		
	Basal Plane	Armchair edge	Zigzag edge
500	0.9692	0.1648	0.1747
600	1.0894	0.2023	0.1997
700	1.1826	0.2181	0.2208
800	1.3210	0.2414	0.2548
900	1.4309	0.2795	0.2742
1000	1.5634	0.3075	0.3000
Activation Energy (Kcal/mol)	0.936	1.184	1.074
Frequency factor (s⁻¹)	2.4 x 10⁹	5.4 x 10⁸	5 x 10⁸
1100	1.4054	0.3354	0.3415
1400	1.6846	0.4379	0.4441
1700	1.8931	0.5380	0.5165
2000	2.1030	0.6446	0.6246
Activation Energy (Kcal/mol)	1.932	3.132	2.84
Frequency factor (s⁻¹)	3.4 x 10⁹	1.4 x 10⁹	1.2x10⁹

Table 2: Rate of carbon atom loss from graphite surfaces upon energetic oxygen atom etching

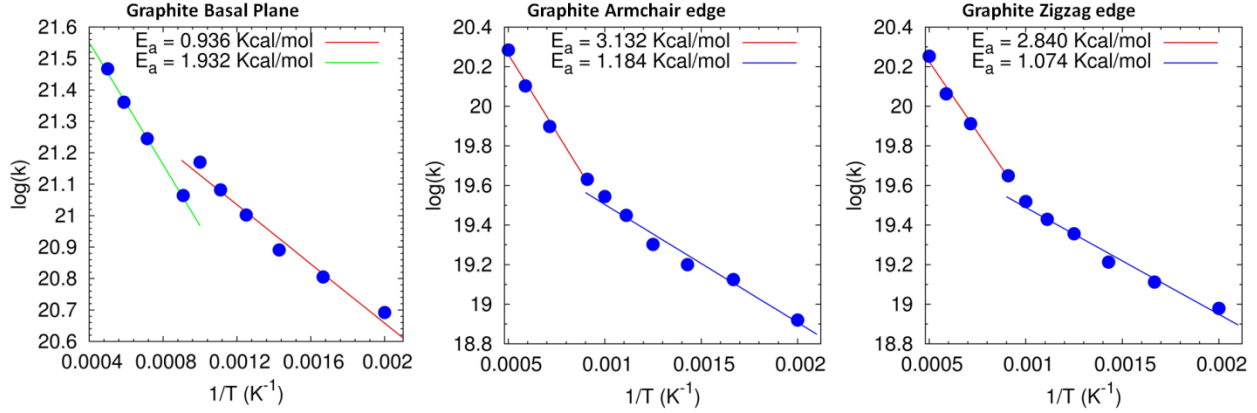


Figure 12: Arrhenius fits to graphite mass loss rate upon energetic oxygen atom collision

From table 2 it is clear that the graphite edges (both ZZ and AC edges) are much more resistant to energetic oxygen atom etching as compared to graphite basal planes. Nevertheless, all the three surface orientations show acceleration in the rate of mass loss beyond 1000K surface temperature giving two Arrhenius type regimes (see fig 12), a low temperature regime between 500K and 1000K, and a high temperature regime beyond 1000K. A commonly used measure to quantify the resistance of a material to energetic atom etching is the erosion yield (EY), defined as the volume of material lost per oxygen atom impact.

$$EY = \frac{\dot{m}}{\rho FS}$$

Here, \dot{m} is the rate of mass loss from the surface, ρ is the density of the material, F is the flux of oxygen atoms on the surface and S is the surface area of the exposed specimen. Figure 13 below shows the erosion yield of all the three surface orientations in both low temperature and high temperature regimes.

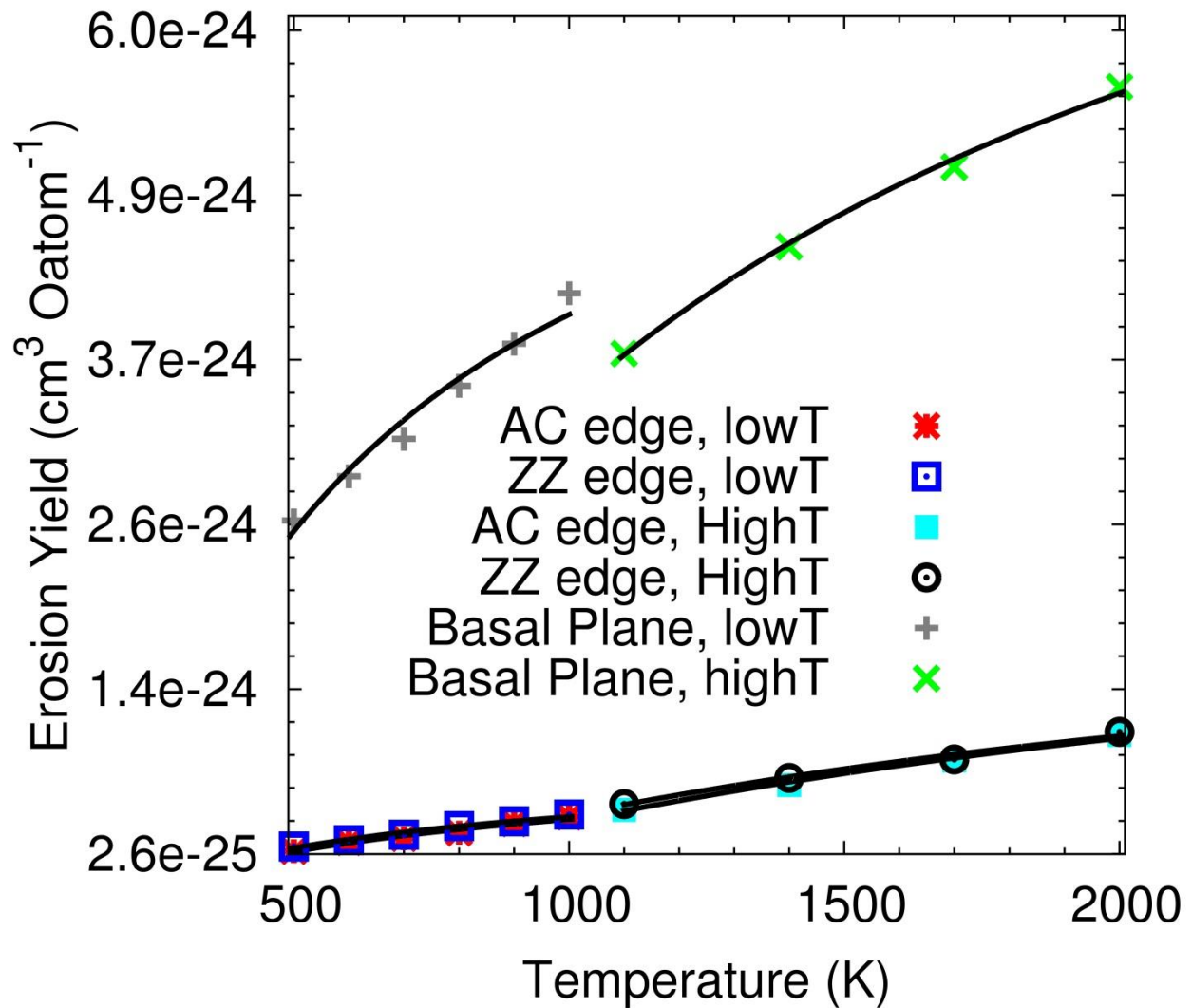


Figure 13: Erosion yield of graphite surfaces upon hyperthermal atomic oxygen etching

From the above figure, it is clear that the graphite edge surfaces are about an order of magnitude more resistant to energetic oxygen atom compared to basal planes. Further the erosion yield of graphite basal plane is in good agreement with experimental value of $1.1 \times 10^{-24} \text{ cm}^3 \text{ Oatom}^{-1}$ ^{26, 28} at 493K surface temperature. Comparing the erosion yield of graphite with Kapton H polyimide ($3 \times 10^{-24} \text{ cm}^3 \text{ Oatom}^{-1}$)⁴⁸, a commonly used spacecraft material, we see that graphite basal planes are just as poorly resistant to energetic oxygen atom etching as Kapton. As such, a different material that is more resistant to hyperthermal oxidation is desirable for such applications.

In addition to the rate of loss of carbon atoms from the surface of carbon based materials, the mode of mass loss is an essential consideration in the design of high speed aircrafts. It is now known that the injection of CO_2 molecules into the boundary layer around the vehicle helps in delaying the transition to turbulence as the energy in the acoustic disturbances is damped by its coupling to CO_2 normal modes. This energy transfer decreases the rate of amplification of the disturbances in the boundary layer and delays the transition to turbulence⁴⁹⁻⁵¹. Figure 14 shows the mode of mass loss from graphite surfaces upon energetic atomic oxygen etching.

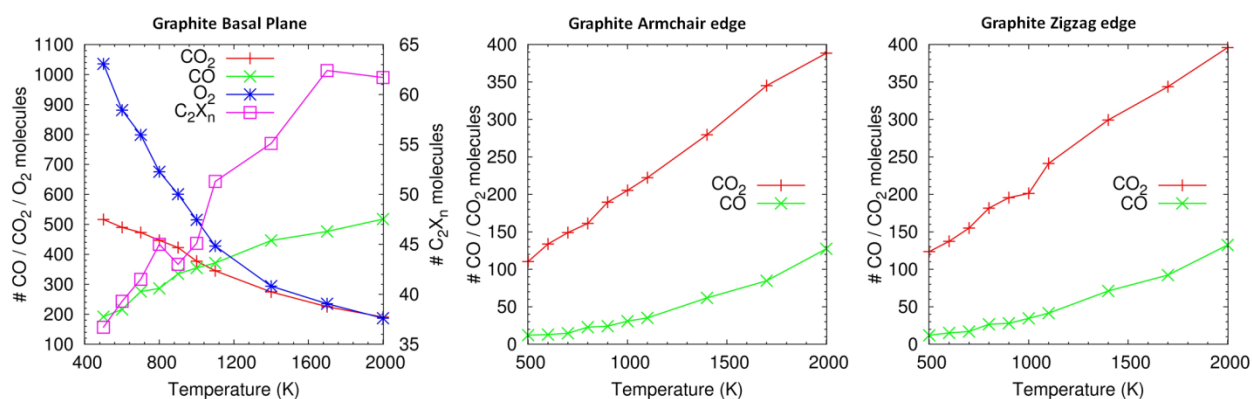


Figure 14: Mode of mass loss from graphite surfaces upon energetic atomic oxygen etching

At lower temperature, the loss of carbon atoms from graphite basal plane occurs predominantly through the loss of CO_2 molecules and to a lesser extent through the loss of CO molecules. With increase in temperature however, the mass loss through CO_2 molecules decreases monotonically. At high temperatures the mass loss occurs mostly via the loss of CO molecules. This is in direct contrast to graphite edge surfaces which lose mass predominantly via the loss of CO_2 molecules at all temperatures. Further, graphite basal planes also lose mass through the loss of C_2 , C_2O_n ($1 \leq n \leq 5$) and larger species with their contribution increasing with increase in temperature. Figure 15 shows the ReaxFF geometry optimized structures of a few of these ‘larger’ species observed in simulations at 1100K.

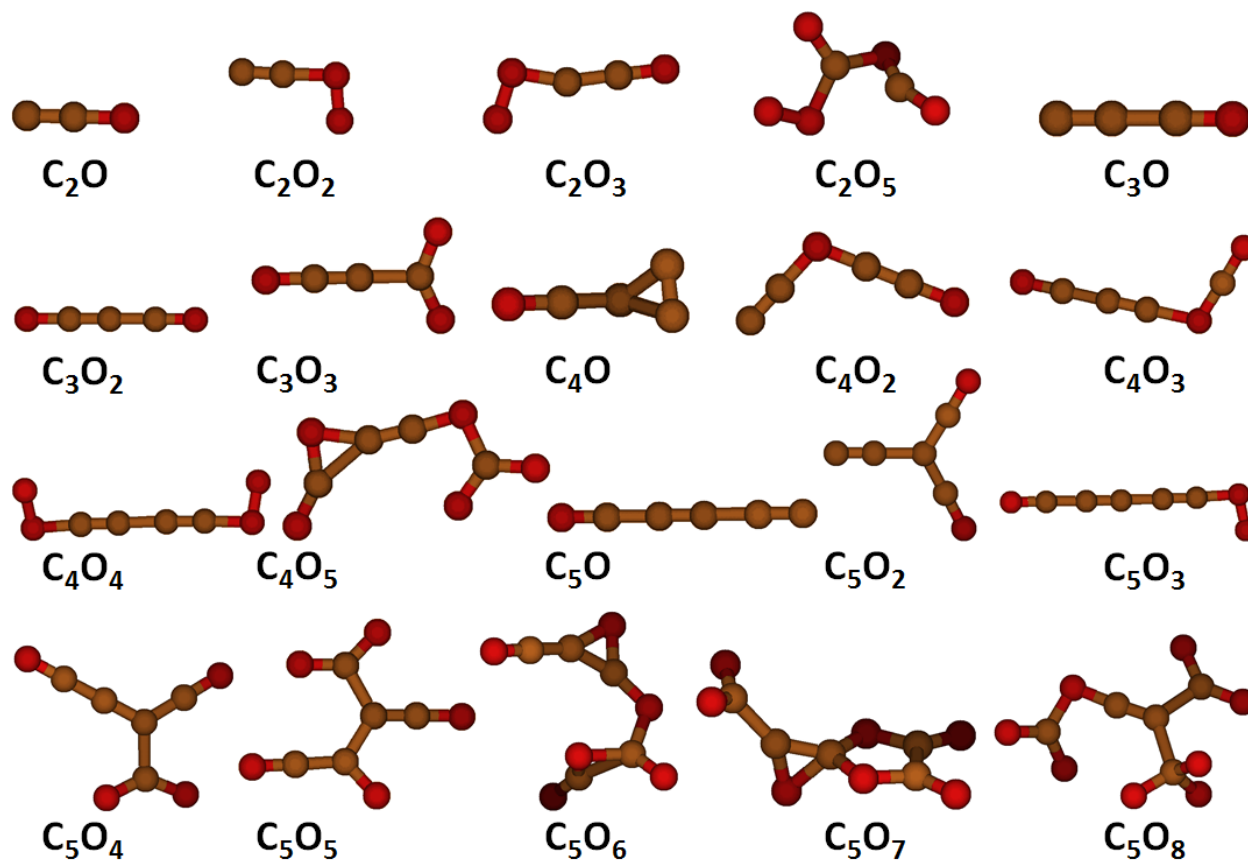


Figure 15: A few 'large' molecules lost from graphite basal planes at 1100K surface temperature. Carbon atoms are colored brown while oxygen atoms are colored red.

However, these products are expected to be kinetic in nature and short lived. For instance, the reaction $m\text{CO}_2 + n\text{O}_2 \rightarrow \text{C}_m\text{O}_{2(m+n)}$ is endothermic by more than 100 Kcal/mol for each of the molecules shown in figure 15. As a result, it is unlikely to be detected in time of flight mass spectrometry measurements of mass loss from graphite specimen in molecular beam experiments. In contrast to graphite basal planes, none of these larger species were observed during the oxidative erosion of both ZZ and AC edges.

Figure 16 below shows a mechanism of loss of CO_2 molecule from graphite basal planes observed in the simulations. Gray and red colored atoms in the figure represent carbon and oxygen atom respectively. Blue and orange colored atoms are oxygen and carbon atoms respectively that leave the surface as a CO_2 molecule. Green colored oxygen atom represents the incoming oxygen atom. 'Fault lines' were observed in the optical micrograph image of a partially oxidized graphite sample⁵². These

were explained to be due to the cooperative alignment of epoxides resulting in the unzipping of the graphene C-C network⁵². The black line in the 1st frame of the figure below shows that the simulations are able to reproduce this unzipping effect and creation of a fault line.

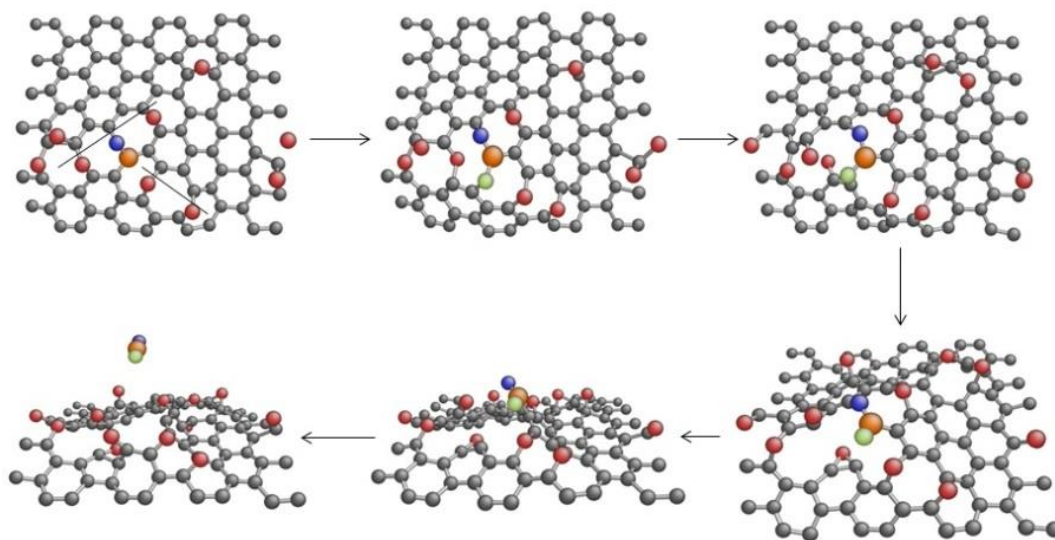


Figure 16: Mechanism of loss of a CO₂ molecule from graphite basal plane

Further, the formation of a lactone intermediate in frame 4 of the above figure is consistent with a DFT based study³⁴ which showed that CO₂ loss from graphene basal planes proceed via a lactone intermediate.

3.5 Summary

In summary, ReaxFF based molecular dynamics simulations have been used to study the direction dependent erosion of graphite subjected to 5eV energetic oxygen atom collisions. Prior to the simulations, ReaxFF potential was validated against DFT based energetics for relevant chemical reactions. The erosion of graphene and graphite basal plane can be divided into distinct regimes. The erosion of graphene occurs via epoxide formation followed by the creation of a vacancy defect and its growth leading to sheet breakup. Breakup of graphite occurs via epoxide formation on the top layer, creation of a vacancy defect and its growth in the top layer followed by epoxide formation on the bottom layer, creation and growth of vacancy defect on the bottom layer. As such the breakup of graphite basal planes was observed to be a

layer by layer phenomena with the vacancy defect growing much faster in the basal plane directions as compared to the axial (depth wise) direction. Molecular dynamics simulation of energetic oxygen atom etching at various surface temperatures indicated that with increase in temperature, the rate of mass loss increases from all the three surfaces namely, graphite basal planes, AC edges and ZZ edges. The mass loss from graphite basal planes occurs predominantly via the loss of CO₂ molecules at lower temperatures. However, with increase in temperature, the mass loss occurs increasingly via the loss of CO molecules and the number of CO₂ molecules lost from the surface decreases monotonically. In contrast, both ZZ and AC edges lose mass via the loss of CO₂ molecules at all temperatures. The erosion yield of AC and ZZ edges was an order of magnitude lower than graphite basal planes. The erosion yield of graphite basal planes obtained from the simulations is in good agreement with experimental values indicating that graphite basal planes are no better than Kapton H polyimide in resisting atomic oxygen etching. As such, a material with better oxidation resistance is more desirable as a spacecraft material in LEO conditions.

4

Direction dependent oxidative etching of diamond

4.1 Introduction

(Parts of this chapter have been submitted for review in Carbon⁵³)

From the results in the previous chapter, we see that graphite basal planes are poorly resistant to hyperthermal atomic oxygen etching with the rate of erosion increasing rapidly with increase in surface temperature. As such, a material with lower erosion rates is more desirable for space craft applications in LEO environment. Owing to their desirable physical and mechanical characteristics, and better oxidation resistance than graphitic materials⁵⁴, diamond thin films are promising materials for such applications. A number of studies in the past have been aimed at understanding the chemistry of oxidative etching of diamond. Oxidative etching of diamond has also been used as a way to polish and pattern diamond for optical applications⁵⁵⁻⁵⁶. Sandhu et al⁵⁷ observed that the reactive ion etching of diamond with oxygen ions occurred more rapidly as compared to etching in hydrogen ions, and that the rate of etching increased with increase in temperature. Oxidative etching of diamond (100) using dry oxygen revealed that the surface formed shallow square etch pits with the loss of carbon atoms proceeding via a step by step mechanism⁵⁸⁻⁵⁹. The steps edges were found to be more reactive than the terraces, indicating that the diamond (100) surface is strongly stabilized by oxygen atoms⁶⁰. Spectroscopic data indicated that the surface of oxidized diamond predominantly consisted of ether and carbonyl groups⁶⁰⁻⁶². Further, Loh et al⁶¹ observed the appearance of (2x1) reconstructions on diamond (100) surface upon the desorption of oxygen at 800 °C while Pehrsson et al⁶² observed an overlayer of graphitic sp² carbon on diamond (100) surface upon oxidation at substrate temperatures larger than 950 °C. Arrhenius type fits to the experimental etching rates indicated that the activation energy for the loss of carbon atoms from diamond (100) surface varied between 41 and 53 kcal/mol^{58, 60, 63-64}. Oxidative etching of diamond (111) surfaces resulted in the roughening of the surface, which eventually broke up into (100) facets after prolonged

etching^{59,65}. The etching rate of diamond (111) surface was found to be larger than that of diamond (100) surface with the activation energy for etching varying between 56 and 62 kcal/mol⁶⁴⁻⁶⁵.

Experimental studies of atomic oxygen etching under conditions similar to those found in LEO environment have been carried out by a few researchers in the past. Li et al⁶⁶⁻⁶⁷ studied the oxidative etching of hot filament chemical vapour deposited (CVD) diamond films subjected to 5eV energetic oxygen atom collisions at a flux of 2.6×10^{16} atoms $\text{cm}^{-2} \text{s}^{-1}$. They found that the CVD films had a very low erosion yield (defined as the volume of material lost per oxygen atom impact), varying between 6.35×10^{-26} and $8.28 \times 10^{-26} \text{ cm}^3 \text{ atom}^{-1}$. Spectroscopic characterization revealed that the diamond surfaces were covered predominantly with ether groups, and to a lesser extent with carbonyl groups. In a series of articles⁶⁸⁻⁷², Shpilman et al studied the response of CVD diamond films subjected to both thermal (~ 0.04 eV mean energy) and hyperthermal (~ 5 eV mean energy) atomic oxygen etching. Exposure to thermal atomic oxygen resulted in the functionalization of the surface with oxygen containing groups such as ether, carbonyl and peroxides while no significant etching of the surface occurred. On the other hand, exposure to hyperthermal atomic oxygen resulted in the selective etching of (111) facets while (100) facets remained largely unaffected, indicating that diamond (100) surface is more resistant to hyperthermal atomic oxygen etching as compared to diamond (111) surface. Diamond (100) facets were etched only along their edges. Diamond (110) facets were also etched considerably, exhibiting crater like points on their surfaces and edges.

In parallel with experimental research, theoretical studies⁷³⁻⁷⁷ aimed at understanding the interactions of oxygen with diamond surfaces have been carried out in the past. These studies showed that, on diamond (100) surface, at monolayer coverage, oxygen atom in ether positions were the most favourable structure but with increase in temperature, carbonyl positions were more favourable due to entropic effects. Further, on (2x1) reconstructed diamond (100) surfaces, the increase in the oxygen coverage past half monolayer resulted in the gradual breaking of the surface reconstruction, resulting in (1x1) diamond (100) surface at a full monolayer coverage. Oxygen atoms were found to favour on top

positions (oxy radicals) on (1x1) diamond (111) surfaces while bridge positions were found to be energetically highly unfavourable. On the other hand, on (2x1) reconstructed diamond (111) surfaces, oxygen atoms were found to prefer a bridge positions (epoxides) till half a monolayer coverage, after which subsequent oxygen atoms preferred forming dioxetanes on the surface with the -O-O- dimer slightly rotated with respect to the underlying -C-C- bond. In recent articles⁷⁸⁻⁷⁹, Paci et al reported first principles based direct dynamics calculations of hyperthermal atomic oxygen collisions with diamond (100) and diamond (111) surfaces. In their calculations, they found that fully oxygenated diamond (100) surface was inert in nature with most of the colliding oxygen atoms either being scattered off the surface or forming an O₂ molecule via an Eley Rideal (ER) type reaction. No mechanism for the removal of a carbon atom was seen on diamond (100) surface. On the other hand, diamond (111) surface exhibited two mechanisms for the removal of a carbon atom from the surface. One of them involved the partial graphitization of the surface while the other involved a β -scission like process that resulted in the formation of a CO₂ molecule.

While a number of works in the past have tried to address the chemistry and dynamics of diamond oxidation, a comprehensive theoretical study of the etching of low index diamond surfaces (i.e., diamond (100), diamond (111) and diamond (110) surfaces) exposed to hyperthermal atomic oxygen has not been undertaken. In this work, classical molecular dynamics simulations using the ReaxFF reactive force field¹² are used to gain an atomically detailed understanding of the etching of low index diamond surfaces exposed to energetic oxygen atom collisions. A detailed description of the computational methods used in the simulations is presented in the next section followed by a discussion of the results and conclusions from the present study.

4.2 Computational Methods and Details

In order to identify various possible functional groups formed on the surface upon energetic oxygen atom collisions, following Paci et al⁷⁸, 100 independent 5eV energetic oxygen atom collisions each were performed on a representative diamond (100), diamond (111) and diamond (110) surface.

Diamond (100) surface consisted of 72 carbon atoms forming 6 atomic layers. The top surface of the slab was fully functionalized with oxygen atoms in the form of carbonyls while the bottom surface was (2x1) reconstructed and hydrogen terminated. Diamond (111) surface also consisted of 72 carbon atoms forming 6 atomic layers with 8 of the 12 carbon atoms on the top surface functionalized with oxygen atoms in the form of oxy radicals (atop oxygen atoms) while the bottom surface was hydrogen terminated. Diamond (110) surface consisted of 60 carbon atoms forming 5 atomic layers. The top surface was functionalized with 6 oxygen atoms in the form of epoxides while the bottom surface was hydrogen terminated. Figure 17 shows these structures used for oxygen collision simulations.

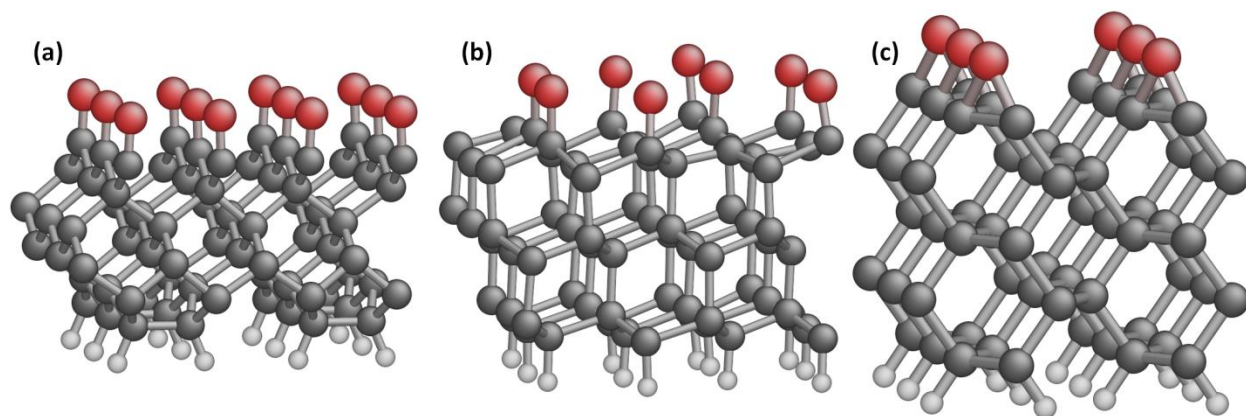


Figure 17: Structure of the diamond surfaces used in individual energetic oxygen atom collisions simulations. Carbon atoms are colored gray, oxygen atoms are colored red and hydrogen atoms are colored white. (a) Diamond (100) surface, (b) Diamond (111) surface and (c) Diamond (110).

Prior to oxygen functionalization, all the surfaces were relaxed, allowing for the lattice vectors in the in-plane directions (X and Y directions) to change, resulting in a zero strain structure. The lattice parameter in the surface normal direction was held fixed at a value of 90\AA . Later the surface was functionalized with oxygen atoms and the system was energy minimized again, holding the lattice vectors fixed. Note that diamond (100) began with a (2x1) reconstructed surface but the oxygen atoms on the surface led to the breaking of this surface reconstruction to form ketones as shown in fig 1a, in agreement with earlier theoretical calculations of Paci et al⁷⁸ and Petrini et al⁷⁵. After energy minimization, the surfaces were equilibrated at 298 K in NVT ensemble for a duration of 25 ps using a time step of 0.1 fs.

The temperature of the system was controlled using Berendsen thermostat⁴⁶ with a 100fs damping constant. Post equilibration, 100 independent oxygen atom collision simulations in NVE ensemble were performed on each of the surface for a duration of 1 ps. The origin of the oxygen atom trajectory was 5Å above the surface while its in-plane (X and Y) coordinates were chosen randomly. The impinging oxygen atoms were given a translational energy of 5eV, directed normal to the surface. Results from these simulations are discussed in the next section.

To obtain the rate of oxidative erosion of diamond surfaces upon hyperthermal oxygen atom impact, successive energetic oxygen atom collisions were carried out on larger bare diamond surfaces as shown in figure 18.

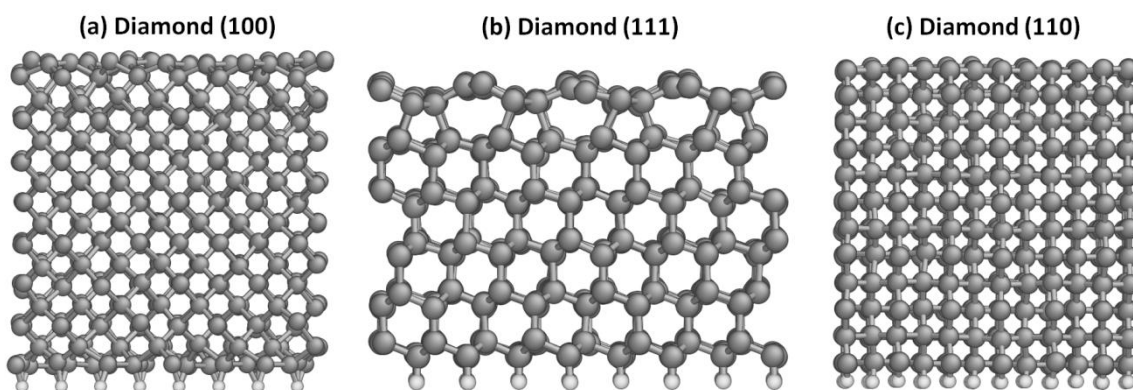


Figure 18: Structure of the diamond surfaces used in successive energetic oxygen atom collisions simulations. Carbon atoms are colored gray and hydrogen atoms are colored white. (a) Diamond (100) surface, (b) Diamond (111) surface and (c) Diamond (110) surface.

Diamond (100) surface contained 512 carbon atoms, diamond (111) surface contained 768 carbon atoms and diamond (110) surface contained 576 carbon atoms. The top side of diamond (100) and diamond (111) surfaces were (2x1) reconstructed while the bottom side of all the three surfaces was hydrogen terminated. Molecular dynamics simulations were carried out at 6 different surface temperatures from 1000K to 1500K, in intervals of 100K. Prior to molecular dynamics simulations, the systems were relaxed, allowing for the lattice vectors in the in-plane directions (X and Y directions) to change, resulting in a zero strain structure. The lattice parameter in the surface normal direction was held fixed at a value of 100Å. All the molecular dynamics simulations were performed in NVT ensemble using a time step of

0.1fs. The temperature of the surface was controlled using Berendsen thermostat with a 100fs damping constant. Post minimization, the system was first equilibrated at 300K for a duration of 60 ps. However, the potential energy and temperature values indicated that the surfaces had well equilibrated by 15 ps. Thus, post equilibration, temperature ramping simulations were initiated from 300K to the target temperature (between 1000K and 1500K) using atomic positions, velocities and accelerations from the equilibration simulation, harvested at 5ps intervals beginning at 15ps till 60 ps, giving us a total of 10 independent trajectories for every target temperature (i.e., a total of 60 trajectories). All the trajectories were further equilibrated at the target temperature for a duration of 15 ps before oxygen atom collisions were initiated.

In all the 60 simulations, oxygen atom trajectories were initiated 5Å above the surface while the in-plane coordinates (X and Y coordinates) of the oxygen atom were chosen randomly. The oxygen atoms were given a translational energy of 5eV directed normal to the surface. One oxygen atom trajectory was initiated every 250fs in the simulations, with the total simulation lasting for a maximum duration of 1.5ns (i.e. a maximum of 6000 5eV energetic oxygen atom collisions were simulated). A reflective wall was used in the surface normal direction (i.e., Z direction) because it would be unrealistic for any species leaving the diamond surface to enter the simulation cell from the bottom side and participate in the surface chemistry. Also, the bulk side of the specimen is inaccessible in experiments. Every 15ps (i.e., after 60 oxygen atom collisions), all the gas phase molecules were removed from the simulation cell. All the molecular images in this chapter were created using the AtomEye atomistic configuration viewer⁸⁰. A detailed discussion of the results from the simulations is presented in the next section.

4.3 Results and Discussions

Molecular dynamics simulations using the ReaxFF reactive force field have been performed to gain an atomically detailed understanding of the etching of low index diamond surfaces exposed to hyperthermal atomic oxygen. In an earlier article, Paci et al⁷⁸ had reported the statistics on various reactions occurring on a model diamond (100) and diamond (111) surface upon hyperthermal oxygen

atom impact in their molecular dynamics simulations using both SCC-DFTB⁸¹ and DFT methods. Their DFT simulations were performed using the SIESTA⁸² package employing the Double Zeta Polarized (DZP) basis set, Perdwe-Burke-Ernzerhof (PBE)^{44, 83} exchange correlational functional and Troullier-Martins type pseudopotentials⁸⁴⁻⁸⁵. Both their SCC-DFTB and DFT simulations were spin polarized triplet calculations, employing the Γ point to sample the Brillouin zone. Tables 3 to 5 below list the percentage of trajectories leading to various reactions from our ReaxFF calculations on model diamond surfaces (see fig 17 above and fig 5 of Paci et al⁷⁸) along with those reported by Paci et al⁷⁸. Note that SCC-DFTB and DFT calculations were reported by Paci et al⁷⁸ for diamond (100) and diamond (111) surfaces only. To the best of our knowledge, no such calculation is available for diamond (110) surface. Thus, only ReaxFF based results have been presented for diamond (110) surface in table 5.

	Diamond (100) surface		
	ReaxFF	SCC-DFTB	DFT
Ether formation	13	1	90
O ₂ formation	16	23	40
Inelastic O	11	74	0
Ozone like group	39	0	0
Peroxide radical formation	19	2	40
Tethered CO ₂ formation	2	0	0
Dioxetane formation	0	0	20

Table 3: Percentage of trajectories leading to various reactions on model diamond (100) surface using various methods

	Diamond (111) Surface		
	ReaxFF	SCC-DFTB	DFT
Oxy radical formation	8	43	70

O ₂ formation	75	43	20
Inelastic O	5	0	0
Dioxetane formation	17	0	0
Partial Graphitization	0	5	0
CO ₂ formation	0	1	10

Table 4: Percentage of trajectories leading to various reactions on model diamond (111) surface using various methods

	Diamond (110) surface
	ReaxFF
Ether formation	19
Oxy radical	46
O ₂ formation	19
Inelastic O	11
Dioxetane formation	5

Table 5: Percentage of ReaxFF trajectories leading to various reactions on diamond (110) surface

From the above tables, it is clear that ReaxFF is able to reproduce most of the reactions seen in DFT and SCC-DFTB trajectories, albeit with a broader distribution of probabilities. Some of the structures resulting from ReaxFF based trajectories are shown in figure 19.

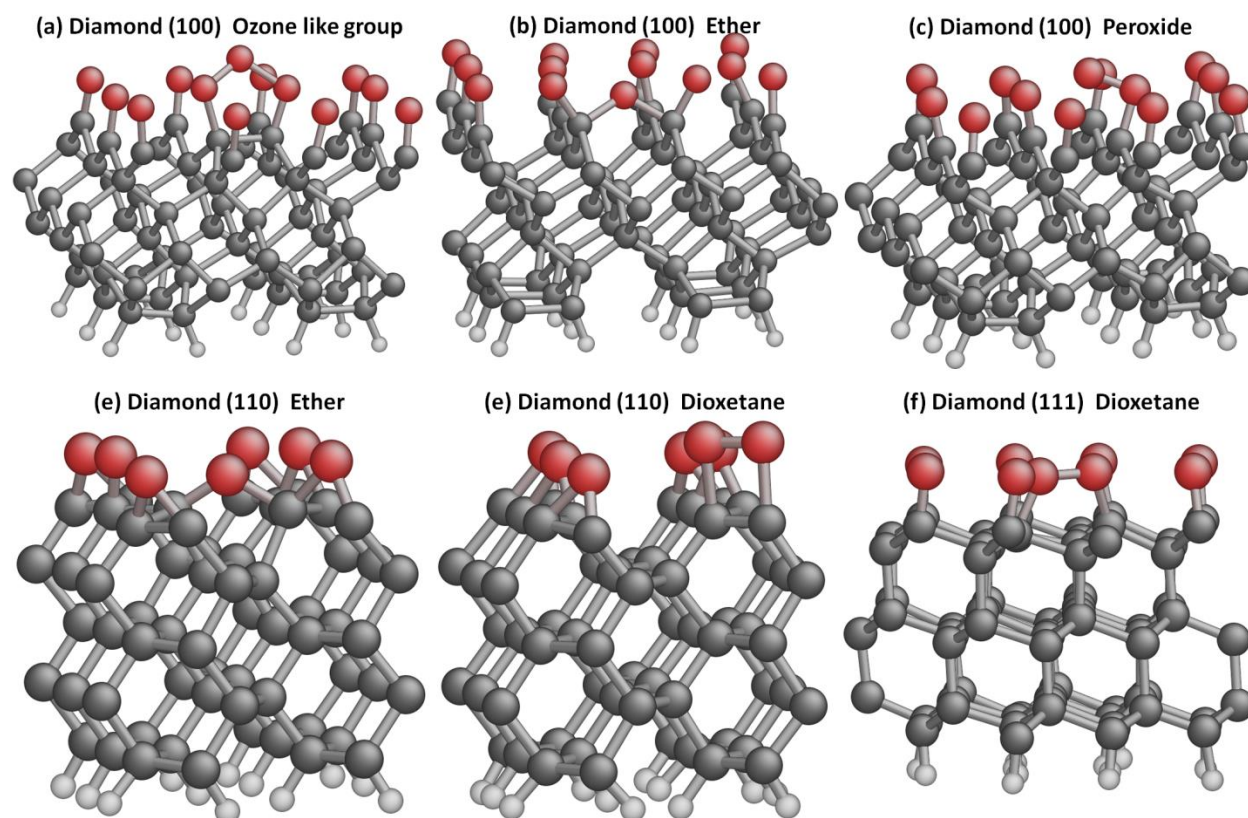


Figure 19: Some structures resulting from ReaxFF simulations of individual hyperthermal oxygen atom collisions with model diamond surfaces

Of the 100 trajectories simulated for diamond (100) surface using ReaxFF, 16% of the trajectories resulted in the formation of an O_2 molecule while 11% of the trajectories resulted in the inelastic scattering of the incoming O atom. In contrast to ReaxFF trajectories, SCC-DFTB trajectories showed a much higher probability of inelastic scattering of the incoming O atom while the DFT trajectories presented no instance of inelastic scattering. O_2 formation in all the ReaxFF trajectories occurred via an Eley-Rideal (ER) direct reaction mechanism wherein the incoming oxygen atom plucked a surface oxygen atom to form an O_2 molecule. 19% of the ReaxFF trajectories resulted in the formation of a peroxide radical (fig 19c) while 40% of the DFT trajectories resulted in the formation of a peroxide radical and only 2% of the SCC-DFTB trajectories formed peroxide. While peroxide formation in all the DFT trajectories was accompanied by (2x1) surface reconstruction of the underlying carbon atoms, only 3 of the 19 ReaxFF trajectories showed this event. 39% of the ReaxFF trajectories resulted in formation of

an ‘ozone like’ functional group (or -C-O-O-O-C- bridge) on the surface (fig 19a) while none of the SCC-DFTB or DFT trajectories seem to witness this functional group. The formation of this ‘ozone like’ group is accompanied by the (2x1) surface reconstruction of the underlying surface carbon atoms. The formation energy of this structure was computed using ReaxFF and DFTB as $E_f = E_{\text{ozone-like}} - E_{\text{surf}} - E_{\text{O-atom}}$, where $E_{\text{ozone-like}}$ is the energy of the geometry optimized structure of the configuration shown in figure 19a, E_{surf} is the energy of the oxygen terminated diamond (100) surface shown in fig 19a and $E_{\text{O-atom}}$ is the energy of an oxygen atom. To calculate the SCC-DFTB energies, firstly (2x1) reconstructed diamond (100) surface was relaxed, allowing for the cell parameters in the in-plane directions (X and Y directions) to change while holding the cell parameter in the surface normal direction (Z direction) to a fixed value of 30Å, resulting in a zero strain structure. The SCC-DFTB calculations utilized the pbc-0-3 parameter set⁸⁶.⁸⁷ Following this, the surface was functionalized with oxygen atoms and then optimized to obtain E_{surf} and $E_{\text{ozone-like}}$ while holding the cell parameters fixed. In all the calculations, the Brillouin zone was sampled using a 4x4x1 kpoint mesh. The formation energy of the ‘ozone like’ group was found to be -1.602 eV using ReaxFF while SCC-DFTB gave a value of -4.581 eV, indicating that both the methods predict this structure to be a local minimum. It is to be noted that none of the SCC-DFTB or DFT trajectories seem to show this event. This warrants a more systematic study of the effect of kpoint and the effect of spin states on the results of the SCC-DFTB and DFT trajectories. 13% of the ReaxFF trajectories showed the formation of an ether group as shown in fig 19b while 90% of the DFT trajectories and 1% of the SCC-DFTB trajectories showed ether formation. 2% of the ReaxFF trajectories resulted in the formation of a tethered CO₂ molecule (or a ‘carboxyl like’ group) wherein the incoming oxygen atom attached to the carbon atom of a ketone on the surface and breaking the C – C bond between the surface and the sub-surface carbon atom. 20% of the DFT trajectories report the formation of a dioxetane group.

Of the 100 trajectories simulated for diamond (111) surface using ReaxFF, 75% of them resulted in the formation of an O₂ molecule via an ER direct reaction mechanism. In comparison, 43% of the SCC-DFTB trajectories resulted in the formation of an O₂ molecule while 20% of DFT trajectories formed O₂. 8% of the ReaxFF trajectories resulted in oxy radicals (or an ‘atop’ oxygen) wherein the incoming oxygen

bound to an un-functionalized carbon atom on the surface. 43% of the SCC-DFTB trajectories and 70% of the DFT trajectories showed this event. 17% of the ReaxFF trajectories resulted in the formation of a dioxetane on the surface resulting from a bond formed between an oxy radical on the surface and an oxy radical formed by the incoming oxygen atom on a neighboring unfunctionalized carbon atom, as shown in figure 19f. 5% of the ReaxFF trajectories resulted in the inelastic scattering of the incoming oxygen atom. Neither of these two events was seen in the SCC-DFTB and DFT trajectories. 5% of the SCC-DFTB trajectories resulted in partial graphitization wherein a C – C bond between a surface and a sub-surface carbon atom was broken. 1% of the SCC-DFTB trajectories formed a CO₂ molecule while 10% of the DFT trajectories resulted in the same.

Since no DFT and SCC-DFTB trajectories are available for diamond (110) surface, results from ReaxFF trajectories alone are discussed here. Of the 100 trajectories, 19% of the trajectories resulted in the formation of an ether group as shown in figure 19d, along with breaking the C – C bond in the neighboring epoxides. In 46% of the trajectories, the incoming oxygen atom broke an epoxide on the surface to form two oxy radicals bound to adjacent carbon atoms on the surface that initially constituted the epoxide. 19% of the trajectories resulted in the formation of an O₂ molecule via an ER direct reaction mechanism. 11% of the trajectories resulted in inelastic scattering of the oxygen atom while 5% of the trajectories formed a dioxetane as shown in figure 19e (instead of forming two oxy radicals, the incoming oxygen atom was captured into a -C-O-O-C- ring). From the above results, it is clear that ReaxFF is able to capture the wide variety of chemistry possible on diamond surfaces. While individual trajectory simulations gave useful information on the nature of functional groups on the surface of diamond, they are unable to provide any data on the erosion rate of these surfaces subjected to hyperthermal oxygen atom impacts. To quantify the erosion rates of these surface, successive oxygen atom collisions were carried out on larger diamond surfaces, as discussed in the previous section.

Successive oxygen atom collisions on diamond surfaces indicated that all the 3 low index surfaces can be etched by hyperthermal atomic oxygen. The etching of all the three surfaces was observed to be a layer

by layer phenomenon. Figures 20 to 22 show a sequence of states through which the diamond surfaces proceed when subjected to hyperthermal atomic oxygen collisions at 1000K surface temperature.

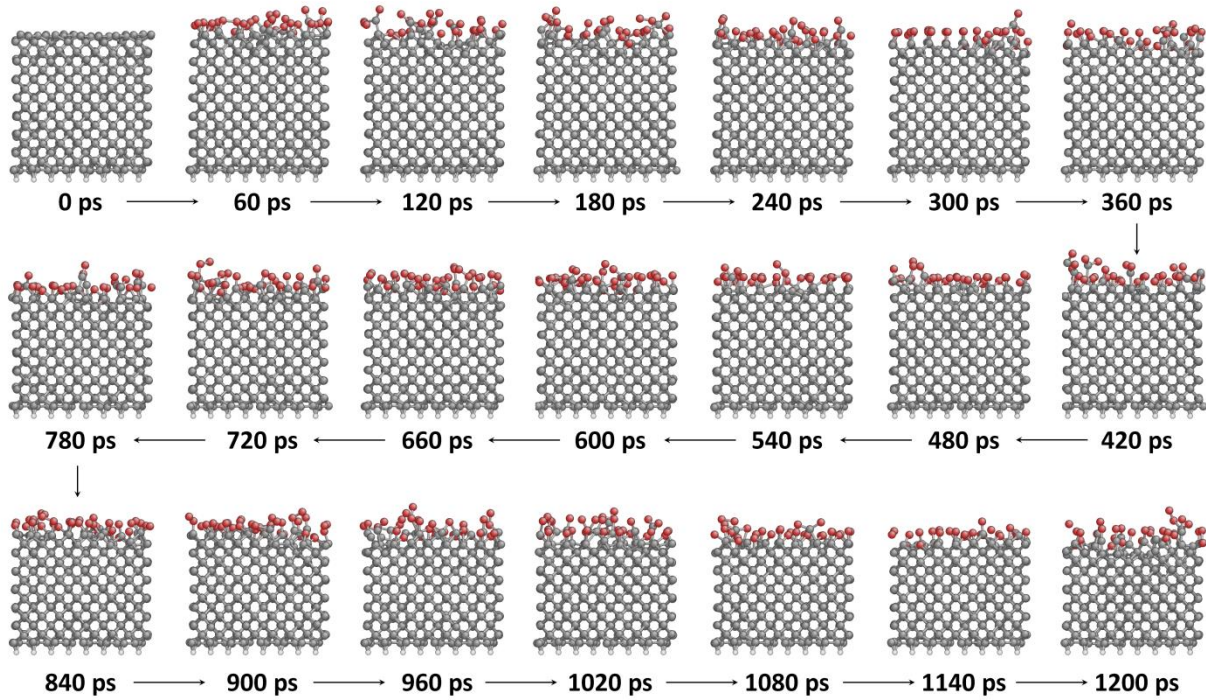


Figure 20: A sequence of states through which a diamond (100) surface proceeds upon hyperthermal atomic oxygen collision at 1000K.

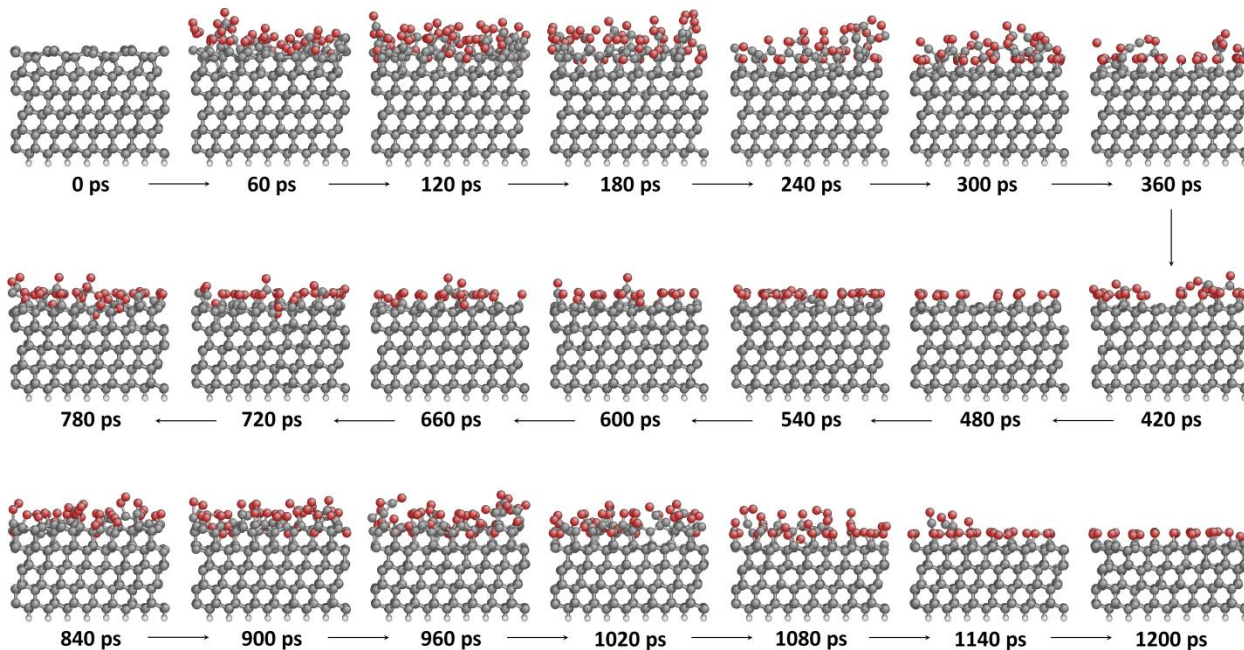


Figure 21: A sequence of states through which a diamond (111) surface proceeds upon hyperthermal atomic oxygen collision at 1000K.

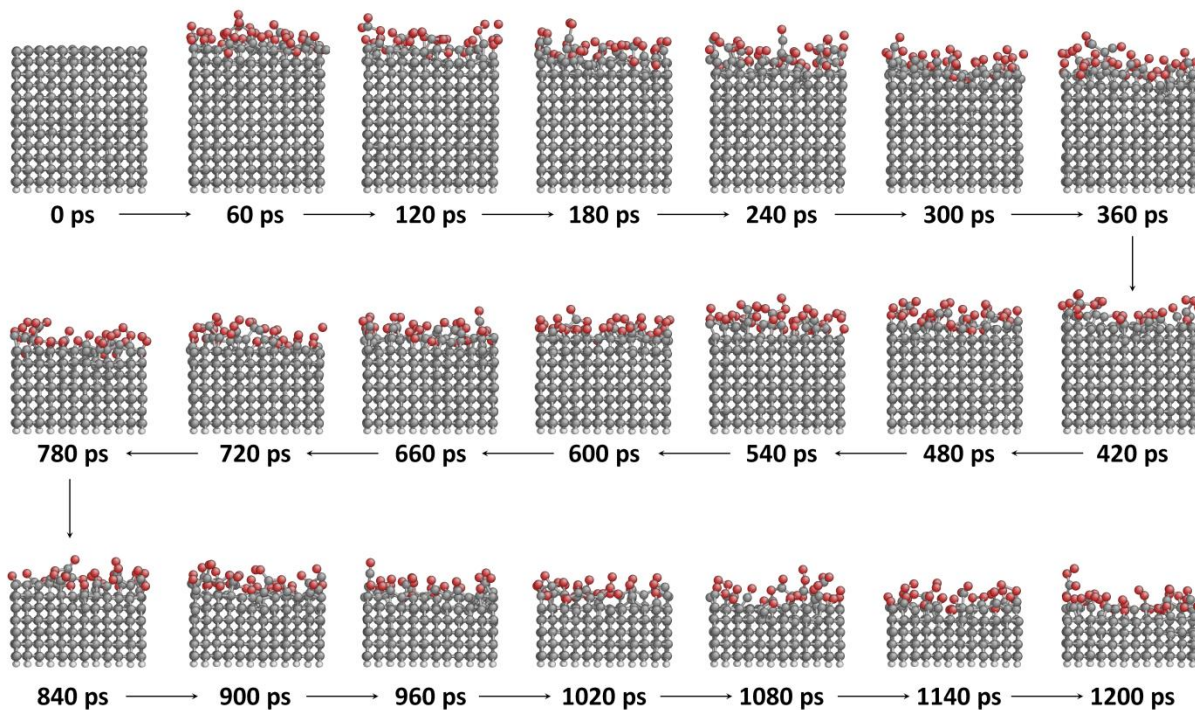


Figure 22: A sequence of states through which a diamond (110) surface proceeds upon hyperthermal atomic oxygen collision at 1000K.

The etching of diamond (100) and diamond (110) surfaces by hyperthermal atomic oxygen proceeded via the functionalization of the bare carbon surface by oxygen atoms followed by the loss of CO₂ molecules predominantly and CO molecules to a lesser extent. While we began with (2x1) reconstructed diamond (100) surface, soon all the surface reconstruction was broken due to the formation of various oxygen functional groups, and during the course of etching, the surface carbon atoms were unable to regain the (2x1) reconstruction. This is in contrast to the observations of Loh et al⁶¹ and Pehrsson et al⁶² who found that during thermal oxidation of diamond (100) surfaces, at substrate temperatures larger than 850 °C, the surface regained its (2x1) reconstruction or developed a graphitic overlayer. The etching of diamond (111) surface began with the formation of oxygen functional groups on the surface. While we began with (2x1) reconstructed diamond (111) surface, the surface quickly transformed into (1x1) diamond (111) due the energy imparted by 5eV oxygen atom collisions. Subsequent reconstruction of the oxygen functionalized (1x1) diamond surface did not occur in our simulations. This is consistent with earlier DFT calculations that indicated the transformation of oxygen functionalized (1x1) diamond (111) surface into a (2x1) pattern is associated with a very high energy barrier⁷⁶. During the course of the simulation, a number of C-C bonds between the carbon atoms in the surface layer and those in the sub-surface layer broke, resulting in the partial graphitization of the surface. It is now well known that diamond (111) surface is prone to graphitization⁸⁸⁻⁹⁰. Further, partial graphitization of diamond (111) surface has also been observed in molecular beam experiments⁷², which relate most closely to the simulations in this work. While the surface undergoes graphitization, at some point in time vacancy defects are created on the surface due the loss of one or more carbon atom in the form of a CO₂ or CO molecule. Once a few defects are formed on the surface, the surface layer etches away rapidly, much like the rapid etching of graphite basal plane by atomic oxygen^{23, 26, 28, 41, 43}. Figures 23 to 25 show the number of carbon atoms lost from all the three diamond surfaces as a function of time, expressed as the ratio of number of carbon atoms lost to the initial number of atoms (1-N/N₀, N₀ = 512 for diamond (100), 768 for diamond (111) and 576 for diamond (110)). Results from all the 60 trajectories (6

surface temperatures, 10 independent trajectories at each surface temperature) for each surface are plotted in these figures.

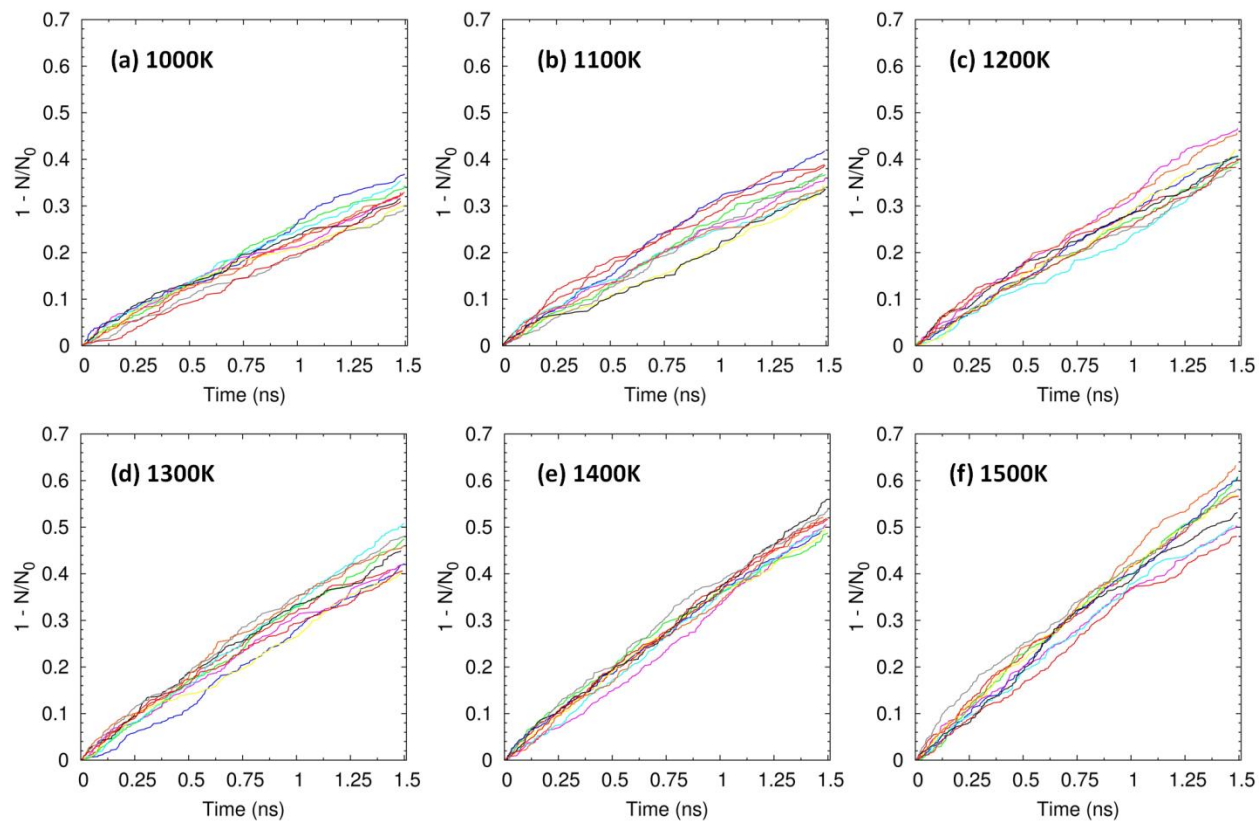


Figure 23: Number of carbon atoms lost from diamond (100) upon hyperthermal atomic oxygen etching, expressed as a ratio of the number of carbon atoms lost to the initial number of carbon atoms

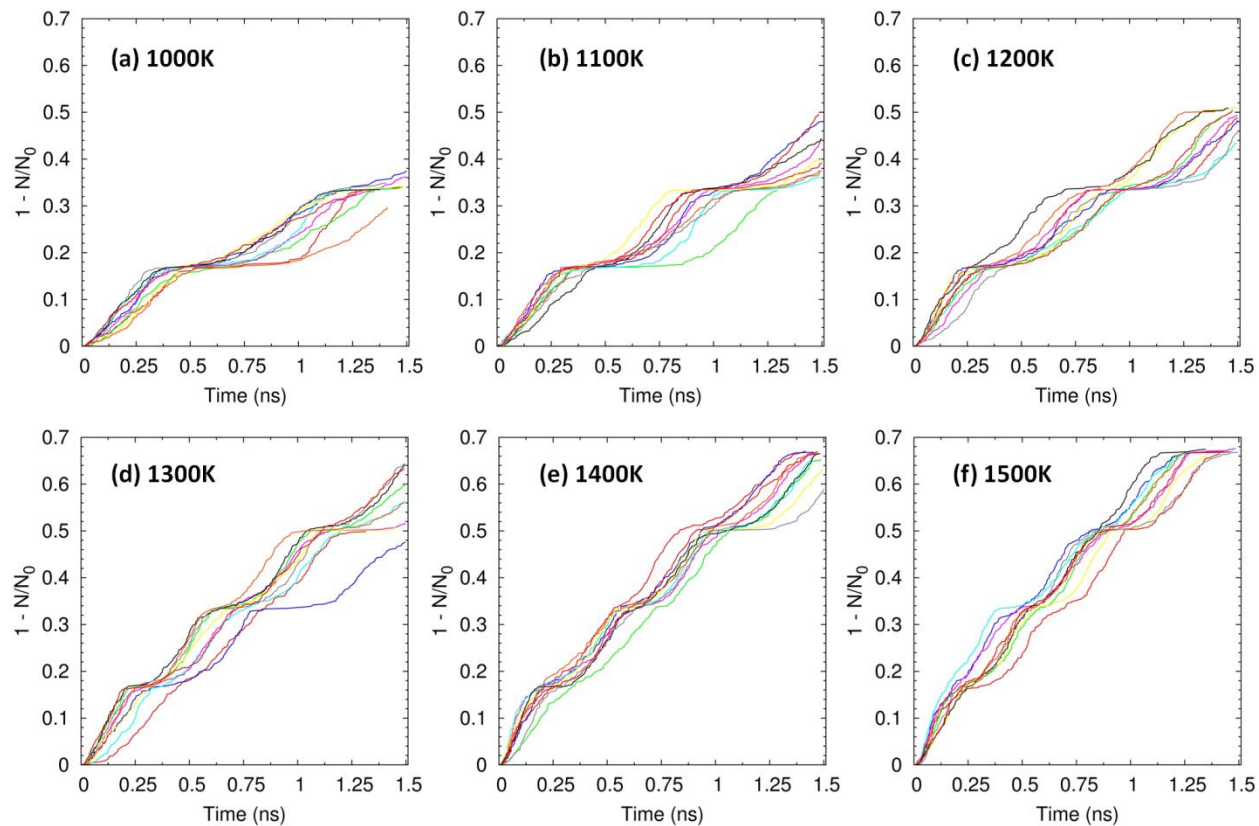


Figure 24: Number of carbon atoms lost from diamond (111) upon hyperthermal atomic oxygen etching, expressed as a ratio of the number of carbon atoms lost to the initial number of carbon atoms

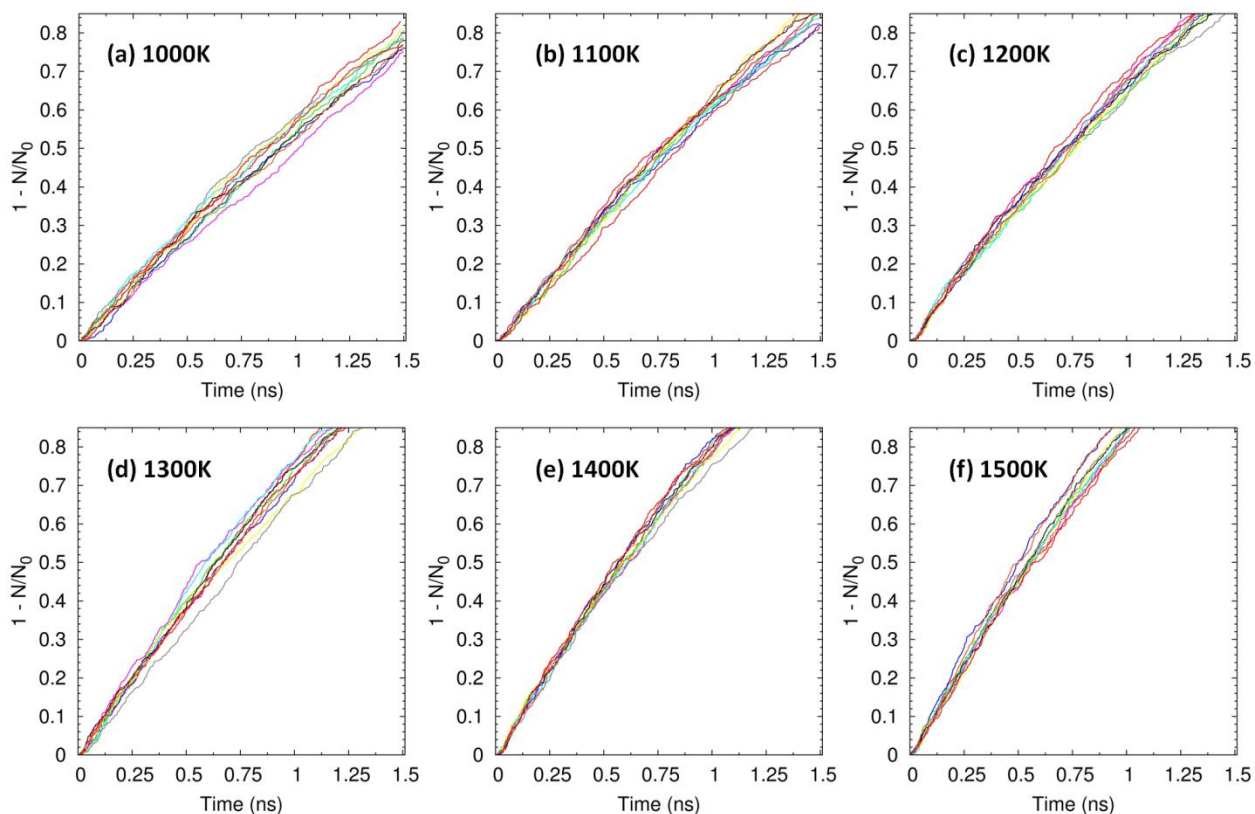


Figure 25: Number of carbon atoms lost from diamond (110) upon hyperthermal atomic oxygen etching, expressed as a ratio of the number of carbon atoms lost to the initial number of carbon atoms

We see from figures 23 and 25 that the rate of loss of carbon atoms from both diamond (100) and diamond (110) are linear functions of time while a ‘wavy’ pattern is observed for the diamond (111) surface due to a temporary slowdown in the rate of carbon atom loss from diamond (111) surface till a few vacancy defects are formed on the surface layer after which it etches away rapidly. During this slowdown, most of the impinging oxygen atoms end up undergoing one of the many reactions discussed earlier for the diamond (111) surface while the surface itself continues to undergo graphitization. Figure 26 below depicts this process in detail from one of the diamond (111) etching trajectories at 1000K surface temperature. The simulation snapshots in the figure numbered (1) to (7) correspond to the times 1 – 7 indicated on the plot on figure 26(a). While this phase in the etching of diamond (111) is apparent at

all the surface temperatures that we simulated, clearly, the duration of this phase for each layer of diamond (111) slab reduces with increase in temperature.

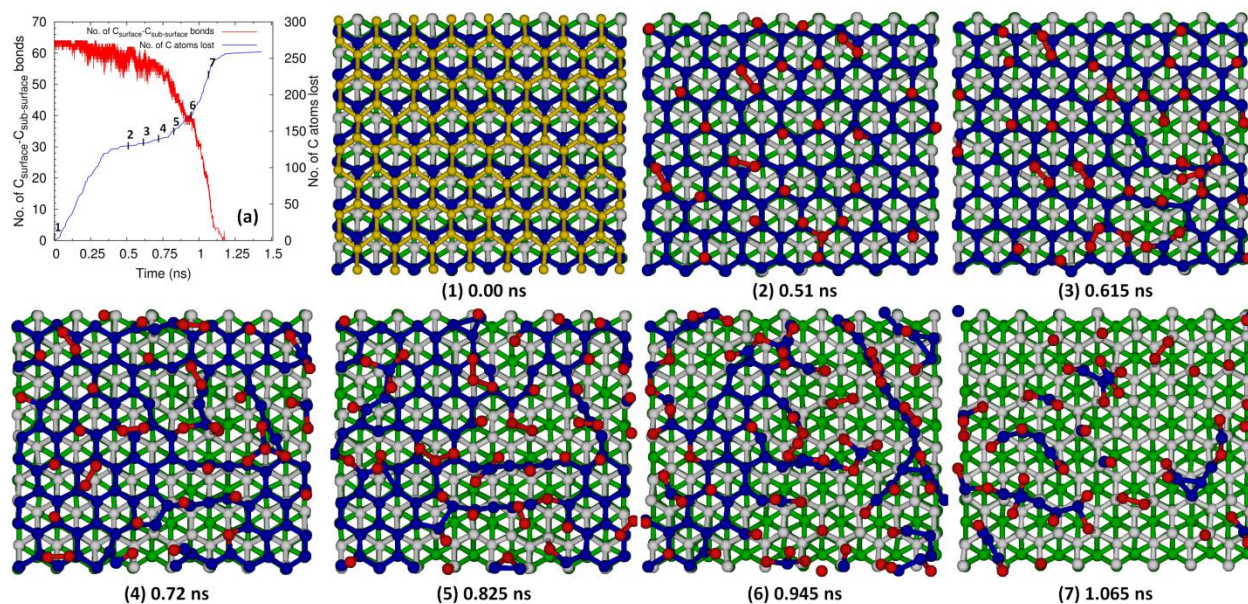


Figure 26: Etching of a layer of diamond (111) surface by hyperthermal atomic oxygen. Oxygen atoms are colored red while carbon atoms in the 1st surface layer are colored yellow, carbon atoms in the 2nd layer are colored blue, carbon atoms in the 3rd layer are colored white and carbon atoms in the subsequent layers underneath are colored green

At time zero, we begin with a bare diamond (111) surface (fig. 10(1)) which etches away completely by about 0.5ns. During this time, particularly beyond 0.2ns, C-C bonds between the 2nd and the 3rd surface layers start to break as more of the 2nd layer becomes exposed (see fig 26(a)). During the time period for 0.51 to 0.72 ns (figs. 26(2) to 26(4)) more of C-C bonds break along with the loss of a few carbon atoms creating vacancy defects on the surface. Beyond this time, the surface rapidly etches away with the entire layer being eroded by ~ 1.1 ns. During the time period between 0.51ns and 0.825ns (figs. 26(2) to 26(5)), 21 carbon atoms were lost from the surface while 76 carbon atoms were lost in the time period between 0.825ns and 1.065ns (figs. 26(5) to 26(7)), showing the acceleration in the etching process. Correspondingly, there is a sharp decrease in the number of C-C bonds between the atoms in the 2nd and 3rd layer, as shown in figure 26(a). Irrespective of the nature of etching, however, we see that all

the diamond surfaces can be continuously etched using hyperthermal atomic oxygen, albeit at different rates.

In order to obtain the rate of loss of carbon atoms from diamond surfaces, a linear equation of the form $1-N/N_0 = k*t$ was fit to each of the curves in figures 23 to 25. The rate of carbon atom loss from each surface at any simulated temperature was taken to be the average of rates of carbon atom loss obtained from the ten independent trajectories at that temperature. These rates were then used in an Arrhenius type expression to obtain the activation energy and the frequency factor for carbon atom loss from the three surfaces. Table 6 below lists the rates obtained for each surface along with their activation energy and frequency factor while figure 27 shows the Arrhenius fit to the rates computed at each temperature for all the three surfaces.

Surface Temperature (K)	Rate of loss of carbon atoms (ns⁻¹)		
	Diamond (100)	Diamond (111)	Diamond (110)
1000	0.2267	0.2624	0.5445
1100	0.2584	0.2993	0.6024
1200	0.2825	0.3453	0.6638
1300	0.3110	0.4233	0.7400
1400	0.3566	0.4819	0.8208
1500	0.3924	0.5496	0.8925
Activation Energy (kcal/mol)	3.221	4.513	2.973
Frequency factor (atom s⁻¹)	5.75×10^{11}	1.86×10^{12}	1.37×10^{12}

Table 6: Rate of carbon atom loss from diamond surfaces and their Arrhenius parameters

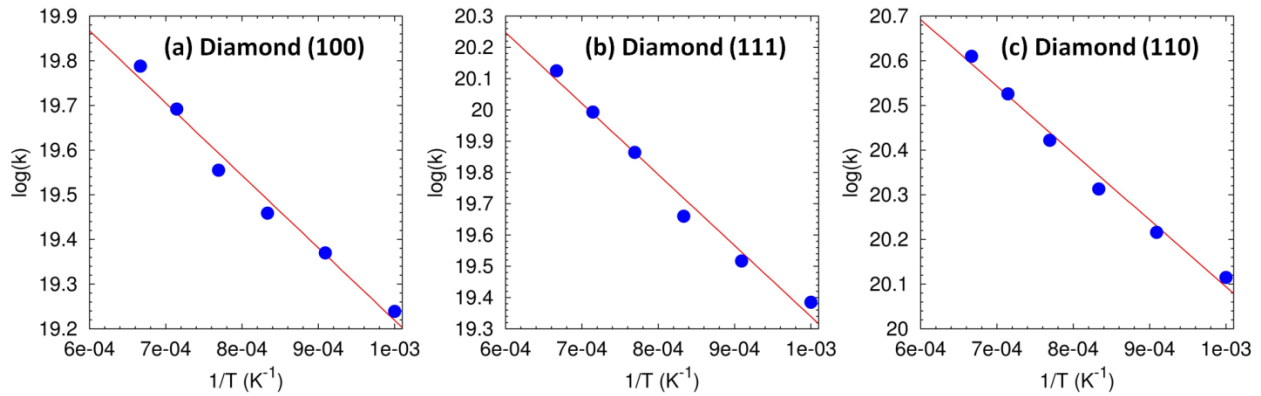


Figure 27: Arrhenius fit to the rate of carbon atom loss from diamond surfaces subject to hyperthermal atomic oxygen etching. In all the plots, the blue circles correspond to data from our simulations while the red line corresponds to the Arrhenius fit to the data.

Comparing the activation energy for etching of diamond surfaces shown in table 6 with those for the thermal oxidation of diamond (100)^{58, 60, 63-64} and diamond (111)⁶⁴⁻⁶⁵, we see that under hyperthermal atomic oxygen collisions, the activation energies are reduced by an order of magnitude. This indicates that diamond surfaces, though oxidation resistant at thermal conditions, can undergo significant etching at hyperthermal conditions. Figure 28 below shows the erosion yield of diamond surfaces computed using the rates from table 6. The erosion yield of graphite basal planes from the previous chapter is also shown for comparison.

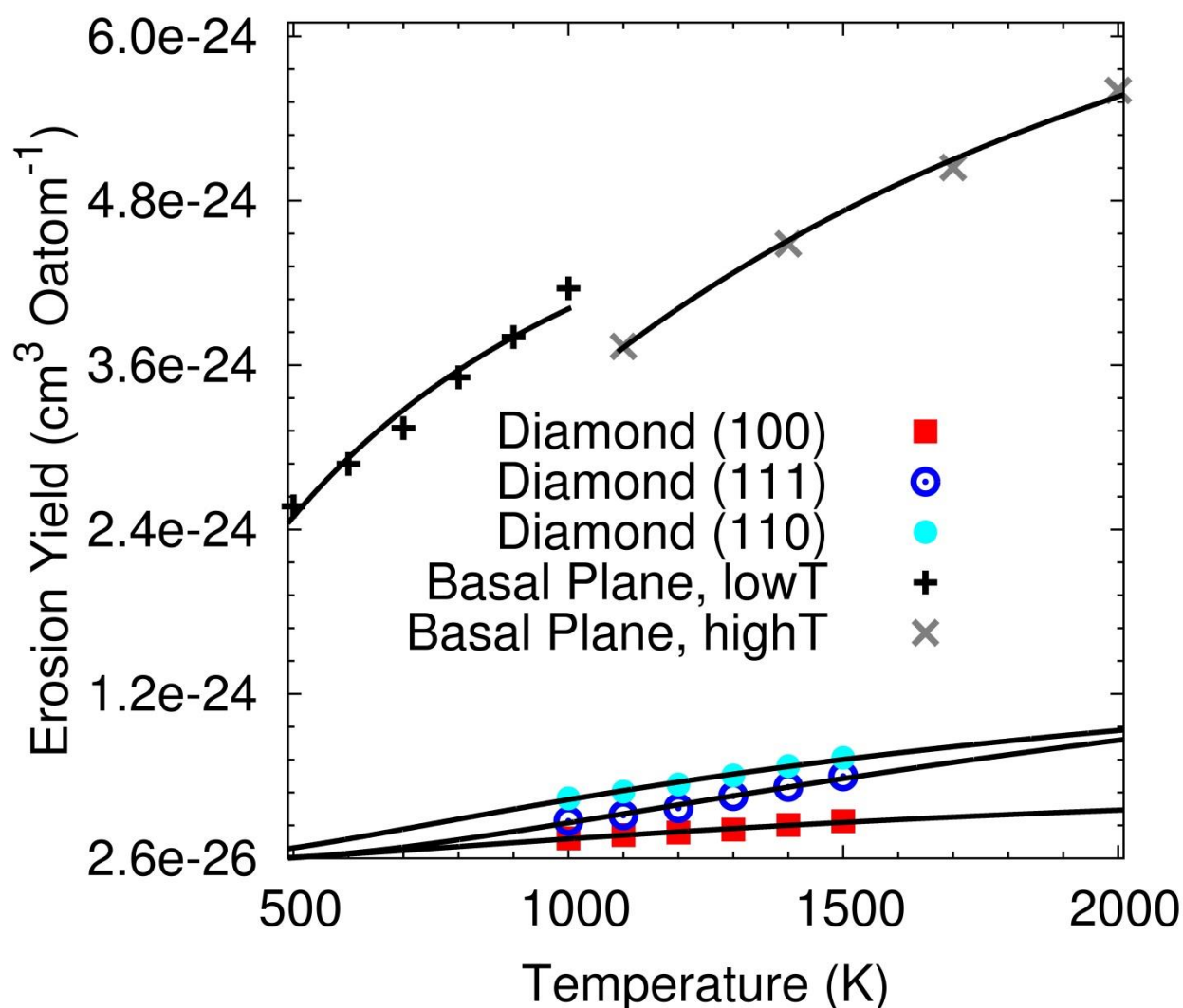


Figure 28: Erosion yield of diamond surfaces upon hyperthermal atomic oxygen etching plotted along with the erosion yield of graphite basal plane. The points correspond to the data from the simulations while the solid lines correspond to the Arrhenius fit to the erosion yield.

From figure 28, we can see that diamond (100) surface is the most resistant to etching followed by diamond (111) surface while diamond (110) surface is the least resistant to atomic oxygen etching. However, the activation energy for the loss of a carbon atom from diamond (111) surface is larger than that from diamond (100) surface (see table 6), indicating that the loss of a carbon atom from diamond (111) is more strongly temperature dependent than diamond (100). This is consistent with earlier experimental works^{58, 64-65} and the fact the rate of graphitization of diamond (111) surface increases with increase in temperature and graphite basal planes can be etched by atomic oxygen easily. Extrapolating

the erosion yield of diamond (111) surface to 500K, we get a value of $2.93 \times 10^{-26} \text{ cm}^3 \text{ Oatom}^{-1}$, in very good agreement with experimental erosion yields^{66-68, 71-72} that vary between 2×10^{-26} to $8.28 \times 10^{-26} \text{ cm}^3 \text{ Oatom}^{-1}$. Comparing this with the erosion yield of graphite (between $4 \times 10^{-25} \text{ cm}^3 \text{ Oatom}^{-1}$ and $1.1 \times 10^{-24} \text{ cm}^3 \text{ Oatom}^{-1}$)^{26, 28}, amorphous carbon (between $3 \times 10^{-26} \text{ cm}^3 \text{ Oatom}^{-1}$ and $1.8 \times 10^{-24} \text{ cm}^3 \text{ Oatom}^{-1}$)⁹¹ and polymers like kapton H polyimide ($3 \times 10^{-24} \text{ cm}^3 \text{ Oatom}^{-1}$)⁴⁸, we see that the diamond surfaces are 1 to 2 orders of magnitude more resistant to hyperthermal atomic oxygen etching. Thus, diamond thin films, with predominantly diamond (100) oriented grains are promising candidates for the surfaces of space crafts exposed to LEO environment.

4.4 Summary

In summary, molecular dynamics simulations have been carried out using the ReaxFF reactive force field to gain an atomically detailed insight into the etching of diamond surfaces by hyperthermal atomic oxygen. Molecular dynamics simulations on small model diamond surfaces showed that a variety of functional groups such as ethers, peroxide radicals, oxy radicals and dioxetanes can form on these surfaces upon exposure to atomic oxygen, in agreement with both theoretical and experimental studies reported earlier. Molecular dynamics simulations on larger diamond surfaces indicated that all the three low index surfaces, namely diamond (100), diamond (111) and diamond (110) can be etched by hyperthermal atomic oxygen. The etching of all the surfaces was observed to be a layer by layer phenomenon. While the etching of diamond (100) and diamond (110) proceeded by formation of oxygen functional groups on the surface followed by the loss of carbon atoms in the form of a CO_2 or CO molecule, the etching of diamond (111) surface proceeded by the simultaneous graphitization and functionalization of the surface with oxygen atoms. Subsequently, once a few vacancy defects were formed, the surface layer etched away rapidly, much like the etching of graphite basal planes by atomic oxygen. The simulations were then used to obtain an Arrhenius type rate law for the loss of carbon atoms from the surface. The erosion yield of diamond surfaces indicated that diamond (110) is the least resistant and diamond (100) is the most resistant surface to atomic oxygen etching, in agreement with earlier

experimental observations. Nevertheless, the erosion yield of all the diamond surfaces were 1 to 2 orders of magnitude smaller than Kapton H polyimide, a commonly used material on the surface of spacecrafts in LEO environment, indicating that diamond thin films with predominantly diamond (100) oriented grains could be a promising material for such applications.

5

Development of ReaxFF_{SiO}^{GSI} for Oxygen–Silica Gas Surface Interactions

4.1 Introduction

(Parts of this chapter were published in Kulkarni et al⁹²)

On account of its low thermal conductivity, high melting temperature, and low catalytic activity, silica is a significant component in many reusable and ablative thermal protection systems for high-speed aerospace vehicles. For example, most current high-temperature oxidation-protection systems for leading edges on hypersonic vehicles involve silica-based or silica-forming coatings (e.g., the reinforced carbon-carbon systems used on the Space Shuttle and the X-43A research aircraft vehicle). Furthermore, natural silica oxides (SiO_2) form on SiC , Si_3N_4 , and most Ultra High Temperature Ceramic (UHTC) composite systems under conditions similar to those of earth re-entry⁹³⁻⁹⁴. In hypersonic flight, the gas layer between the bow shock and the surface of the vehicle can reach temperatures of several thousand kelvins leading to the vibrational excitation and dissociation of diatomic molecules (O_2 and N_2 primarily). These gaseous species reach the surface of the vehicle in a dissociated highly non equilibrium state. The surface of the vehicle acts as a catalyst for the exothermic recombination of these dissociated species, increasing the overall heating on the thermal protection system of the vehicle. It has been shown that this heterogeneous recombination can contribute up to 30% of the total heat load for Earth reentry⁹⁵. Despite a large body of experimental work^{93, 96-101}, the fundamental processes occurring on silica surfaces exposed to atomic and molecular oxygen are still uncertain. Molecular dynamics based simulations can provide atomistically detailed insight into the mechanisms that contribute to the heterogeneous recombination of oxygen species on silica surfaces. Such simulations based on empirical potentials¹⁰²⁻¹⁰⁶ have been used in the past to study the gas surface interactions of oxygen atoms and molecules with silica surfaces. A number of empirical force fields describing Si-O systems have been developed in the past¹⁰⁷⁻¹¹¹, and they have been successful in describing the structures and energies of various polymorphs of silicon and silicon oxides.

Specifically, the BKS potential¹⁰⁹ has been used for simulating bulk silica and silica surfaces¹¹². Although these force fields provide valuable insights into the dynamics of silica polymorphs and their chemistry, they are applicable only close to the equilibrium structures of the morphologies against which they were parameterized. This imposes a severe restriction on the transferability of these potentials and their ability to simulate chemical reactions.

To describe the structures, properties, and chemistry of silicon and silicon oxide materials, ReaxFF_{SiO} was developed by van Duin et al¹¹³. Since its development, ReaxFF_{SiO} has been successfully used to study such diverse phenomena such as the thermal decomposition of PDMS polymers¹¹⁴, crack propagation¹¹⁵, brittle to ductile transitions in silicon crystals¹¹⁶, self-assembly of silica nanocages into an inorganic framework with potential applications as capacitors and heterogeneous catalysts¹¹⁷ and hyperthermal oxygen atom interaction with silicon surfaces and nanowires¹¹⁸⁻¹²¹. Although ReaxFF_{SiO} has been developed and used extensively, it was not specifically parameterized for gas–surface interactions. In this work, ReaxFF_{SiO} potential for silica has been extended to describe the chemistry and dynamics in oxygen–silica gas–surface interactions (GSI). This extended potential is referred to as ReaxFF_{SiO}^{GSI}.

4.2 Gas – Surface Model Systems and DFT based Binding Energy Curves

Cluster models representing the interaction of atomic and molecular oxygen were selected from reconstructed (001) α -quartz and several defects occurring on silica surfaces. The cleaved (001) α -quartz surface is known to undergo reconstruction into a well ordered (1x1) pattern at room temperature¹²². Figure 29 shows the cleaved and reconstructed (001) α -quartz surface as obtained from ReaxFF simulations after geometry optimization.

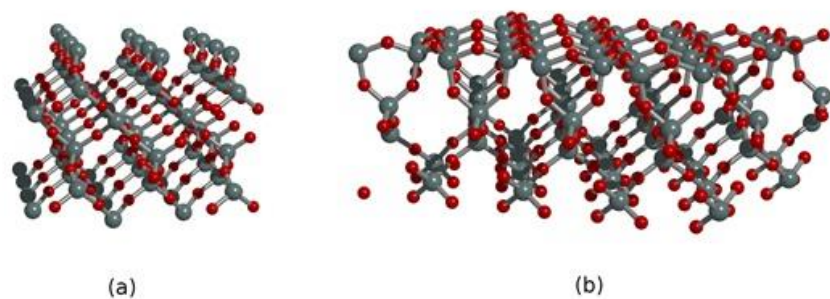


Figure 29: (a) Cleaved (001) α -quartz surface. (b) Reconstructed (001) α -quartz surface. Oxygen atoms are red, and silicon atoms are gray.

Non defective cluster models representing the site over a fully coordinated surface silicon atom (S) and the site over a bridging oxygen atom (B) were chosen to represent the reconstructed (001) α -quartz surface while defective cluster models representing an under-coordinated surface silicon atom or a non-bridging oxygen atom were chosen to represent surface defects occurring on silica surfaces. A notation 'Tn-A + B' was chosen for these models where 'n' represents the number of silicon atoms, 'A' is the relevant surface site represented by the cluster and 'B' denotes the O/O₂ species (as the case maybe) interacting with the cluster. Figure 30 shows the non-defective clusters representative of the (001) α -quartz surface while figure 31 shows the defective clusters representative of surface defects on silica.

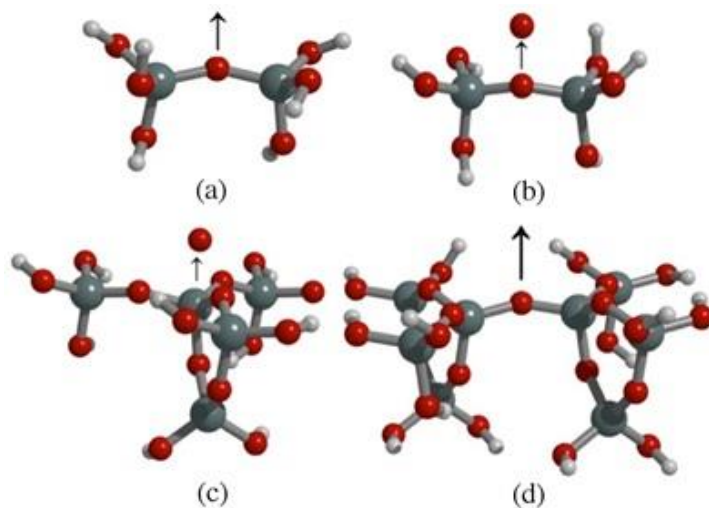


Figure 30: Non-defective clusters. (a) T2-B1, (b) T2-B1+O, (c) T5-S1+O, (d) T8-B1

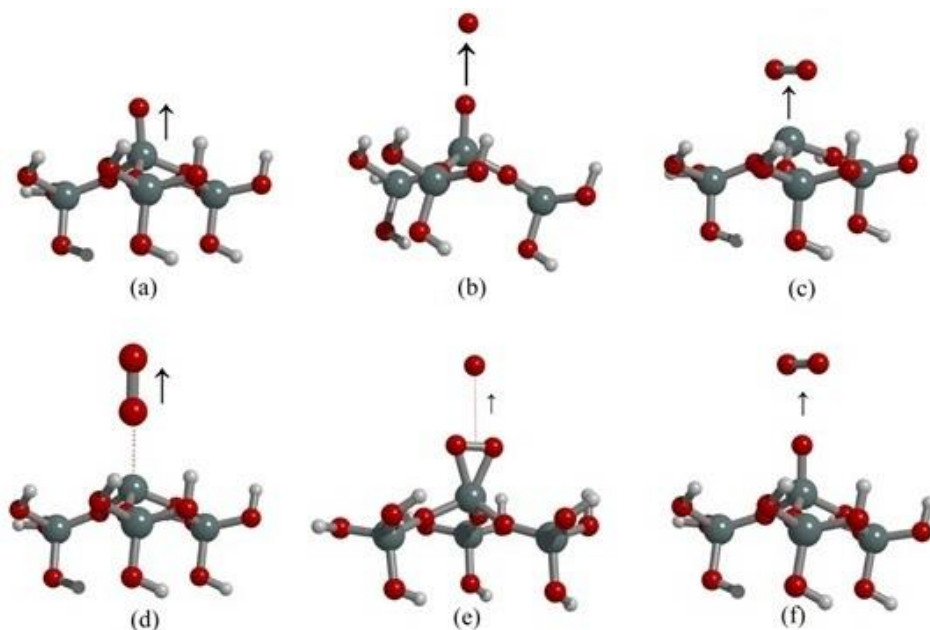


Figure 31: Defective Clusters: (a) T4-O, (b) T4-O+O, (c) T4-O2||, (d) T4-O2L, (e) T4-O2||+O, (f) T4-O+O2||

Single point energies for the approach of an oxygen atom (or molecule as the case maybe) in various configuration shown above were calculated to obtain the binding energy curve with a convenient reference chosen separately for each system. Singlet and triplet curves were calculated for the non – defective clusters that contain an even number of electrons while doublet and quartet curves were calculated for defective clusters consisting of an odd number of electrons. The density functional calculations employed M06-2X¹²³ functional for the non – defective clusters and M06-L¹²⁴ for the defective clusters in def2-TZVP basis¹²⁵. The binding energy curves along with those from ReaxFF_{SiO} and ReaxFF_{SiO}^{GSI} are presented in the Results and Discussion section of this chapter.

4.3 Retraining ReaxFF reactive force field

As mentioned in the previous section, ReaxFF_{SiO}¹¹³ was developed to describe the structures, properties, and chemistry of silicon and silicon oxide materials. However, it was not parameterized against quantum chemical data specific to gas surface interactions. First, the DFT based binding energy curves were compared to the energy values predicted by ReaxFF_{SiO}. While the energies predicted by the

ReaxFF_{SiO} potential for the non-defective T8-B1 cluster was satisfactory (Fig 34), ReaxFF_{SiO} energies were too repulsive for the T2-B1+O and T5-S1+O clusters (Figs. 32,33). Amongst defective clusters, the performance of ReaxFF_{SiO} was satisfactory for the T4-O, T4-O₂||+O, T4-O+O₂|| clusters (Figs. 35, 39, and 40 respectively). ReaxFF_{SiO} predicted a purely repulsive energy profile for the T4-O+O and T4-O₂⊥ clusters (Figs. 36 and 38), while the DFT profile showed an attractive well between 1.1 – 3.0 Å for the T4-O+O cluster and an attractive well between 1.5 – 2.0 Å for the T4-O₂⊥ cluster. ReaxFF_{SiO} predicted a qualitatively incorrect profile (no barrier for the approach of the oxygen molecule) for the T4-O₂|| cluster (Fig. 37).

To re-parameterize ReaxFF_{SiO}, the DFT based binding energy curves obtained for the defective and non – defective clusters were added to the ReaxFF_{SiO} training set to extend ReaxFF_{SiO} for gas – surface interactions. In addition to these entries, the training set contained cell parameters for quartz, cristobalite and coesite, Si, O and H charges in various compounds, Si – O bond lengths and Si – O – Si angles in crystalline forms of silica, heats of formation of quartz, cristobalite, and coesite, equation of state for silicon diamond lattice, cristobalite, and coesite, energies of silicon suboxides and ring conformations, various angle bending energies such as Si – O – Si angle, H – Si – H angle etc., Si – O and O – O bond dissociation energies, and Si and O over- and under-coordination energies, as described in van Duin et al¹¹³.

The ReaxFF parameter optimization proceeds via a successive one-parameter search optimization technique¹²⁶. This technique uses a training set that contains the DFT values for various quantities like the cell parameters, bond lengths, bond angles, torsion angles, charges, heats of formation, equations of state for various crystals, and the relative potential energies for various clusters and their associated weights. In addition, a ‘params’ file containing the list of parameters that must be optimized, which includes parameter minimums, maximums, and search interval values, is specified as an input for the force field optimization program. For every parameter specified in the params file, the program performs four individual ReaxFF runs resulting in four error values (called $Error^{ReaxFF}$). In the first two runs, the

parameter value is decreased and increased by the search interval value specified for that parameter. Using each of these parameter values, a ReaxFF-based error value is calculated for every datum in the training set. This error is defined as

$$err_i = \left(\frac{V_i^{ReaxFF} - V_i^{QC}}{\Delta_i} \right)^2$$

In the above expression V_i^{ReaxFF} is the value of the i^{th} quantity in the training set based on ReaxFF, and V_i^{QC} is the Quantum Chemical value of that quantity. The inverse weight Δ_i is a number that determines the accuracy desired for that physical quantity. The cumulative ReaxFF error for all the entries in the training set based on the present value of a parameter is defined as

$$Error^{ReaxFF} = \sum_i err_i$$

The force field optimization program calculates $Error^{ReaxFF}$ using the original (unmodified) value of the present parameter plus two modified values. A parabola ($y = ax^2 + bx + c$) is then fit through the three $Error^{ReaxFF}$ values as a function of their corresponding parameter values. If the program identifies a ‘concave up’ ($a > 0$) parabola, the procedure uses extrapolation (or interpolation) to find the optimum parameter value within a user-input set range. On the other hand, if the program identifies a ‘concave down’ ($a < 0$) parabola, the procedure chooses the best of the three parameter values. Using the best parameter value thus identified, a fourth ReaxFF run is performed after which the procedure moves on to the next parameter defined in the ‘params’ file. In order to take into account the strong inter-parameter correlation in ReaxFF, multiple copies of the list of parameters to be optimized are placed in the ‘params’ file so that the force field optimization program can visit any parameter more than once and optimize it while the other parameters take on their most recent values.

The ‘params’ file for the optimization of the ReaxFF_{SiO} potential to describe gas–surface interactions included Si and O atom parameters, Si – O and O – O bond parameters, Si – O – Si, O – Si –

O, O – O – Si and Si – Si – O angle parameters. A detailed description of these parameters and the ReaxFF_{SiO} potential energy equations can be found elsewhere¹¹³. The inverse weights for various clusters in the training set were assigned carefully to ensure that the parameter optimization is able to generate a force field that can describe the energetics of the above clusters without causing much change in the description of other structures from the earlier ReaxFF_{SiO} training set. Being a classical potential, ReaxFF does not use electronic degrees of freedom; for this reason, the ReaxFF potentials are always parameterized to reproduce the energy of the lowest-lying spin state of any configuration. Accordingly, for each of the above clusters, the energy of lowest lying spin state (triplet/singlet for non-defective clusters and doublet/quartet for defective clusters) was taken as the DFT value against which the ReaxFF_{SiO} parameters were optimized.

4.4 Results and Discussions

DFT based binding energy curves of representative systems were used to extend ReaxFF_{SiO} to describe oxygen – silica gas surface interactions. The binding energy curves from DFT, ReaxFF_{SiO} and ReaxFF_{SiO}^{GSI} for the non-defective clusters are shown in figures 32-34 while those for the defective clusters are shown in figures 35-40.

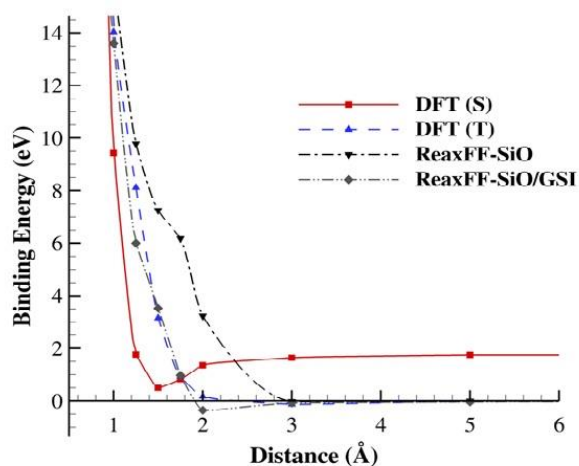


Figure 32: Binding energy curves for T2B1-O

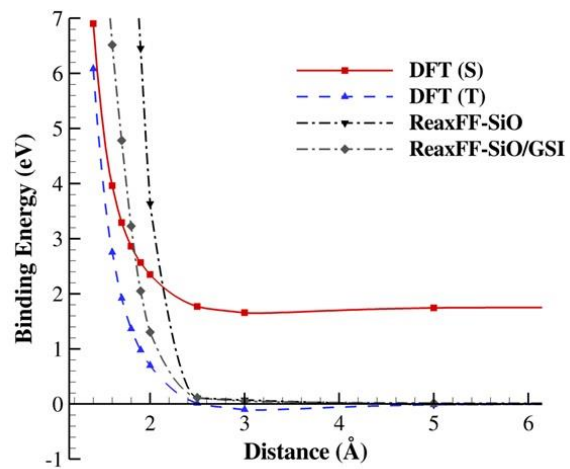


Figure 33: Binding energy curves for T5S1-O

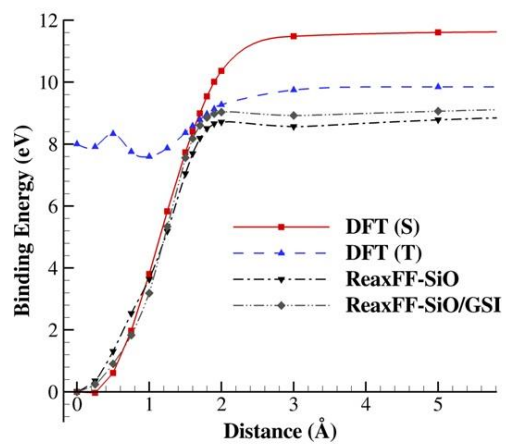


Figure 34: Binding energy curves for T8B1

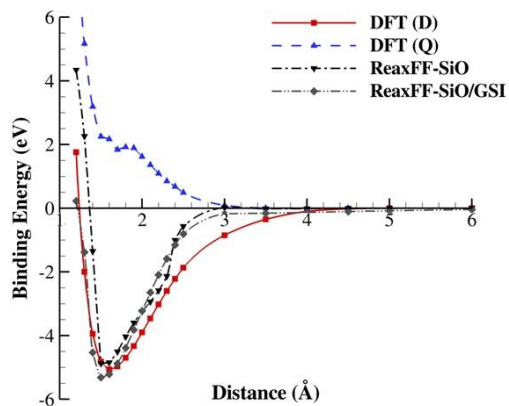


Figure 35: Binding energy curves for T4-O

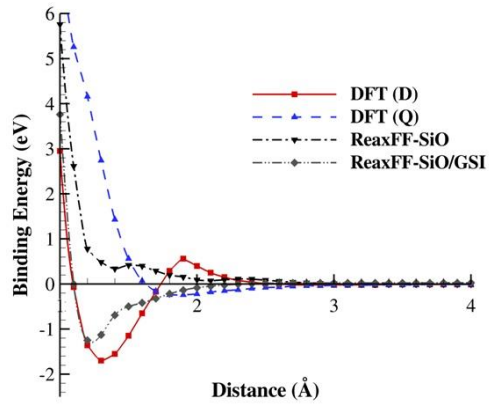


Figure 36: Binding energy curves for T4-O+O

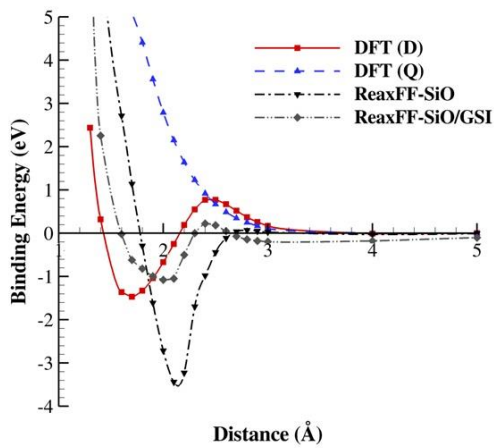


Figure 37: Binding energy curves for T4-O₂||

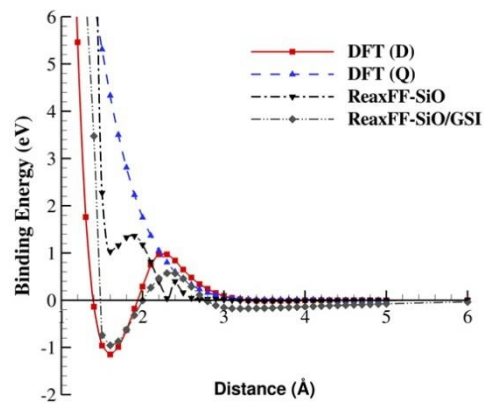


Figure 38: Binding energy curves for T4-O₂⊥

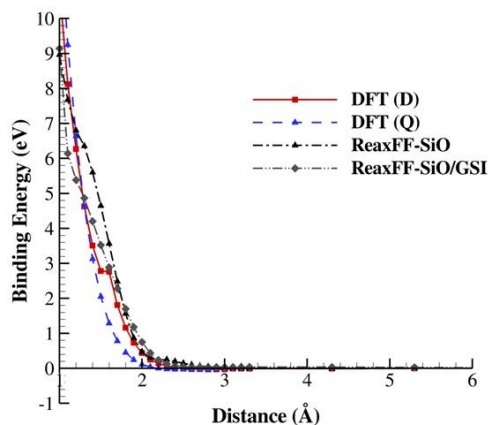


Figure 39: Binding energy curves for T4-O₂||+O

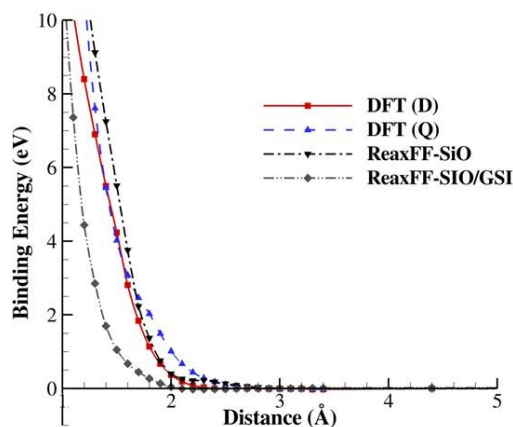


Figure 40: Binding energy curves for T4-O+O₂||

It is evident from the plots that ReaxFF_{SiO}^{GSI} is in much better agreement with the DFT values than ReaxFF_{SiO}. Notably, amongst the defective structures, ReaxFF_{SiO}^{GSI} is able to predict the correct energy profile for T4-O+O (Fig. 36), T4-O₂|| (Fig. 37), T4-O₂⊥ (Fig. 38). Among the non-defective clusters, the energy profile predicted by ReaxFF_{SiO}^{GSI} for the T2-B1+O (Fig. 32) and T5-S1+O (Fig. 33) clusters is much less repulsive than the energy predicted by ReaxFF_{SiO}. ReaxFF_{SiO}^{GSI} predicts a small attractive well between 1.9 Å and 3 Å for the T2-B1+O cluster. Though ReaxFF_{SiO}^{GSI} is in very good agreement with DFT, there are a few minor instances where ReaxFF_{SiO}^{GSI} is still unable to fully predict the DFT energy values. For instance, ReaxFF_{SiO}^{GSI} is unable to exactly reproduce the barrier for the approach of O₂ molecule in the T4-O₂|| cluster (see Fig. 37). In addition, ReaxFF_{SiO}^{GSI} predicts the minimum energy to occur at a distance of

2.0 Å for the T4-O₂|| cluster while DFT predicts the minimum energy to occur at a distance of 1.7 Å.

Though the energy profiles for the T4-O+O cluster has been improved considerably from that predicted by ReaxFF_{SiO}, the potential well, as predicted by ReaxFF_{SiO}^{GSI}, is still shallow in comparison to the DFT values (see Fig. 36).

4.5 Summary

In summary, ReaxFF_{SiO} has been extended to describe oxygen silica gas surface interactions by obtaining DFT based binding energy curves for cluster models representing defective and non-defective sites on silica surfaces and re-parameterizing ReaxFF_{SiO} to reproduce these energies. The new potential developed has been named ReaxFF_{SiO}^{GSI}. This potential can be used for accurate fully reactive molecular dynamics simulations of oxygen silica gas surface interactions. In a recent article¹²⁷, ReaxFF_{SiO}^{GSI} was used to describe the nature of chemical defects found on the surface of silica upon exposure to atomic oxygen and its implications for the catalytic recombination of the oxygen on silica surfaces.

6

Thermal Fragmentation of a Large Fullerene

6.1 Introduction

(Parts of this chapter have been submitted for review in J Phys Chem A¹²⁸)

Rocket nozzles and the surface of a spacecraft during atmospheric reentry are subjected to a tremendous heating load. Owing to their light weight and desirable chemical and mechanical properties, carbon based materials like organic thin films, polymers and carbon fiber reinforced composites are commonly used as ablatives and heat shield in spacecraft applications. The extreme heating of the surface of the spacecraft and nozzles results in material loss through pyrolysis. In order to predict the rate of mass loss from such materials, a full chemical understanding of the thermal decomposition of such materials is essential. Fullerenes are cage like structures consisting entirely of carbon atoms that could serve as a prototypical all carbon material for studying their thermal stability. Ever since their discovery¹²⁹, fullerenes have been a subject of active research owing to their wide ranging applications. A number of studies in the past have been dedicated towards attempting to explain the atomistically detailed mechanism of the formation of fullerenes from hot carbon vapor or hydrocarbon combustion flames. The earliest mechanism proposed for the formation of fullerenes was the ‘party line mechanism’¹³⁰ according to which small carbon fragments assembled into monocyclic rings. As these rings grew beyond 25 to 35 carbon atoms in size, polycyclic networks began to emerge from them which eventually rearranged into pentagons and hexagons to provide the necessary curvature for the closure of the fullerene cage. As an extension of the party line mechanism, the ‘pentagon road mechanism’¹³¹ was proposed which suggested that the lowest energy open graphitic networks formed from the party line mechanism were those that obeyed the pentagon rule and subsequently annealed into fullerenes. The ‘ring fusion spiral zipper mechanism’¹³² suggested that small carbon fragments first assemble to form planar mono, bi and tri cyclic rings that later coalesce and anneal into fullerene cages. On similar lines to the pentagon road mechanism, the ‘fullerene road mechanism’¹³³ was proposed which allowed for the existence of adjacent pentagons in

the process leading to the formation of fullerenes. *Ab initio* calculations¹³⁴ showed that such closed shell molecules with adjacent pentagons (such as C₅₀ with D_{5h} symmetry) were thermodynamically favorable. More recently, in a series of articles¹³⁵⁻¹⁴⁰, Irlé and coworkers proposed the ‘shrinking hot giant road’ to fullerene formation through their Density Functional Tight Binding (DFTB)^{81, 141} based Molecular Dynamics (MD) simulations. According to this mechanism, larger fullerene molecules (larger than 100 atoms) first assemble from hot carbon vapor through autocatalytic reactions of carbon chains. These larger fullerenes then shrink in size to C₆₀ and C₇₀ through the loss of small molecular fragments such as C₂.

In parallel with fullerene formation studies, a number of works in the past have tried to address the thermodynamics, kinetics and possible mechanisms of the decomposition of fullerenes, with most of these works being limited to small fullerenes (smaller C₁₀₀). Early laser induced fullerene decompositions experiments^{131, 142} suggested the ‘shrink – wrap mechanism’¹³¹ of fullerene fragmentation wherein the fullerene molecules shrink down in size due to the loss of a C₂ fragment from two abutting pentagons. At high temperature conditions characteristic of fullerene formation, these abutting pentagons could be formed by Stone – Wales (SW) rearrangements¹⁴³ in the fullerene molecule. Alternately, *ab initio* calculations¹⁴⁴⁻¹⁴⁵ suggested an energetically more favorable ‘handle and stick mechanism’ through an *sp*³ intermediate that does not require the creation of abutting pentagons for the loss of a C₂ unit from the fullerene molecule. MD studies based on tight binding potentials were used to understand the dynamics of fullerenes subjected to high temperatures. Wang et al¹⁴⁶ found that Buckminsterfullerene (C₆₀) was stable against spontaneous disintegration up to 5000K beyond which the cage like structure opened up into an amorphous phase due to C – C bond breakage. Zhang et al¹⁴⁷ studied the fragmentation temperature of a range of fullerenes from C₂₀ to C₉₀ and noted that the fragmentation temperature increases linearly with the size of the fullerene from C₂₀ to C₅₈ but levels off at around 4750K beyond C₆₀ while Kim et al¹⁴⁸ found that the melting temperature of C₆₀ and C₇₀ molecules lie between 3000 and 4000K. Further, at 5000K, they observed the rapid disintegration of the cage like structure in both C₆₀ and C₇₀ molecules,

initiated by the breakage of a C – C bond between a five and a six membered ring in the molecule. This was later confirmed by Kim and Tomanek¹⁴⁹, who studied the phase transitions in fullerenes with increase in temperature. In their constant energy MD simulations of a C₆₀ molecule, Xu et al¹⁵⁰ observed a continuous loss of C₂ molecules beyond a temperature of 5600K. Openov et al¹⁵¹ studied the fragmentation of a C₆₀ molecule between 4000K and 6000K, and reported an activation energy of 9.2eV for the fragmentation of the fullerene molecule. In their size down trajectories¹⁵² of the shrinking hot giant road to fullerene formation, Irle and coworkers observed that the decomposition of the self – assembled giant fullerenes occurred in two stages, an antenna fall off stage followed by the irreversible C_n pop out phase leading to the shrinking of the fullerene molecule. Further, they observed that, in a dynamic size down process of fullerene molecules, a number of channels for C_n fragment elimination (other than the ‘shrink – wrap’ and ‘handle and stick’ mechanism mentioned above) open up resulting in a variety of topological defects. While a number of works in the past have tried to study the decomposition of fullerenes, they have been restricted to the initial stages of fullerene decomposition on short time scales. To the best of our knowledge, no study has been undertaken to observe the complete size down of a fullerene molecule from its original cage like structure till its complete disintegration. In this work, we have studied the thermal decomposition of a large icosahedral fullerene molecule (C₁₈₀) by performing constant temperature MD simulations using the ReaxFF reactive force field. Prior to performing these simulations, we re-parameterized the ReaxFF C/H/O potential to obtain a more accurate description of the condensed phases of carbon. The newly developed potential (called ReaxFF_{C-2013}) was used in the MD studies of C₁₈₀ fragmentation between temperatures of 4100K and 4500K to obtain the decomposition rates and activation energy for the large fullerene decomposition.

6.2 Parameterizing ReaxFF_{C-2013} Reactive Force Field

As mentioned in chapter 3, ReaxFF C/H/O potential was developed by Chenoweth et al³⁷ to describe hydrocarbon and their oxidation chemistry by parameterizing against an extensive training set consisting of atomic charges, bond lengths, bond, valence and torsion angle energies, heats of formation

and various hydrocarbon reaction energies. However, this potential was not explicitly parameterized to describe the dynamics of condensed phases of carbon. Towards this end, ReaxFF C/H/O has been extended to describe carbon condensed phases more accurately. The new potential developed here is called ReaxFF_{C-2013}. In addition to the ReaxFF C/H/O training set, the training set for ReaxFF_{C-2013} parameterization consisted of equation of state type data for the volumetric expansion of diamond, in and out of plane expansion of graphite, uniaxial expansion of diamond in (001) direction, heats of formation of graphite, diamond, mono, di, tri and quadruple vacancies in graphene, heat of formation of stone-wales defect in graphene and heats of formation of a number of amorphous carbon phases obtained from earlier simulations of thermal decomposition of fullerenes performed in our group using the ReaxFF_{CHO} potential. First principles calculations based on Density Functional Theory (DFT) were performed to provide the aforementioned data for ReaxFF_{C-2013} parameterization. DFT based calculations to obtain the equation of state of graphite and diamond were performed using the Perdew – Burke – Ernzerhoff (PBE)⁴⁴ exchange-correlation functional with the DFT-D2¹⁵³ parameters to describe the van der Waals interaction for carbon as implemented in the VASP package¹⁵⁴. A projector augmented wave (PAW) potential¹⁵⁵ was used to perform the calculations. A well converged 12x12x12 Kpoint mesh was used for the two atom diamond unit cell while a denser 16x16x8 Kpoint mesh was used for the four atom graphite unit cell with a high precision setting in VASP that used a 500eV plane wave energy cutoff. While the condensed phase calculations were done using a plane wave basis set based code, the heats of formation for the amorphous carbon phases and fullerenes were calculated using the Jaguar quantum chemistry package¹⁵⁶ in the Schrodinger software suite employing the 6-311g** basis set¹⁵⁷ and B3LYP¹⁵⁸⁻¹⁶⁰ exchange correlation functional. For these calculations, the geometry optimizations were performed with a root mean squared (RMS) force convergence criteria of 3.5×10^{-4} hartree per a.u. or smaller.

The parameterization of the ReaxFF_{C-2013} potential was carried out using a successive one parameter search optimization technique¹²⁶, described in detail in chapter 5. The energy predictions from DFT-D2, ReaxFF_{CHO} and ReaxFF_{C-2013} are shown in the figures below. In all the figures, the black line

corresponds to values from DFT-D2, the blue line corresponds to values from ReaxFF C/H/O and the red line corresponds to values from ReaxFF_{C-2013}. All the energies are reported on a ‘per atom’ basis. Figures 41 and 42 below show the equation of state for graphite obtained upon expansion / compression of the lattice in the in-plane and out of plane directions respectively.

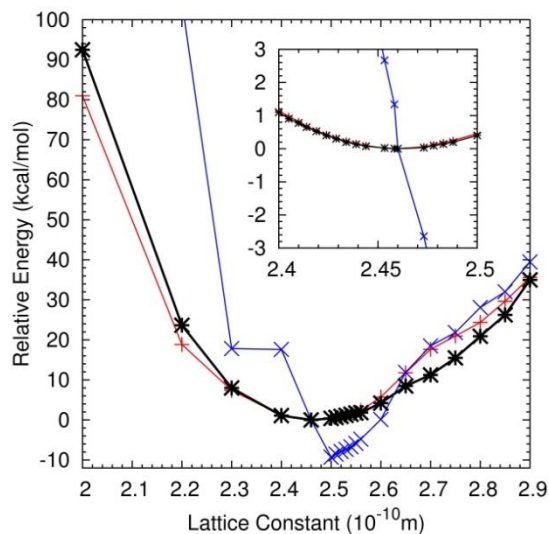


Figure 41: Equation of state data for the isotropic variation of the lattice constant along graphite basal plane directions. Black line corresponds to DFT-D2, red line corresponds to ReaxFF_{C-2013} and blue line corresponds to ReaxFF_{CHO}.

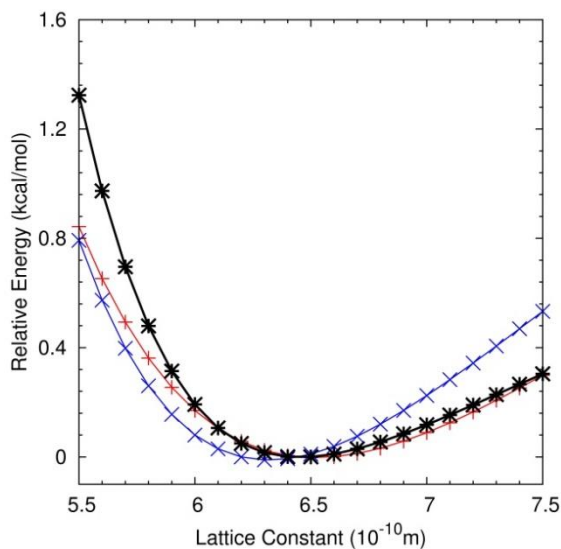


Figure 42: Equation of state data for the variation of the lattice constant normal to the graphite basal plane directions. Black line corresponds to DFT-D2, red line corresponds to ReaxFF_{C-2013} and blue line corresponds to ReaxFF_{CHO}.

From the above figures, especially from figure 41, it is clear that ReaxFF_{C-2013} is in much better agreement with DFT-D2 compared to ReaxFF C/H/O. ReaxFF C/H/O predicted incorrect values for the in and out of plane optimum lattice constants of graphite. In addition, ReaxFF C/H/O predicted an incorrect curvature in the energy vs lattice constant curve around the minimum and an artificial shoulder between 2.3 and 2.4 Å in the in-plane direction. Figures 43 and 44 show the equation of state for diamond obtained upon volumetric expansion/compression and the uniaxial expansion/compression along the (001) direction respectively. The force field optimization procedure used a 2x2x2 super cell (containing 16 atoms) of the diamond structure used in the DFT-D2 calculations.

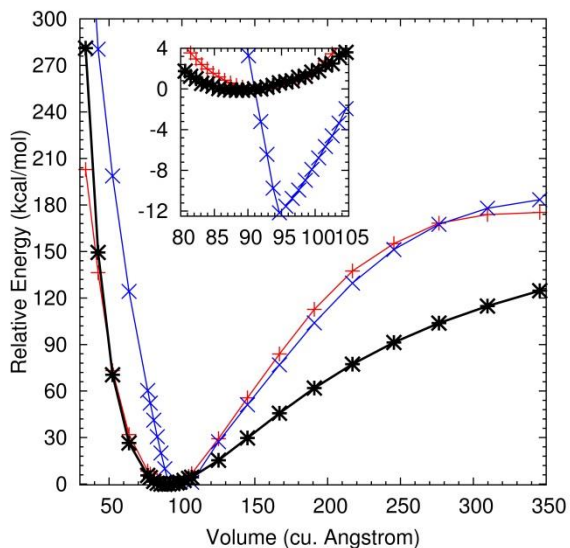


Figure 43: Equation of state data for the cubic expansion of a 2x2x2 diamond super cell containing 16 atoms. Black line corresponds to DFT-D2, red line corresponds to ReaxFF_{C-2013} and blue line corresponds to ReaxFF_{CHO}.

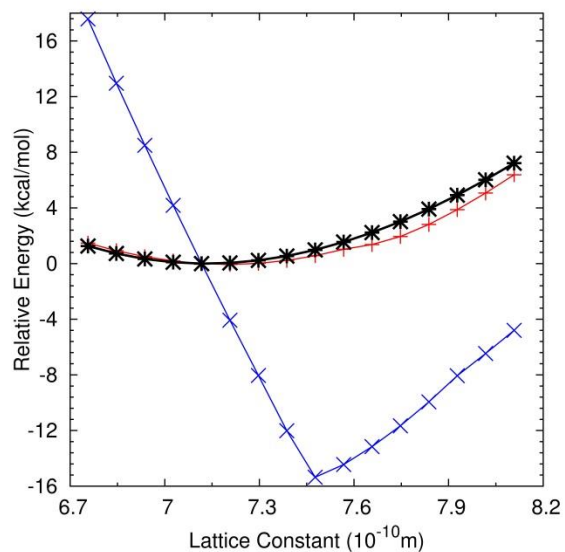


Figure 44: Equation of state data for the uniaxial expansion of a 2x2x2 diamond super cell containing 16 atoms in the (001) direction. Black line corresponds to DFT-D2, red line corresponds to ReaxFF_{C-2013} and blue line corresponds to ReaxFF_{CHO}.

Again, figures 43 and 44 show that ReaxFF_{C-2013} overcomes the inaccurate prediction of the optimal lattice constant and the curvature around the minimum by ReaxFF C/H/O, resulting in a potential that closely reproduces the DFT-D2 based equation of state for diamond. However, ReaxFF_{C-2013} predicts a much stiffer equation of state for large volumetric expansions greater than 10%. Figure 45 shows the relative energies (in kcal/mol) of various vacancy defects and Stone-Wales defect¹⁴³ (SW) on graphene with respect to pristine graphene on a ‘per atom’ basis. The energy computed using DFT-D2, ReaxFF_{CHO} and ReaxFF_{C-2013} is shown in black, blue and red fonts respectively. All the molecular images in this chapter were constructed using the VMD molecular visualization package¹⁶¹.

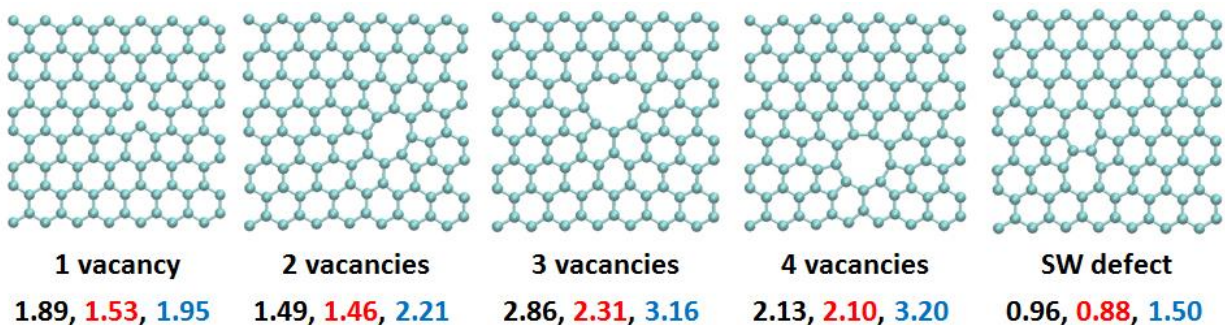


Figure 45: Relative energies (in kcal/mol) of vacancy and stone - wales defect in graphene with respect to pristine graphene expressed on a per atom basis. Black font corresponds to DFT-D2, red font corresponds to ReaxFF_{C-2013} and blue font corresponds to ReaxFF_{CHO}.

Clearly, ReaxFF_{C-2013} is in very good agreement with DFT-D2 data. ReaxFF_{C-2013} predicts an atomization energy of 172.6 kcal/mol for graphite, in very close agreement with experimental value of 172.46 kcal/mol¹⁶² while ReaxFF C/H/O predicted a graphite atomization energy of 197.3 kcal/mol. Further, on a per atom basis, ReaxFF_{C-2013} predicts graphite to be 0.66 kcal/mol more stable than diamond and graphite to diamond transformation barrier of 4.91 kcal/mol, in close agreement with the respective DFT-D2 values of 0.61 kcal/mol and 7.41 kcal/mol. Table 7 shows the formation energy of various fullerenes with respect to C₆₀ on a ‘per atom’ basis, computed using the equation below. The symmetry of each of the fullerene is listed in brackets in table 7.

$$\Delta E = \frac{E_{C_n}}{n} - \frac{E_{C_{60}}}{60}$$

	Formation energy (kcal/mol)		
	DFT	ReaxFF _{CHO}	ReaxFF _{C-2013}
C ₃₂ (D _{3h})	11.32	10.76	7.44
C ₃₆ (D _{3h})	8.72	7.62	5.84
C ₄₂ (C _{2v})	7.47	6.32	4.65
C ₄₄ (D _{3h})	6.38	5.65	4.16
C ₄₆ (C _{2v})	5.47	4.41	3.25
C ₄₈ (C _{2v})	5.78	4.71	3.30

C₅₀ (D_{3h})	8.70	5.98	4.04
C₆₀ (I_h)	0.00	0.00	0.00

Table 7: Formation energy of various fullerenes expressed on a 'per atom' basis with respect to C₆₀ molecule

Figure 46 shows the formation energy for various amorphous 'blob' like phases obtained upon thermal decomposition of a C₁₈₀ molecule using ReaxFF C/H/O with respect to fullerenes of corresponding sizes using the equation below

$$\Delta E = \frac{E_{C_n}^{blob}}{n} - \frac{E_{C_n}^{Fullerene}}{n}$$

The symmetry of the fullerene molecules considered is same as that shown in brackets in table 7. In the above equation, $E_{C_n}^{blob}$ corresponds to the single point energy of the amorphous 'blob' like phases shown in figure 46 while $E_{C_n}^{Fullerene}$ is the optimized energy value of the corresponding fullerene. The energy computed using DFT, ReaxFF_{C-2013} and ReaxFF_{CHO} is shown in black, red and blue fonts respectively.

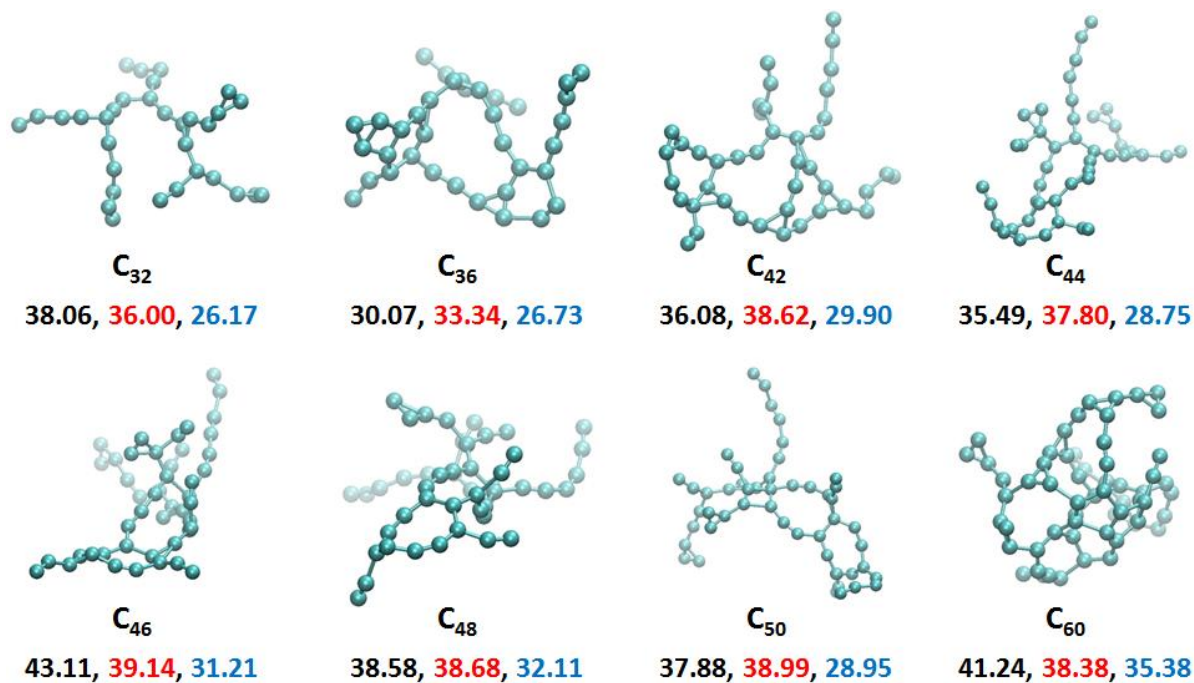


Figure 46: Relative energies (in kcal/mol) on a 'per atom' basis of amorphous phases with respect to fullerenes of corresponding sizes. Black font corresponds to DFT, red font corresponds to ReaxFF_{C-2013} and blue font corresponds to ReaxFF_{CHO}.

From table 7, we see that ReaxFF_{C-2013} predicts smaller fullerenes (smaller than C₆₀) to be more stable than ReaxFF C/H/O. However, this overestimation does not have any effect on our simulations as the molecule opens up into an amorphous phase by the time it decays down to C₆₀, as discussed in the following sections. Figure 46 clearly shows that ReaxFF_{C-2013} is in very good agreement with DFT energies for such amorphous phases. In addition, ReaxFF_{C-2013} is able to reproduce the faceted geometry of larger fullerenes such as C₂₄₀, C₃₂₀, C₅₄₀ etc. as predicted by earlier DFT calculations¹⁶³. Finally, ReaxFF_{C-2013} predicts a barrier of 6.9eV for the SW transformation of a C₆₀ molecule of I_h symmetry into a C₆₀ molecule of C_{2v} symmetry through the concerted rotation of a C₂ unit (the transition state has C₂ symmetry), in excellent agreement with earlier published DFT data¹⁶⁴. Thus a new ReaxFF potential, ReaxFF_{C-2013}, has been created which can accurately describe carbon condensed phases. This newly developed potential has been used to study the thermal fragmentation of a C₁₈₀ molecule, discussed in detail in the following sections.

6.3 Simulation Methods and Details

To study the thermal decomposition dynamics of a large fullerene, molecular dynamics (MD) simulations were performed on a C₁₈₀ molecule using the newly developed ReaxFF_{C-2013} potential. Prior to the MD simulations, the molecule was energy minimized with a Root Mean Square (RMS) force convergence criteria of 0.1 kcal/mol-Å. The molecular dynamics simulations were performed in canonical ensemble (NVT ensemble) at five different temperatures, between 4100K and 4500K, at intervals of 100K. All the MD simulations used the Berendsen thermostat⁴⁶ with a damping constant of 100fs to maintain the system temperature at the desired value while the equations of motion were integrated using the velocity – verlet algorithm. Following energy minimization, the molecule was first equilibrated at 300K before rising the temperature up to the desired value. The equilibration simulation was carried out in the canonical (NVT) ensemble for a duration of 60 ps using a time step of 0.25fs. The potential energy and temperature values indicated that the system had well equilibrated by 15 ps. Thus, post equilibration, temperature ramping simulations were initiated from 300K to the desired final temperature using atomic

positions, velocities and accelerations from the equilibration simulation, harvested at 5ps intervals beginning at 15ps till 60 ps, giving a total of 10 independent trajectories for every target temperature (i.e., a total of 50 trajectories). For each of these trajectories, the temperature was increased linearly from 300K to the desired final value at the rate of 0.005 K per iteration, using at time step of 0.1 fs. After the temperature ramp, production runs were carried out at the target temperature (4100K to 4500K in intervals of 1000K) in canonical ensemble using a time step of 0.1fs, on each of the 10 independent trajectories. The production runs lasted from anywhere between 0.25 ns and 5.4 ns depending on the temperature, with lower temperature simulations lasting for a longer duration of time. It is now well known from earlier DFTB based MD simulations¹⁶⁵ and our own simulations using the ReaxFF C/H/O potential that large fullerenes can both loose and gain small C_n fragments when subjected to high temperature annealing at constant density. Since the goal was to study the monotonic decay process of a large fullerene, in our production runs, any small molecule (defined as a molecule with mass less than 100 a.m.u. or smaller than C₉) formed due to the fragmentation of the fullerene was removed from the system. In effect, an open system was simulated that can exchange both mass and energy with the surroundings. A detailed discussion of the results from these simulations is presented in the following section.

6.4 Results and Discussion

In this section, the results obtained from the molecular dynamics simulation of the thermal fragmentation of a C₁₈₀ molecule using the newly developed ReaxFF_{C-2013} potential are discussed. The simulations began with a fullerene of 'Ih' symmetry consisting of 12 five membered rings and 80 six membered rings. Temperature ramp from 300K caused SW rearrangements in a few trajectories resulting in a different number of 5-memebered, 6-membered, 7-membered and 8-membered rings at the end of this stage. Of the 10 trajectories leading to 4100K target temperature, none of them underwent any SW rearrangements. For 4200 K target temperature, one trajectory underwent SW rearrangement resulting in a fullerene with 13 5-membered, 78 6-membered and 1 7-membered rings. Two trajectories underwent SW rearrangements leading to 13 5-memeberd, 78 6-membered and 1 7-membered rings for 4300K target

temperature, three trajectories ended up with 13 5-membered, 78 6-membered and 1 7-membered rings, and one trajectory ended up with 12 5-membered, 76 6-membered, 2 7-membered and 1 8-membered rings at 4400K target temperature. For 4500K target temperature, three trajectories ended up with 13 5-membered, 78 6-membered and 1 7-membered rings, and one trajectory ended up with 14 5-membered, 76 6-membered and 2 7-membered rings. Subsequent molecular dynamics simulations in canonical ensemble at these target temperatures resulted in the decomposition of the C_{180} fullerene into smaller fullerenes with many topological defects through loss of small fragments such as C_2 , C_3 units etc. and later into an amorphous phase. Figures 47a to 47e show the size of the fullerene (N) as a function of time obtained from the ten independent trajectories at each target temperature, expressed as the ratio (called 'lost mass ratio' henceforth) of the number of atoms lost to the initial number of atoms in the fullerene ($1 - N/N_0$, $N_0 = 180$).

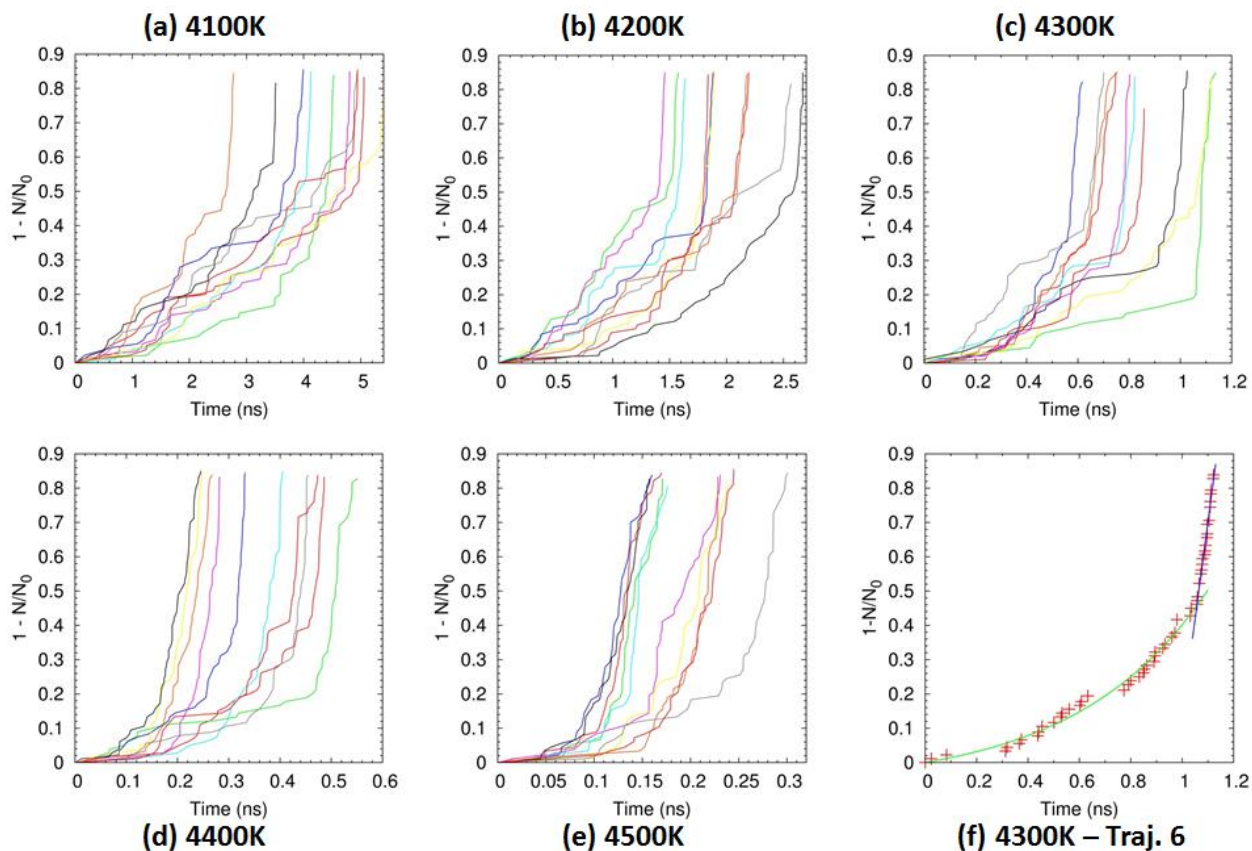


Figure 47: (a)-(e) Decay of a C_{180} fullerene as a function of time from the 10 independent trajectories at each target temperature. (f) Curve fit to the exponential and linear regime of the decay process at 4300K.

From figure 47, it can be seen that, with increase in temperature, the decomposition of the fullerene occurs faster with the time required for decay reducing by an order of magnitude as the temperature increases from 4100K to 4500K. Further, at any given temperature, the decomposition times could vary widely indicative of the inherently stochastic nature of the decomposition process. While the decay times vary between trajectories at any given temperature, each trajectory can be understood by dividing it into an initial exponential decay period for the lost mass ratio followed by a final linear decay regime, as shown in figure 47f for a trajectory at 4300K. Figure 48 shows the sequence of states through which a C_{180} molecule proceeds upon fragmentation from one of the trajectories at 4100K, which can be used in the phenomenological understanding of the exponential and linear regimes suggested above.

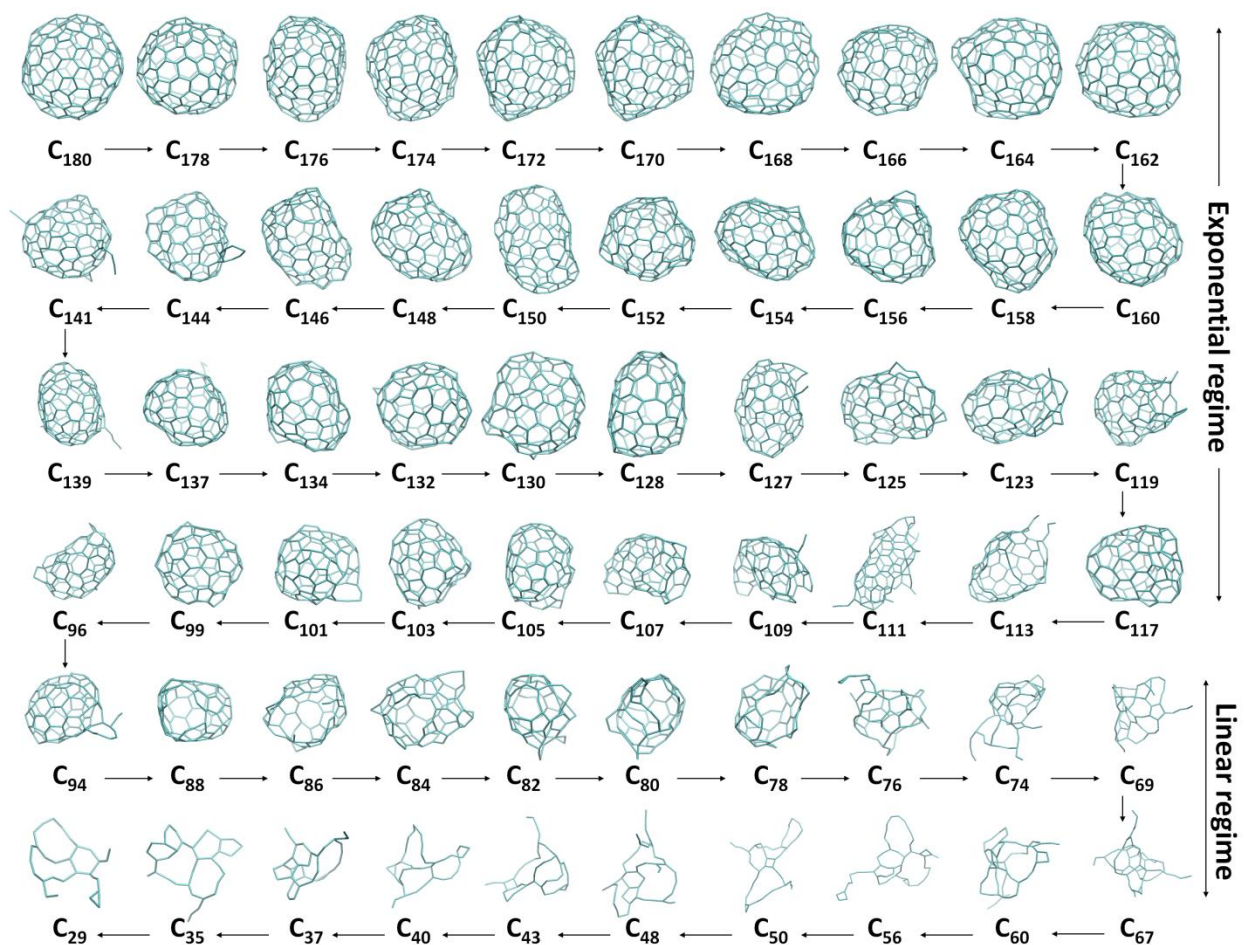


Figure 48: A sequence of states through which a C_{180} molecule proceeds upon thermal fragmentation at 4100K

In the initial exponential regime, the fullerene molecule shrinks in size primarily through the loss of small fragments such as C_2 , C_3 and C_4 units, akin to the ‘ C_n pop out’ events described by Irle and co-workers¹⁵² in their DFTB/MD simulations of the shrinking hot giant road to fullerene formation. During this period, while the fullerene molecule shrinks in size, it retains the cage like structure. Temporary cage opening may occur due to the formation of a large defect such as the C_{113} molecule in figure 32, but the molecule anneals into a cage like structure eventually (e.g., the molecule has annealed back into a cage like structure by C_{103} state). Eventually, the molecule shrinks to a small enough size that once the cage opening process sets in, the molecule is unable to anneal itself back into a closed shell like structure. In figure 48, this event begins when the molecule has decayed to C_{94} . Beyond C_{94} , as the cage begins to unravel, the molecule is unable to regain the closed shell like structure, with the cage opening process

complete by the time the molecule reduces in size to C_{74} . In this regime, the molecule could lose larger fragments such as C_5 , C_6 and C_7 molecules during the process of shrinking. The loss of these large fragments is akin the ‘antenna fall off’ event described earlier by Irlle and co-workers¹⁵², albeit happening from an amorphous carbon cluster instead of a chain of carbon atoms attached to the fullerene cage. In this regime, there is acceleration in the rate of mass loss, with the lost mass ratio becoming a linear function of time. Such opening of the cage is an entropically driven event, observed both in earlier molecular dynamics studies^{146, 149, 166} and experiments¹⁶⁷. The beginning of the cage unravelling feature of the fullerene shrinking process is dependent on temperature, with a larger temperature resulting in the onset of this process at an earlier point in time (or at a larger fullerene size). In our simulations, on an average (average over the 10 trajectories at each target temperature), the cage opening process begins when the fullerene has shrunk to C_{83} , C_{99} , C_{113} , C_{124} and C_{142} at 4100K, 4200K, 4300K, 4400K and 4500K respectively. In order to obtain the activation energy for the larger fullerene decay process, for each of the 50 trajectories, an equation of the form $\left(1 - \frac{N}{N_0}\right) = c_1(e^{k_1 t} - 1)$ was fit to the exponential portion of the decay curve and another equation of the form $\left(1 - \frac{N}{N_0}\right) = k_2 t + c_2$ was fit to the linear portion of the decay curve. One such fit to both the exponential and linear decay portion of a trajectory at 4300K was shown in figure 47f. An average over the ten values for k_1 and k_2 at each temperature was taken as the rate of mass loss in the exponential and linear regimes respectively. Table 8 below gives a compilation of the rates obtained for all the trajectories along with their average values.

	Regime	#1 (ns ⁻¹)	#2 (ns ⁻¹)	#3 (ns ⁻¹)	#4 (ns ⁻¹)	#5 (ns ⁻¹)	#6 (ns ⁻¹)	#7 (ns ⁻¹)	#8 (ns ⁻¹)	#9 (ns ⁻¹)	#10 (ns ⁻¹)	Average (ns ⁻¹)
4100K	Exponential	0.0658	0.8403	0.1370	0.3059	0.5725	0.2925	0.4539	0.4412	0.0979	0.2687	0.3476
	Linear	2.8080	2.5980	1.6020	3.1910	3.6520	2.2640	4.9630	2.7930	2.4070	2.4040	2.8682
4200K	Exponential	1.2580	0.5685	0.3278	0.8651	0.6465	1.5230	1.1650	0.6065	0.6065	1.1620	0.8729
	Linear	2.3990	7.0840	5.5690	6.9500	4.5900	2.2880	5.1840	3.1090	3.1090	6.9250	4.7207
4300K	Exponential	3.9400	0.4177	6.1510	3.0700	2.3910	1.9550	0.1518	4.8650	0.5642	2.5350	2.6041
	Linear	5.2470	9.2650	8.7870	14.1400	6.6740	5.6560	7.7120	3.8050	6.0650	9.0010	7.6352
4400K	Exponential	5.6620	1.3770	8.1720	27.4800	12.7300	22.8100	11.5300	22.1900	7.7080	7.3550	12.7014
	Linear	16.1100	9.2080	24.0900	11.5600	10.7600	9.6390	8.46400	10.8400	16.2600	6.9790	12.3910
4500K	Exponential	44.6800	33.1900	33.7100	8.2960	26.2300	20.9800	30.6000	25.3200	8.20500	26.710	25.7921
	Linear	9.2810	11.9100	11.8700	7.3660	14.6600	10.0600	13.7400	17.8500	13.0500	12.720	12.2507

Table 8: Rate of mass loss from the C₁₈₀ fullerene at various temperatures in both the exponential and linear regimes of decay

An Arrhenius type equation ($k = Ae^{-E_a/RT}$) was then fit to the average values of k_1 and k_2 in the table above, giving an activation energy of 17.9 eV for the exponential regime and 6.2 eV for the linear regime. Comparing this with the activation energy for C_{60} fragmentation reported earlier (~ 9.2 eV)¹⁵¹, we find that the fragmentation of C_{180} requires the a much larger energy to overcome the barrier. This is primarily due to the increase in the heat of formation of a fullerene with its size, as obtained from both our calculations and confirmed by earlier experiments¹⁶⁸ and theoretical work¹⁶⁹. The fragmentation energy of C_2 from a C_{180} molecule, defined as the energy of the reaction $C_{180} \rightarrow C_{178} + C_2$, computed here as the reaction energy obtained upon geometry optimization of the C_{178} and C_{180} molecules (using an RMS force convergence criteria of 0.1 Kcal/Å) from our trajectories at 4100K, 4200K and 4300K was found to be 14.132 eV. Comparing this value with the earlier published values for C_2 fragmentation energy from C_{60} (11 – 12 eV)¹⁷⁰⁻¹⁷¹, C_{70} (10.7 – 13.3 eV)¹⁷²⁻¹⁷³, C_{80} (8.7 – 10 eV)¹⁷⁴⁻¹⁷⁵, C_{82} (9.1 – 9.4 eV)¹⁷⁵⁻¹⁷⁶, we see that C_{180} fullerene has a larger C_2 fragmentation energy compared to the smaller fullerenes. This result is in agreement with other experimental and theoretical results that show an increase in the C_2 fragmentation energy with the size of the fullerene¹⁷⁷⁻¹⁷⁸. Finally, figure 49 shows the probability that a molecule of size C_x loses a fragment of size C_n to form a molecule of size C_{x-n} during the decay process of the C_{180} fullerene at each target temperature, obtained as an average over the ten trajectories at that temperature.

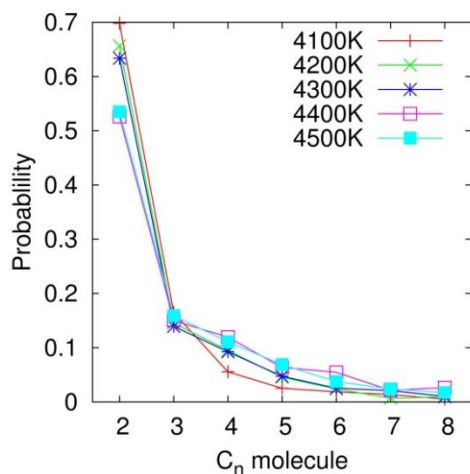


Figure 49: The average probability for the shrinking of the C_{180} fullerene through the loss of a C_n molecule at temperatures between 4100K and 4500K

From figure 49 it can be seen that at all temperatures, the fragmentation of the fullerene proceeds predominantly via the loss of C_2 units, with much smaller probabilities for the loss of C_3 and larger fragments. With increase in temperature however, the probability of loss of larger fragments increases due to entropic effects with a consequent decrease in the probability of decay through loss of C_2 units.

6.5 Summary

In summary, the thermal fragmentation of a large fullerene (C_{180}) has been simulated through molecular dynamics simulations using the ReaxFF reactive force field. Prior to performing these simulations, the ReaxFF C/H/O potential was reparameterized against DFT data for equations of state of graphite and diamond, formation energies of various defects in graphene, small fullerene molecules and various amorphous carbon phases, yielding a new potential ReaxFF_{C-2013} that can accurately describe the condensed phases of carbon. ReaxFF_{C-2013} was then used to study the kinetics of a large fullerene fragmentation by performing molecular dynamics at temperatures between 4100K and 4500K, in the intervals of 1000K, for a duration of time between 0.25 and 5.4 ns. At each of the temperature, ten independent trajectories were simulated resulting in a range of fragmentation times and fragmentation products.

Fullerene fragmentation simulations indicated that between 4100K and 4500K, the fullerene shrinks in size to smaller molecules through the loss of molecular fragments such as C_2 , C_3 , C_4 etc. At all temperatures, the fragmentation of the fullerene can be divided into two distinct regimes, an initial exponential regime followed by a final linear regime. In the exponential regime of decay, the fullerene shrinks in size due to the loss of small molecular fragments such as C_2 , C_3 , and C_4 units while it retains its cage like structure. However, in the final linear regime of decay, the cage opens up into an amorphous phase and the molecule can shrink in size through the loss of larger molecular fragments such as C_5 , C_6 etc. The onset of the linear regime was found to be a temperature dependent phenomenon with the onset happening earlier at larger temperatures. The rate of decay obtained for the exponential and linear regimes for each of the ten independent trajectories at each simulation temperature was averaged to obtain the

mean rate of decay in each regime at each temperature. An Arrhenius type equation was then fit to these mean rates, giving an activation energy of 17.9 eV for the exponential regime and 6.2 eV for the linear regime. The probability distribution of fullerene fragmentation through the loss of C_n units indicated that at all temperatures, the fullerene fragmentation occurs predominantly through the loss of C_2 units. However, with increase in temperature, the probability of loss of larger fragments such as C_3 , C_4 , C_5 , C_6 , C_7 and C_8 increases. The ReaxFF_{C-2013} potential developed in this work along with the fullerene decomposition simulations are an important step towards the full computational chemical modelling of the decomposition of carbon rich materials and species in various fields such as soot decomposition, graphite rocket nozzle erosion and ablation of carbon based materials used in space crafts during atmospheric reentry.

7 Initial Validation of ReaxFF_{CHOB} Potential for Oxygen – Boron-Doped Graphene/Graphite Gas Surface Interactions

7.1 Introduction

Boron is one of the most widely used dopant in carbon materials¹⁷⁹. Boron substitution in graphite is known to improve the oxidation resistance of graphite in both wet and dry thermal O₂¹⁸⁰⁻¹⁸² due to the formation of a boron oxide layer that is impermeable to oxygen diffusion. The doping of carbon with boron has been shown to improve the capacity of carbon as an anode material in Li ion batteries¹⁸³. The improved oxidation resistance of boron doped carbon materials could serve as a guide to design materials that can withstand erosion due to hyperthermal impact of oxygen atoms at elevated temperatures for space based applications. A ReaxFF potential (ReaxFF_{CHOB}) was developed recently for modeling the chemistry and kinetics of ammonia borane oxidation¹⁸⁴⁻¹⁸⁵. This potential was extended to accurately reproduce the thermodynamics and material behavior of complex boron, boron carbide and boron nitride condensed phases. In the following section, initial stages in the development of ReaxFF_{CHOB} to describe oxygen – boron doped graphene gas surface interaction has been discussed.

7.2 Cluster models, DFT based binding energy curves and Performance of ReaxFF_{CHOB}

Cluster models representing boron doped graphene were chosen to obtain the DFT based potential energy curves for the approach of an oxygen atom. A coronene molecule was chosen to represent graphene. Coronene is the smallest molecule containing a completely aromatic 6 member ring representative of graphene and has been used in the past as a model for graphene¹⁸⁶. Three different models containing 1, 2 and 3 boron atoms corresponding to 4.2%, 8.3% and 12.5% doping were considered as shown in figure 50 below. The boron atoms were doped such that no two boron atoms are bonded in the molecule since experimental evidence suggests that at low doping levels isolated boron atoms are dominant in the material¹⁸⁷. DFT calculations were performed using M06-2X¹²³ density functional as it has been shown to perform better than the widely used B3LYP¹⁵⁸⁻¹⁶⁰ functional for main

group thermochemistry¹²³. All the calculations employed cc-PVTZ basis set of Dunning and co-workers¹⁸⁸.

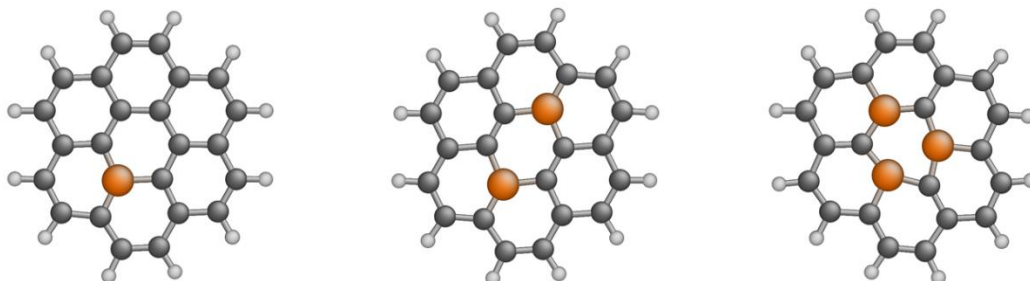


Figure 50: Models considered for oxygen - boron doped graphene gas surface interactions. Carbon atoms are colored gray, boron atoms are colored orange and hydrogen atoms are colored white.

Firstly, the binding energy for oxygen binding onto various positions of the B-doped coronene (shown in figure 51) molecule was considered. These molecules have been named models A to F. The reference was chosen to be the B-doped coronene molecule in its ground state (doublet state for the molecule containing 1 and 3 boron atoms and singlet state for the molecule with 2 boron atoms) and oxygen (in triplet ground state) at infinity. The binding energies obtained from DFT and ReaxFF_{CHOB} are reported in table 9.

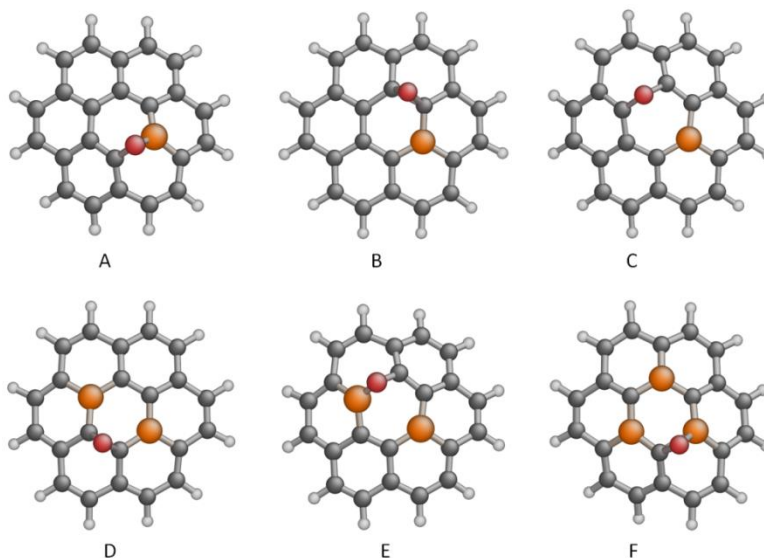


Figure 51: Oxygen binding to various positions on boron doped coronene molecule

	DFT (M06-2X/cc-PVTZ) (kcal/mol)	ReaxFF_{CHOB} (kcal/mol)
A	-138.13	-117.05
B	-99.19	-51.24
C	-111.56	-28.72
D	-166.92	-69.05
E	-194.06	-112.57
F	-192.03	-191.71

Table 9: Binding energy of oxygen atom in models A - F

From table 9, it is clear that ReaxFF_{CHOB} is in good agreement for models A and F while it needs to be improved for models B to E. Next, the single point energies as a function of distance was calculated for the approach of a second oxygen atom to models A – F using DFT to obtain the potential energy curve. Models A, B, C and F contain odd number of electrons. Thus doublet and quartet curves were calculated for these models. Models D and E contains even number of electrons and hence singlet and triplet curves were calculated for these models. The same calculation was also performed with ReaxFF_{CHOB} to obtain a comparison between the two methods. There are 5 different positions possible for the approach of the second oxygen atom to models A, B, C, E and F. These are named A1-A5, B1-B5, C1-C5, E1-E5 and F1-F5. Three different positions are possible for the approach of a second oxygen atom to model D, named D1-D3. The potential energy curves along with the images of the models for A – F are shown in figures 52 – 57 respectively.

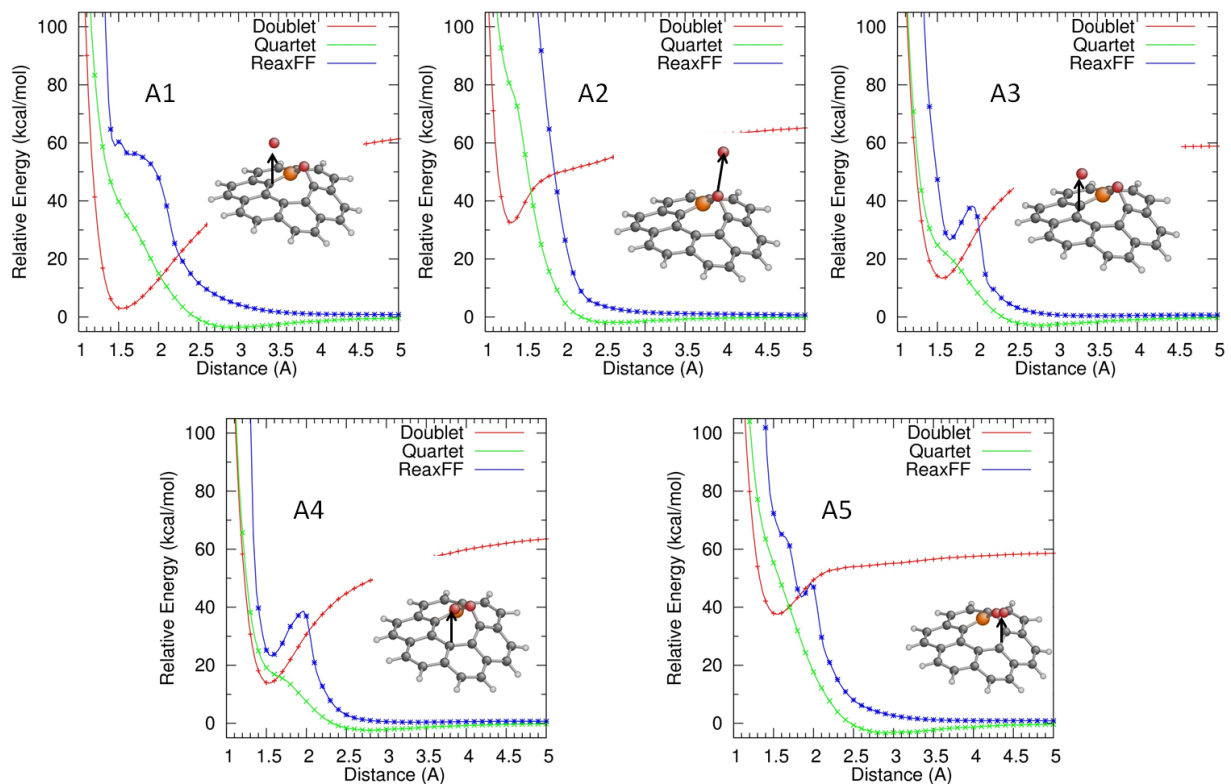


Figure 52: Binding energy curve for model A

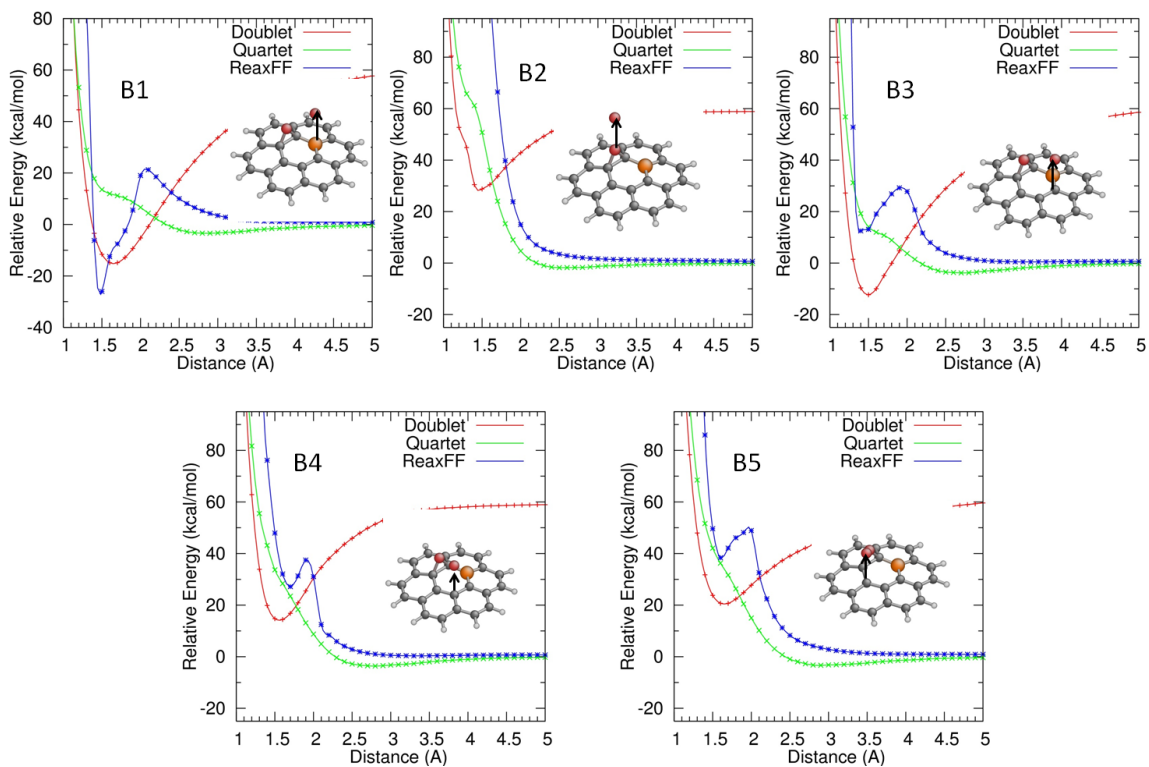


Figure 53: Binding energy curve for model B

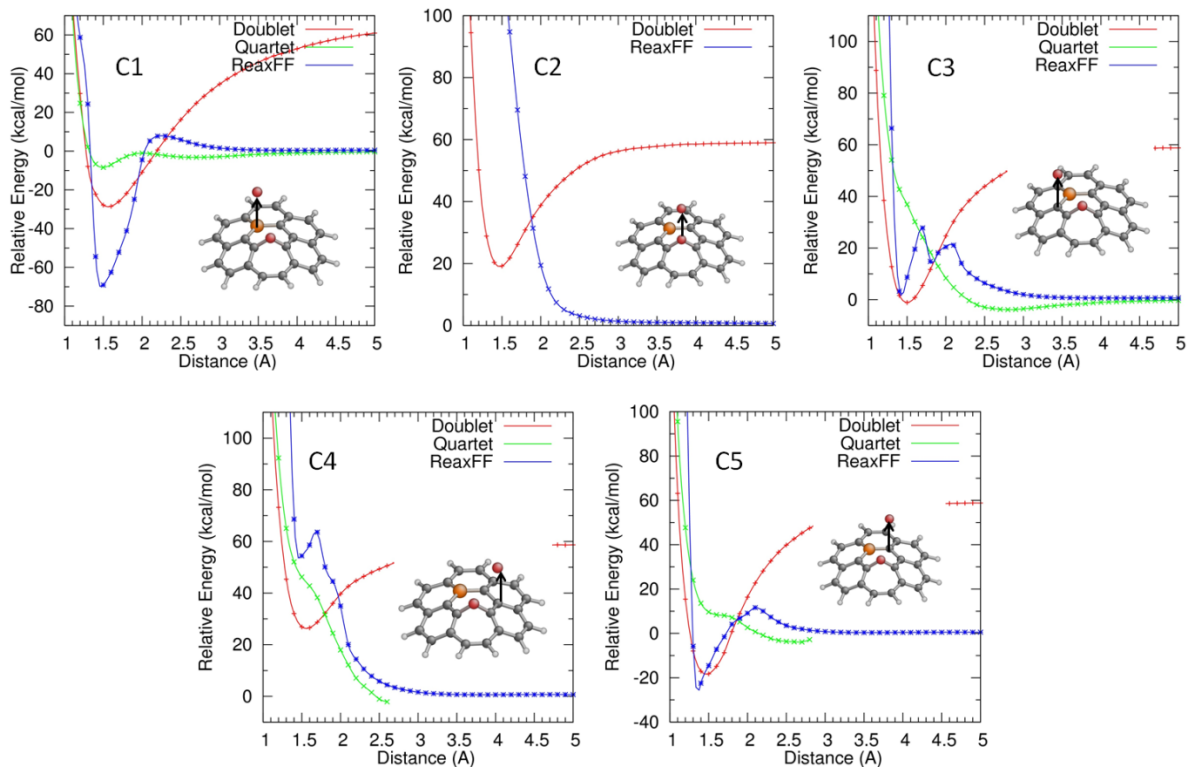


Figure 54: Binding energy curves for model C

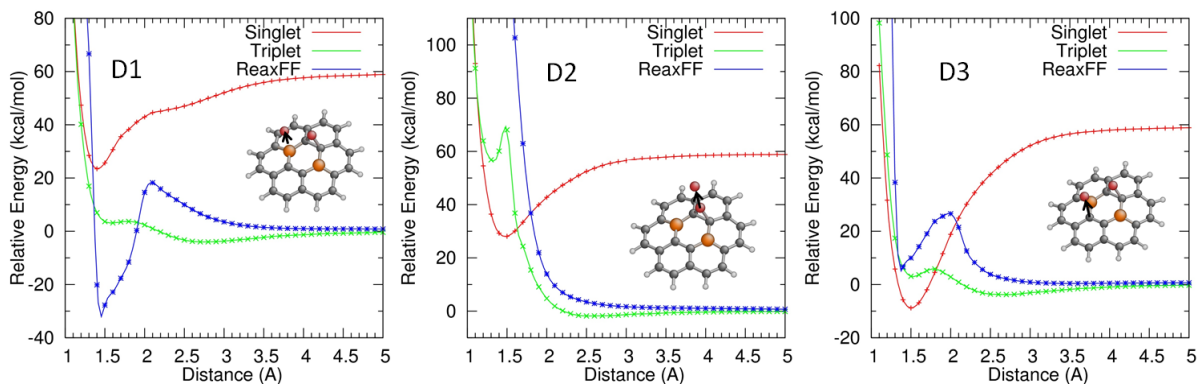


Figure 55: Binding energy curves for model D

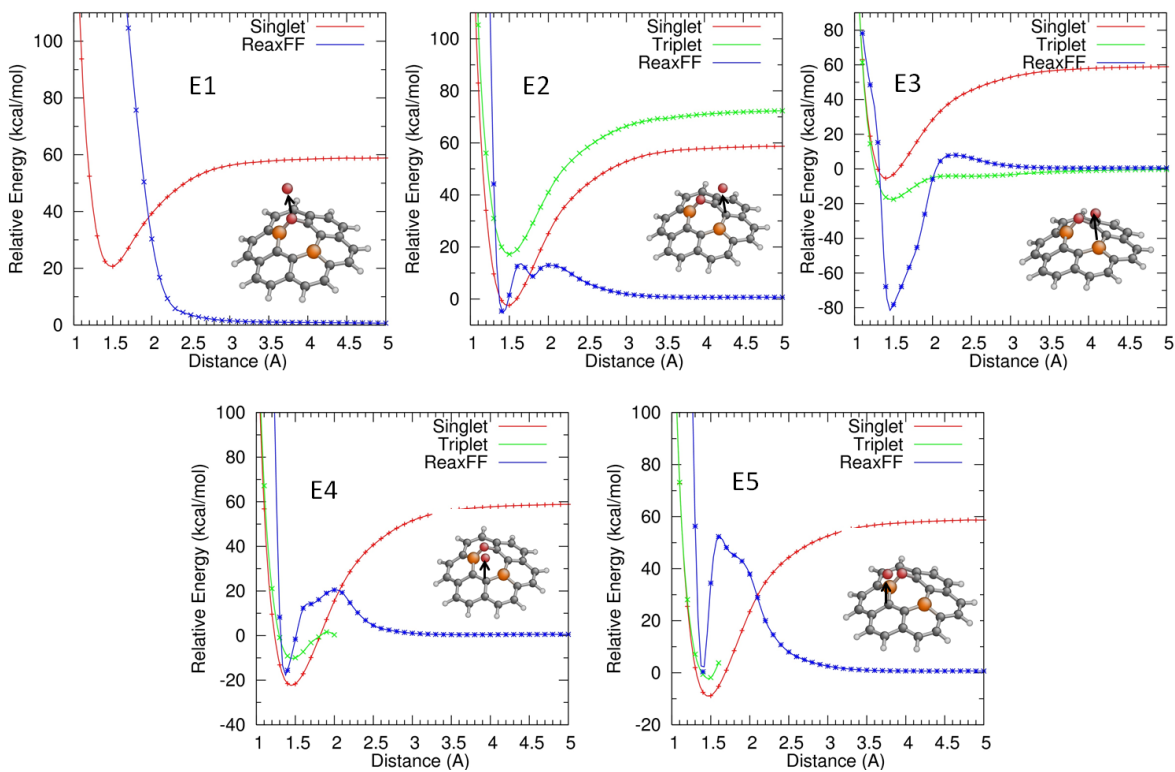


Figure 56: Binding energy curves for model E

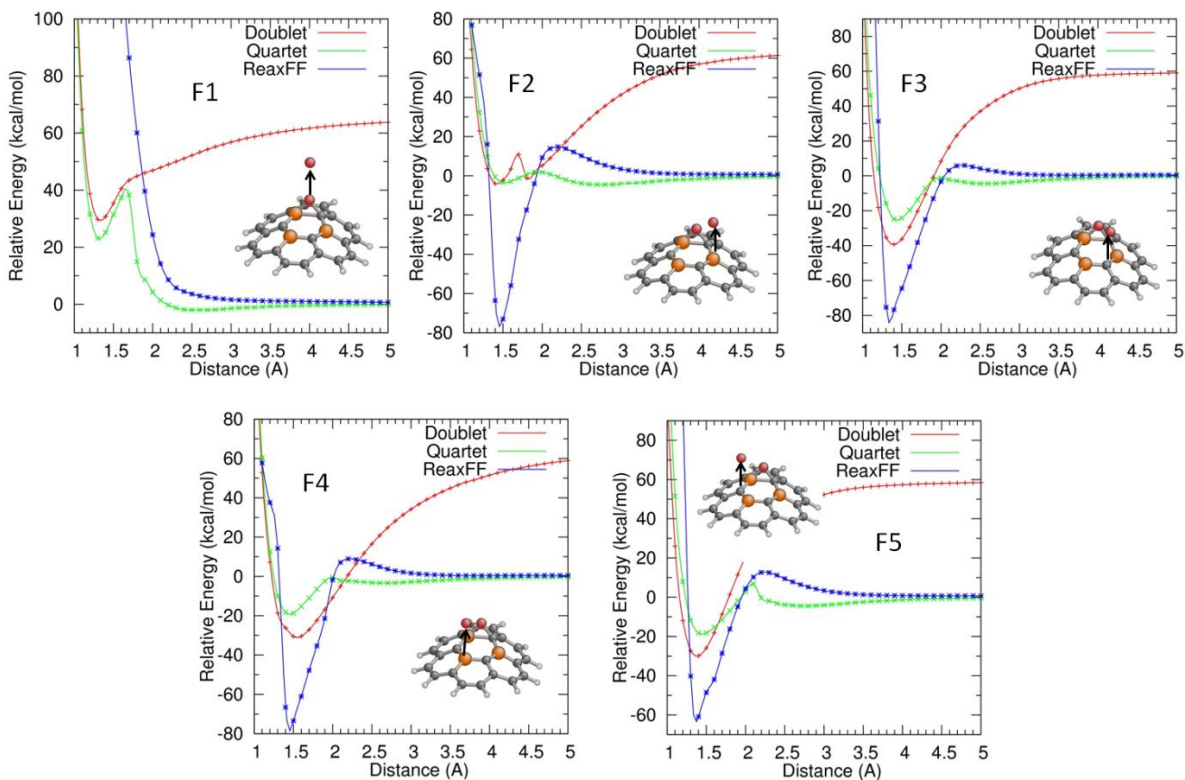


Figure 57: Binding energy curves for model F

From the above plots it is clear that while ReaxFF_{CHOB} is able to reproduce the qualitative trends similar to DFT, the potential has to be improved to obtain quantitative agreement. Re-parameterization of ReaxFF_{CHOB} for oxygen – boron doped graphene interactions will be carried out in the future. Once the potential has been reparameterized, it can be used for the molecular dynamics simulation of 5eV energetic oxygen atom impact with boron doped graphene and graphite samples at various surface temperatures and boron doping levels. The results from these simulations can then be used to obtain an Arrhenius type rate law for the mass loss upon impact of an oxygen atom. These results can then be compared directly with those from oxygen bombardment on graphite and diamond to suggest a strategy to limit the oxidative erosion of these materials in space based applications.

The primary focus of this work has been to study the chemistry and dynamics of hyperthermal oxidation and pyrolysis of carbon based materials through atomistic simulations using the ReaxFF reactive force field and to develop ReaxFF potentials for such applications. The following conclusions can be drawn based on the work done so far:

1. The ReaxFF C/H/O parameters³⁷ have been validated against DFT data and found to be well suited for the simulation of hyperthermal collisions of atomic oxygen with graphite and diamond.
2. Molecular dynamics simulations based on energetic oxygen atom bombardment on graphene and graphite using this potential showed that the erosion of these materials can be divided into distinct regimes. Graphene erodes via formation of epoxides on the surface followed by creation and growth of vacancy defects. Graphite breakup occurs via formation of epoxides on the top layer, creation of vacancy defects and their growth on the top layer, followed by the formation of epoxides on the bottom layer, defect creation and growth in the bottom layer. As such, the erosion of graphite basal planes was observed to be a layer by layer event.
3. The rate of growth of defects on graphite was observed to be faster in the basal plane directions than the axial direction, consistent with the anisotropic etching behavior observed in molecular beam experiments on highly ordered pyrolytic graphite.
4. Oxygen molecule formation from the surface occurred primarily via an Eley-Rideal type direct reaction mechanism.
5. The rate of loss of carbon atoms from graphite was found to be surface temperature dependent with the mass loss rate increasing with increase in surface temperature.
6. These simulations have been used to obtain Arrhenius parameters for the carbon atom loss rate from graphite basal planes, armchair and zigzag edges.

7. The erosion rates suggest that graphite basal planes are poorly resistant to energetic oxygen atom etching while the armchair and zigzag edges are an order of magnitude more resistant than basal plane.
8. At lower temperatures, the primary mode of mass loss from graphite basal planes is through CO₂ molecules but with increase in temperature, the primary mass loss mode changes to CO molecules. The number of CO₂ molecules lost decreases monotonically with increase in temperatures. In contrast, mass loss via CO₂ molecules remains the primary mode of mass loss from armchair and zigzag edges at all temperatures.
9. While the impinging oxygen atoms had hyperthermal energy (5eV) the reactions leading to the loss of a CO₂ molecule from the surface of graphite was observed to be thermal in nature.
10. ReaxFF simulations on small oxygen terminated low index diamond surfaces indicated that a variety of functional groups such as ethers, peroxides, oxy radicals and dioxetanes can form on the surface, in agreement with earlier experiments and first principles based calculations.
11. Successive energetic oxygen atom collisions on larger reconstructed diamond surfaces showed that all the low index surfaces, namely diamond(100), (111) and (110) can be etched by hyperthermal atomic oxygen with diamond(100) showing the lowest etching rate and diamond(110) presenting the largest etching rate. These results from these simulations have been used to obtain Arrhenius type parameters for the rate of carbon atom loss for diamond surfaces.
12. While diamond (100) and diamond (110) showed a linear variation of mass loss with time, diamond (111) showed a 'wavy' pattern, much like the oxidative erosion of graphite basal planes since diamond (111) surface is prone to graphitization and the rate of graphitization is known to increase with increase in temperature.
13. Irrespective of the nature of mass loss, the erosion yield of all the diamond surfaces was found to be about two orders of magnitude lower than graphite basal planes. These results indicate that diamond thin films with predominantly diamond (100) oriented grains could be a promising material for spacecraft applications in the low earth orbit environment.

14. The ReaxFF_{SiO}¹¹³ potential was extended to describe oxygen silica gas surface interactions by harvesting model clusters representative of (001) α -quartz surface and defects occurring on silica surfaces, obtaining DFT based binding energy curves for the approach of atomic and / or molecular oxygen to these clusters and retraining the ReaxFF_{SiO} potential to reproduce these curves. The new potential, titled ReaxFF_{SiO}^{GSI}, can now be employed in accurate large scale molecular dynamics simulations of oxygen silica gas surface interactions.
15. To study the mechanism of pyrolysis of an all carbon material, the thermal decomposition of a large fullerene (C₁₈₀) molecule was studied through high temperature molecular dynamics simulations.
16. Prior to these simulations, the ReaxFF C/H/O potential was re-parameterized to obtain a new potential (ReaxFF_{C-2013}) that can accurately describe the dynamics of carbon condensed phases.
17. Molecular dynamics simulations using ReaxFF_{C-2013} indicated that the decomposition large fullerenes can be divided into two regimes; an initial exponential regime where the fullerene loses mass through small fragments such as C₂ molecules but retains its cage like structure and a final linear regime where the mass loss rate accelerates through the loss of larger fragments such as C₄, C₅ etc. In the final linear regime, the fullerene loses its cage like structure and transforms into an amorphous phase.
18. The simulations were used to obtain Arrhenius parameters for the decomposition rate in both the regimes. While the decay of the molecule occurred primarily via the loss of C₂ units, with increase in temperature, the probability of loss of larger fragments was found to increase.
19. To develop ReaxFF_{CHOB} for oxygen – boron doped graphene gas surface interactions, model systems representative of boron doped graphene were identified and DFT based binding energy curves for the approach of an atomic oxygen to these models were obtained. Preliminary comparisons of ReaxFF_{CHOB} based binding energy profiles against DFT based data were obtained. Based on these comparisons, it was determined that ReaxFF_{CHOB} has to be re-optimized to describe oxygen – boron doped graphene interactions accurately.

References

1. Dressler, R. A., *Chemical Dynamics in Extreme Environments*; World Scientific Pub Co Inc, 2001.
2. Lessing, H. C. C., R. E.; *A Simple Atmosphere Reentry Guidance Scheme for Return from the Manned Mars Mission*; NASA Ames Research Center: 1966.
3. [Http://Www.Nasa.Gov/](http://www.nasa.gov/).
4. [Http://En.Wikipedia.Org/Wiki/Nasa_X-43](http://en.wikipedia.org/wiki/Nasa_X-43).
5. [Http://En.Wikipedia.Org/Wiki/Boeing_X-51](http://en.wikipedia.org/wiki/Boeing_X-51).
6. Da Rold, G., G., C.; Cavadias, S.; Amouroux, J., *Adv. Mat. Res.* **2010**, 89-91, 136-141.
7. Gosse, R. C., G. V.; In *Evaluation of Carbon-Carbon Ablation Models Using a Fully Coupled Cfd Solver*, AIAA-2008-3908, June 2008; 2008.
8. Cornell, W. D.; Cieplak, P.; Bayly, C. I.; Gould, I. R.; Merz, K. M.; Ferguson, D. M.; Spellmeyer, D. C.; Fox, T.; Caldwell, J. W.; Kollman, P. A., A Second Generation Force Field for the Simulation of Proteins, Nucleic Acids, and Organic Molecules. *J. Am. Chem. Soc.* **1995**, 117, 5179-5197.
9. Allinger, N. L.; Yuh, Y. H.; Lii, J. H., Molecular Mechanics. The Mm3 Force Field for Hydrocarbons. 1. *J. Am. Chem. Soc.* **1989**, 111, 8551-8566.
10. Lii, J. H.; Allinger, N. L., Molecular Mechanics. The Mm3 Force Field for Hydrocarbons. 2. Vibrational Frequencies and Thermodynamics. *J. Am. Chem. Soc.* **1989**, 111, 8566-8575.
11. Lii, J. H.; Allinger, N. L., Molecular Mechanics. The Mm3 Force Field for Hydrocarbons. 3. The Van Der Waals' Potentials and Crystal Data for Aliphatic and Aromatic Hydrocarbons. *J. Am. Chem. Soc.* **1989**, 111, 8576-8582.
12. van Duin, A. C. T.; Dasgupta, S.; Lorant, F.; Goddard, W. A., Reaxff: A Reactive Force Field for Hydrocarbons. *J. Phys. Chem. A* **2001**, 105, 9396-9409.
13. Abell, G. C., Empirical Chemical Pseudopotential Theory of Molecular and Metallic Bonding. *Phys. Rev. B* **1985**, 31, 6184-6196.
14. Tersoff, J., New Empirical Approach for the Structure and Energy of Covalent Systems. *Phys. Rev. B* **1988**, 37, 6991-7000.
15. Brenner, D. W., Empirical Potential for Hydrocarbons for Use in Simulating the Chemical Vapor Deposition of Diamond Films. *Phys. Rev. B* **1990**, 42, 9458-9471.
16. Stuart, S. J.; Tutein, A. B.; Harrison, J. A., A Reactive Potential for Hydrocarbons with Intermolecular Interactions. *J. Chem. Phys.* **2000**, 112, 6472-6486.
17. Yu, J.; Sinnott, S. B.; Phillpot, S. R., Charge Optimized Many-Body Potential for the Si/SiO₂ System. *Phys. Rev. B* **2007**, 75, 085311.
18. Shan, T.-R.; Devine, B. D.; Kemper, T. W.; Sinnott, S. B.; Phillpot, S. R., Charge-Optimized Many-Body Potential for the Hafnium/Hafnium Oxide System. *Phys. Rev. B* **2010**, 81, 125328.
19. Liang, T.; Shan, T.-R.; Cheng, Y.-T.; Devine, B. D.; Noordhoek, M.; Li, Y.; Lu, Z.; Phillpot, S. R.; Sinnott, S. B., Classical Atomistic Simulations of Surfaces and Heterogeneous Interfaces with the Charge-Optimized Many Body (Comb) Potentials. *Mat. Sci. & Eng: R* **2013**, 74, 255-279.
20. Janssens, G. O. A.; Baekelandt, B. G.; Toufar, H.; Mortier, W. J.; Schoonheydt, R. A., Comparison of Cluster and Infinite Crystal Calculations on Zeolites with the Electronegativity Equalization Method (Eem). *J. Phys. Chem.* **1995**, 99, 3251-3258.
21. Mortier, W. J.; Ghosh, S. K.; Shankar, S., Electronegativity-Equalization Method for the Calculation of Atomic Charges in Molecules. *J. Am. Chem. Soc.* **1986**, 108, 4315-4320.
22. de Vos Burchart, E.; Verheij, V. A.; van Bekkum, H.; van de Graaf, B., A Consistent Molecular Mechanics Force Field for All-Silica Zeolites. *Zeolites* **1992**, 12, 183-189.

23. Goverapet Srinivasan, S.; van Duin, A. C. T., Molecular-Dynamics-Based Study of the Collisions of Hyperthermal Atomic Oxygen with Graphene Using the Reaxff Reactive Force Field. *J. Phys. Chem. A* **2011**, *115*, 13269-13280.
24. Kinoshita, H.; Umeno, M.; Tagawa, M.; Ohmae, N., Hyperthermal Atomic Oxygen Beam-Induced Etching of HOPG (0001) Studied by X-Ray Photoelectron Spectroscopy and Scanning Tunneling Microscopy. *Surf. Sci.* **1999**, *440*, 49-59.
25. Ngo, T.; Snyder, E. J.; Tong, W. M.; Williams, R. S.; Anderson, M. S., O Atom Etching of Graphite in Low Earth Orbit. *Surf. Sci.* **1994**, *314*, L817-L822.
26. Nicholson, K. T.; Minton, T. K.; Sibener, S. J., Temperature-Dependent Morphological Evolution of HOPG Graphite Upon Exposure to Hyperthermal O(3p) Atoms. *Prog. Org. Coat.* **2003**, *47*, 443-447.
27. Nicholson, K. T.; Sibener, S. J.; Minton, T. K., Nucleation and Growth of Nanoscale to Microscale Cylindrical Pits in Highly-Ordered Pyrolytic Graphite Upon Hyperthermal Atomic Oxygen Exposure. *High Perform. Polym.* **2004**, *16*, 197-206.
28. Nicholson, K. T.; Minton, T. K.; Sibener, S. J., Spatially Anisotropic Etching of Graphite by Hyperthermal Atomic Oxygen. *J. Phys. Chem. B* **2005**, *109*, 8476-8480.
29. Cohen, L. K., A Lower Bound on the Loss of Graphite by Atomic Oxygen Attack at Asymptotic Energy. *J. Chem. Phys.* **1993**, *99*, 9652-9663.
30. Radovic, L. R., Active Sites in Graphene and the Mechanism of CO₂ Formation in Carbon Oxidation. *J. Am. Chem. Soc.* **2009**, *131*, 17166-17175.
31. Hall, P. J.; Calo, J. M., Secondary Interactions Upon Thermal Desorption of Surface Oxides from Coal Chars. *Energy & Fuels* **1989**, *3*, 370-376.
32. Incze, A.; Pasturel, A.; Chatillon, C., Oxidation of Graphite by Atomic Oxygen: A First-Principles Approach. *Surf. Sci.* **2003**, *537*, 55-63.
33. Sánchez, A.; Mondragón, F., Role of the Epoxy Group in the Heterogeneous CO₂ Evolution in Carbon Oxidation Reactions. *J. Phys. Chem. C* **2006**, *111*, 612-617.
34. Sun, T.; Fabris, S.; Baroni, S., Surface Precursors and Reaction Mechanisms for the Thermal Reduction of Graphene Basal Surfaces Oxidized by Atomic Oxygen. *J. Phys. Chem. C* **2011**, *115*, 4730-4737.
35. Bagri, A.; Mattevi, C.; Acik, M.; Chabal, Y. J.; Chhowalla, M.; Shenoy, V. B., Structural Evolution During the Reduction of Chemically Derived Graphene Oxide. *Nat. Chem.* **2010**, *2*, 581-587.
36. Bagri, A.; Grantab, R.; Medhekar, N. V.; Shenoy, V. B., Stability and Formation Mechanisms of Carbonyl- and Hydroxyl-Decorated Holes in Graphene Oxide. *J. Phys. Chem. C* **2010**, *114*, 12053-12061.
37. Chenoweth, K.; van Duin, A. C. T.; Goddard III, W. A., Reaxff Reactive Force Field for Molecular Dynamics Simulations of Hydrocarbon Oxidation. *J. Phys. Chem. A* **2008**, *112*, 1040-1053.
38. Chenoweth, K.; Van Duin, A. C. T.; Dasgupta, S.; Goddard III, W. A., Initiation Mechanisms and Kinetics of Pyrolysis and Combustion of JP-10 Hydrocarbon Jet Fuel. *J. Phys. Chem. A* **2009**, *113*, 1740-1746.
39. Castro-Marcano, F.; Kamat, A. M.; Russo, M. F.; van Duin, A. C. T.; Mathews, J. P., Combustion of an Illinois No. 6 Coal Char Simulated Using an Atomistic Char Representation and the Reaxff Reactive Force Field. *Combustion and Flame* **2011**.
40. Qian, H. J.; van Duin, A. C. T.; Morokuma, K.; Irle, S., Reactive Molecular Dynamics Simulation of Fullerene Combustion Synthesis: Reaxff Vs DFTB Potentials. *J. Chem. Theory Comput.* **2011**, *7*, 2040-2048.
41. Poovathingal, S.; Schwartzentruber, T. E.; Srinivasan, S. G.; van Duin, A. C. T., Large Scale Computational Chemistry Modeling of the Oxidation of Highly Oriented Pyrolytic Graphite. *J. Phys. Chem. A* **2013**, *117*, 2692-2703.
42. Orrego, J. F.; Zapata, F.; Truong, T. N.; Mondragón, F., Heterogeneous CO₂ Evolution from Oxidation of Aromatic Carbon-Based Materials. *J. Phys. Chem. A* **2009**, *113*, 8415-8420.

43. Paci, J. T.; Upadhyaya, H. P.; Zhang, J.; Schatz, G. C.; Minton, T. K., Theoretical and Experimental Studies of the Reactions between Hyperthermal O(3p) and Graphite: Graphene-Based Direct Dynamics and Beam-Surface Scattering Approaches†. *J. Phys. Chem. A* **2009**, *113*, 4677-4685.
44. Perdew, J. P.; Burke, K.; Ernzerhof, M., Generalized Gradient Approximation Made Simple. *Phys. Rev. Lett.* **1996**, *77*, 3865-3868.
45. Isborn, C. M.; Li, X.; Tully, J. C., Time-Dependent Density Functional Theory Ehrenfest Dynamics: Collisions between Atomic Oxygen and Graphite Clusters. *J. Chem. Phys.* **2007**, *126*, 134307-7.
46. Berendsen, H. J. C.; Postma, J. P. M.; van Gunsteren, W. F.; DiNola, A.; Haak, J. R., Molecular Dynamics with Coupling to an External Bath. *J. Chem. Phys.* **1984**, *81*, 3684-3690.
47. Hahn, J. R., Kinetic Study of Graphite Oxidation Along Two Lattice Directions. *Carbon* **2005**, *43*, 1506-1511.
48. Buczala, D. M.; Brunsvold, A. L.; Minton, T. K., Erosion of Kapton H® by Hyperthermal Atomic Oxygen. *J. Spacecr. Rockets* **2006**, *43*, 421-425.
49. Leyva, I. A.; Laurence, S.; Beierholm, A. W.; Hornung, H. G.; Wagnild, R.; Candler, G., *Transition Delay in Hypervelocity Boundary Layers by Means of Co2/Acoustic Instability Interactions*; Defense Technical Information Center, 2008.
50. Wagnild, R. M.; Candler, G. V.; Leyva, I. A.; Jewell, J. S.; Hornung, H. G., *Carbon Dioxide Injection for Hypervelocity Boundary Layer Stability*; Defense Technical Information Center, 2009.
51. Jewell, J.; Leyva, I.; Parziale, N. J.; Shepherd, J. E. In *Effect of Gas Injection on Transition in Hypervelocity Boundary Layers*, 28th International Symposium on Shock Waves, Springer: 2012; pp 735-740.
52. Li, J.-L.; Kudin, K. N.; McAllister, M. J.; Prud'homme, R. K.; Aksay, I. A.; Car, R., Oxygen-Driven Unzipping of Graphitic Materials. *Phys. Rev. Lett.* **2006**, *96*, 176101.
53. Goverapet Srinivasan, S.; van Duin, A. C. T., Direction Dependent Etching of Diamond Surfaces by Hyperthermal Atomic Oxygen: A Reaxff Based Molecular Dynamics Study. *Carbon* **2014**, *Submitted for review*.
54. Joshi, A.; Nimmagadda, R., Erosion of Diamond Films and Graphite in Oxygen Plasma. *J. Mater. Res.* **1991**, *6*, 1484-1490.
55. Grogan, D. F.; Zhao, T.; Bovard, B. G.; Macleod, H. A., Planarizing Technique for Ion-Beam Polishing of Diamond Films. *Appl. Opt.* **1992**, *31*, 1483-1487.
56. Ral'chenko, V. G.; Korotushenko, K. G.; Smolin, A. A.; Loubnin, E. N., Fine Patterning of Diamond Films by Laser-Assisted Chemical Etching in Oxygen. *Diamond Relat. Mater.* **1995**, *4*, 893-896.
57. Sandhu, G. S.; Chu, W. K., Reactive Ion Etching of Diamond. *Appl. Phys. Lett.* **1989**, *55*, 437-438.
58. de Theije, F. K.; van der Laag, N. J.; Plomp, M.; van Enckevort, W. J. P., A Surface Topographic Investigation of {001} Diamond Surfaces Etched in Oxygen. *Philos. Mag. A* **2000**, *80*, 725-745.
59. de Theije, F. K.; Roy, O.; van der Laag, N. J.; van Enckevort, W. J. P., Oxidative Etching of Diamond. *Diamond Relat. Mater.* **2000**, *9*, 929-934.
60. John, P.; Polwart, N.; Troupe, C. E.; Wilson, J. I. B., The Oxidation of (100) Textured Diamond. *Diamond Relat. Mater.* **2002**, *11*, 861-866.
61. Loh, K. P.; Xie, X. N.; Lim, Y. H.; Teo, E. J.; Zheng, J. C.; Ando, T., Surface Oxygenation Studies on (1 0 0)-Oriented Diamond Using an Atom Beam Source and Local Anodic Oxidation. *Surf. Sci.* **2002**, *505*, 93-114.
62. Pehrsson, P. E.; Mercer, T. W.; Chaney, J. A., Thermal Oxidation of the Hydrogenated Diamond (1 0 0) Surface. *Surf. Sci.* **2002**, *497*, 13-28.
63. Nimmagadda, R. R.; Joshi, A.; Hsu, W. L., Role of Microstructure on the Oxidation Behavior of Microwave Plasma Synthesized Diamond and Diamond-Like Carbon Films. *J. Mater. Res.* **1990**, *5*, 2445-2450.

64. Sun, Q.; Alam, M., Relative Oxidation Behavior of Chemical Vapor Deposited and Type IIa Natural Diamonds. *J. Electrochem. Soc.* **1992**, *139*, 933-936.
65. de Theije, F. K.; van Veenendaal, E.; van Enckevort, W. J. P.; Vlieg, E., Oxidative Etching of Cleaved Synthetic Diamond {111} Surfaces. *Surf. Sci.* **2001**, *492*, 91-105.
66. Li, J., et al., Reaction of Diamond Thin Films with Atomic Oxygen Simulated as Low-Earth-Orbit Environment. *J. Appl. Phys.* **2002**, *92*, 6275-6277.
67. Li, J.; Zhang, Q.; Yoon, S. F.; Ahn, J.; Zhou, Q.; Wang, S.; Yang, D.; Wang, Q., Erosion Resistance of Polycrystalline Diamond Films to Atomic Oxygen. *Carbon* **2003**, *41*, 1847-1850.
68. Shpilman, Z.; Gouzman, I.; Grossman, E.; Akhvlediani, R.; Hoffman, A., Oxidation of Diamond Films by Atomic Oxygen: High Resolution Electron Energy Loss Spectroscopy Studies. *J. Appl. Phys.* **2007**, *102*, 114914.
69. Shpilman, Z.; Gouzman, I.; Grossman, E.; Akhvlediani, R.; Hoffman, A., Hydrogen Plasma and Atomic Oxygen Treatments of Diamond: Chemical Versus Morphological Effects. *Appl. Phys. Lett.* **2008**, *92*, 234103.
70. Shpilman, Z.; Gouzman, I.; Grossman, E.; Akhvlediani, R.; Hoffman, A., Chemical and Morphological Aspects of Diamond Film Oxidation and Regeneration. *physica status solidi (a)* **2008**, *205*, 2130-2135.
71. Shpilman, Z.; Gouzman, I.; Grossman, E.; Shen, L.; Minton, T. K.; Hoffman, A., Resistance of Diamond (100) to Hyperthermal Atomic Oxygen Attack. *Appl. Phys. Lett.* **2009**, *95*, 174106.
72. Shpilman, Z.; Gouzman, I.; Grossman, E.; Shen, L.; Minton, T. K.; Paci, J. T.; Schatz, G. C.; Akhvlediani, R.; Hoffman, A., Oxidation and Etching of Cvd Diamond by Thermal and Hyperthermal Atomic Oxygen. *J. Phys. Chem. C* **2010**, *114*, 18996-19003.
73. Skokov, S.; Weiner, B.; Frenklach, M., Molecular-Dynamics Study of Oxygenated (100) Diamond Surfaces. *Phys. Rev. B* **1994**, *49*, 11374-11382.
74. Larsson, K.; Björkman, H.; Hjort, K., Role of Water and Oxygen in Wet and Dry Oxidation of Diamond. *J. Appl. Phys.* **2001**, *90*, 1026-1034.
75. Petrini, D.; Larsson, K., A Theoretical Study of the Energetic Stability and Geometry of Hydrogen- and Oxygen-Terminated Diamond (100) Surfaces. *J. Phys. Chem. C* **2006**, *111*, 795-801.
76. Petrini, D.; Larsson, K., Theoretical Study of the Thermodynamic and Kinetic Aspects of Terminated (111) Diamond Surfaces. *J. Phys. Chem. C* **2008**, *112*, 3018-3026.
77. Zheng, X. M.; Smith, P. V., The Stable Configurations for Oxygen Chemisorption on the Diamond (100) and (111) Surfaces. *Surf. Sci.* **1992**, *262*, 219-234.
78. Paci, J. T.; Schatz, G. C.; Minton, T. K., Theoretical Studies of the Erosion of (100) and (111) Diamond Surfaces by Hyperthermal O(³p). *J. Phys. Chem. C* **2011**, *115*, 14770-14777.
79. Paci, J. T.; Minton, T. K.; Schatz, G. C., Hyperthermal Oxidation of Graphite and Diamond. *Acc. Chem. Res.* **2012**, *45*, 1973-1981.
80. Ju, L., Atomeye: An Efficient Atomistic Configuration Viewer. *Modell. Simul. Mater. Sci. Eng.* **2003**, *11*, 173.
81. Elstner, M.; Porezag, D.; Jungnickel, G.; Elsner, J.; Haugk, M.; Frauenheim, T.; Suhai, S.; Seifert, G., Self-Consistent-Charge Density-Functional Tight-Binding Method for Simulations of Complex Materials Properties. *Phys. Rev. B* **1998**, *58*, 7260-7268.
82. José, M. S.; Emilio, A.; Julian, D. G.; Alberto, G.; Javier, J.; Pablo, O.; Daniel, S.-P., The Siesta Method for Ab Initio Order- N Materials Simulation. *J. Phys.: Condens. Matter* **2002**, *14*, 2745.
83. Perdew, J. P.; Burke, K.; Ernzerhof, M., Generalized Gradient Approximation Made Simple [Phys. Rev. Lett. *77*, 3865 (1996)]. *Phys. Rev. Lett.* **1997**, *78*, 1396-1396.
84. Troullier, N.; Martins, J. L., Efficient Pseudopotentials for Plane-Wave Calculations. *Phys. Rev. B* **1991**, *43*, 1993-2006.

85. Troullier, N.; Martins, J. L., Efficient Pseudopotentials for Plane-Wave Calculations. II. Operators for Fast Iterative Diagonalization. *Phys. Rev. B* **1991**, *43*, 8861-8869.
86. Köhler, C.; Hajnal, Z.; Deák, P.; Frauenheim, T.; Suhai, S., Theoretical Investigation of Carbon Defects and Diffusion in α -Quartz. *Phys. Rev. B* **2001**, *64*, 085333.
87. Köhler, C.; Frauenheim, T., Molecular Dynamics Simulations of Cf_x ($X = 2, 3$) Molecules at Si_3N_4 and SiO_2 Surfaces. *Surf. Sci.* **2006**, *600*, 453-460.
88. Evans, T.; James, P., A Study of the Transformation of Diamond to Graphite. *Proc. R. Soc. London, Ser. A* **1964**, *277*, 260-269.
89. Davies, G.; Evans, T., Graphitization of Diamond at Zero Pressure and at a High Pressure. *Proc. R. Soc. London, Ser. A* **1972**, *328*, 413-427.
90. De Vita, A.; Galli, G.; Canning, A.; Car, R., A Microscopic Model for Surface-Induced Diamond-to-Graphite Transitions. *Nature* **1996**, *379*, 523-526.
91. Bourdon, E. B. D.; Raveh, A.; Gujrathi, S. C.; Martinu, L., Etching of a -C:H Films by an Atomic Oxygen Beam. *J. Vac. Sci. Technol., A* **1993**, *11*, 2530-2535.
92. Kulkarni, A. D.; Truhlar, D. G.; Goverapet Srinivasan, S.; van Duin, A. C. T.; Norman, P.; Schwartzenuber, T. E., Oxygen Interactions with Silica Surfaces: Coupled Cluster and Density Functional Investigation and the Development of a New Reaxff Potential. *J. Phys. Chem. C* **2012**, *117*, 258-269.
93. Balat-Pichelin, M.; Badie, J. M.; Berjoan, R.; Boubert, P., Recombination Coefficient of Atomic Oxygen on Ceramic Materials under Earth Re-Entry Conditions by Optical Emission Spectroscopy. *Chem. Phys.* **2003**, *291*, 181-194.
94. Alfano, D.; Scatteia, L.; Monteverde, F.; Bêche, E.; Balat-Pichelin, M., Microstructural Characterization of ZrB₂-SiC Based Uhtc Tested in the Mesox Plasma Facility. *J. Eur. Ceram. Soc.* **2010**, *30*, 2345-2355.
95. Barbato, M.; Reggiani, S.; Bruno, C.; Muylaert, J., Model for Heterogeneous Catalysis on Metal Surfaces with Applications to Hypersonic Flows. *J. Thermophys Heat Transfer* **2000**, *14*, 412-420.
96. Macko, P.; Veis, P.; Cernogora, G., Study of Oxygen Atom Recombination on a Pyrex Surface at Different Wall Temperatures by Means of Time-Resolved Actinometry in a Double Pulse Discharge Technique. *Plasma Sources Science & Technology* **2004**, *13*, 251-262.
97. Kim, Y. C.; Boudart, M., Recombination of O, N, and H-Atoms on Silica - Kinetics and Mechanism. *Langmuir* **1991**, *7*, 2999-3005.
98. Carleton, K. L.; Marinelli, W. J., Spacecraft Thermal Energy Accommodation from Atomic Recombination. *Journal of Thermophys. Heat Transfer* **1992**, *6*, 650-655.
99. Cartry, G.; Duten, X.; Rousseau, A., Atomic Oxygen Surface Loss Probability on Silica in Microwave Plasmas Studied by a Pulsed Induced Fluorescence Technique. *Plasma Sources Science & Technology* **2006**, *15*, 479-488.
100. Marschall, J., Experimental Determination of Oxygen and Nitrogen Recombination Coefficients at Elevated Temperature Using Laser-Induced Fluorescence. *AIAA 97-3879* **1997**, Baltimore, MD.
101. Bedra, L.; Balat-Pichelin, M. J. H., Comparative Modeling Study and Experimental Results of Atomic Oxygen Recombination on Silica-Based Surfaces at High Temperature. *Aerospace Science and Technology* **2005**, *9*, 318-328.
102. Arasa, C.; Gamallo, P.; Sayos, R., Adsorption of Atomic Oxygen and Nitrogen at Beta-Cristobalite(100): A Density Functional Theory Study. *J. Phys. Chem. B* **2005**, *109*, 14954-14964.
103. Arasa, C.; Busnengo, H. F.; Salin, A.; Sayos, R., Classical Dynamics Study of Atomic Oxygen Sticking on the Beta-Cristobalite (100) Surface. *Surf. Sci.* **2008**, *602*, 975-985.
104. Arasa, C.; Moron, V.; Busnengo, H. F.; Sayos, R., Eley-Rideal Reaction Dynamics between O Atoms on Beta-Cristobalite (100) Surface: A New Interpolated Potential Energy Surface and Classical Trajectory Study. *Surf. Sci.* **2009**, *603*, 2742-2751.

105. Moron, V.; Gamallo, P.; Martin-Gondre, L.; Crespos, C.; Larregaray, P.; Sayos, R., Recombination and Chemical Energy Accommodation Coefficients from Chemical Dynamics Simulations: O/O(2) Mixtures Reacting over a Beta-Cristobalite (001) Surface. *PCCP* **2011**, *13*, 17494-17504.
106. Cacciatore, M.; Rutigliano, M.; Billing, G. D., Eley-Rideal and Langmuir-Hinshelwood Recombination Coefficients for Oxygen on Silica Surfaces. *J. Thermophys Heat Transfer* **1999**, *13*, 195-203.
107. Sander, M. J.; Leslie, M.; Catlow, C. R. A., *J. Chem. Soc. Chem. Commun.* **1984**, 1271.
108. Tsuneyuki, S.; Tsukada, M.; Aoki, H.; Matsui, Y., *Phys. Rev. Lett.* **1988**, *61*, 869.
109. van Beest, B. W.; Kramer, G. J.; van Santen, R. A., Force Fields for Silicas and Aluminophosphates Based on Ab Initio Calculations. *Phys Rev Lett* **1990**, *64*, 1955-1958.
110. Belonoshko, A. B.; Dubrovinsky, L. S., *Geochim. Cosmochim. Acta* **1995**, *59*, 1883.
111. Ermoshin, V. A.; Smirnov, K. S.; Bougeard, D., *Chem. Phys.* **1996**, *202*, 53.
112. Roder, A.; Kob, W.; Binder, K., Structure and Dynamics of Amorphous Silica Surfaces. *J. Chem. Phys.* **2001**, *114*, 7602-7614.
113. van Duin, A. C. T.; Strachan, A.; Stewman, S.; Zhang, Q. S.; Xu, X.; Goddard, W. A., Reaxff(Sio) Reactive Force Field for Silicon and Silicon Oxide Systems. *J. Phys. Chem. A* **2003**, *107*, 3803-3811.
114. Chenoweth, K.; Cheung, S.; van Duin, A. C.; Goddard, W. A., 3rd; Kober, E. M., Simulations on the Thermal Decomposition of a Poly(Dimethylsiloxane) Polymer Using the Reaxff Reactive Force Field. *J Am Chem Soc* **2005**, *127*, 7192-202.
115. Buehler, M. J.; Tang, H.; van Duin, A. C.; Goddard, W. A., 3rd, Threshold Crack Speed Controls Dynamical Fracture of Silicon Single Crystals. *Phys Rev Lett* **2007**, *99*, 165502.
116. Sen, D. C., Alan ; Thompson, Aidan P. ; Van Duin, Adri ; Goddard III, William A. ; Buehler, Markus J In *Direct Atomistic Simulation of Brittle-to-Ductile Transition in Silicon Single Crystals*, MRS Proceedings, 2010.
117. Ning, N.; Calvo, F.; van Duin, A. C. T.; Wales, D. J.; Vach, H., Spontaneous Self-Assembly of Silica Nanocages into Inorganic Framework Materials. *J. Phys. Chem. C* **2008**, *113*, 518-523.
118. Neyts, E. C.; Khalilov, U.; Pourtois, G.; van Duin, A. C. T., Hyperthermal Oxygen Interacting with Silicon Surfaces: Adsorption, Implantation, and Damage Creation. *J. Phys. Chem. C* **2011**, *115*, 4818-4823.
119. Khalilov, U.; Neyts, E. C.; Pourtois, G.; van Duin, A. C. T., Can We Control the Thickness of Ultrathin Silica Layers by Hyperthermal Silicon Oxidation at Room Temperature? *J. Phys. Chem. C* **2011**, *115*, 24839-24848.
120. Khalilov, U.; Pourtois, G.; Duin, A. C. T. v.; Neyts, E. C., Self-Limiting Oxidation in Small-Diameter Si Nanowires. *Chem. Mater.* **2012**, *24*, 2141-2147.
121. Khalilov, U.; Pourtois, G.; van Duin, A. C. T.; Neyts, E. C., Hyperthermal Oxidation of Si(100)2x1 Surfaces: Effect of Growth Temperature. *J. Phys. Chem. C* **2012**, *116*, 8649-8656.
122. Steurer, W.; Apfalter, A.; Koch, M.; Sarlat, T.; Sondergard, E.; Ernst, W. E.; Holst, B., The Structure of the Alpha-Quartz (0001) Surface Investigated Using Helium Atom Scattering and Atomic Force Microscopy. *Surf. Sci.* **2007**, *601*, 4407-4411.
123. Zhao, Y.; Truhlar, D., The M06 Suite of Density Functionals for Main Group Thermochemistry, Thermochemical Kinetics, Noncovalent Interactions, Excited States, and Transition Elements: Two New Functionals and Systematic Testing of Four M06-Class Functionals and 12 Other Functionals. *Theoretical Chemistry Accounts: Theory, Computation, and Modeling (Theoretica Chimica Acta)* **2008**, *120*, 215-241.
124. Zhao, Y.; Truhlar, D. G., A New Local Density Functional for Main-Group Thermochemistry, Transition Metal Bonding, Thermochemical Kinetics, and Noncovalent Interactions. *J. Chem. Phys.* **2006**, *125*, 194101-18.
125. Weigend, F.; Ahlrichs, R., Balanced Basis Sets of Split Valence, Triple Zeta Valence and Quadruple Zeta Valence Quality for H to Rn: Design and Assessment of Accuracy. *PCCP* **2005**, *7*, 3297-3305.

126. van Duin, A. C. T.; Baas, J. M. A.; van de Graaf, B., Delft Molecular Mechanics: A New Approach to Hydrocarbon Force Fields. Inclusion of a Geometry-Dependent Charge Calculation. *J. Chem. Soc., Faraday Trans.* **1994**, *90*, 2881-2895.
127. Norman, P.; Schwartzentruber, T. E.; Leverentz, H.; Luo, S.; Meana-Pañeda, R.; Paukku, Y.; Truhlar, D. G., The Structure of Silica Surfaces Exposed to Atomic Oxygen. *J. Phys. Chem. C* **2013**, *117*, 9311-9321.
128. Goverapet Srinivasan, S.; van Duin, A. C. T.; Ganesh, P., Development of a Reaxff Potential for Carbon Condensed Phases and Its Application to the Thermal Fragmentation of a Large Fullerene. *J. Phys. Chem. A* **2014**, *Submitted for review*.
129. Kroto, H. W.; Heath, J. R.; O'Brien, S. C.; Curl, R. F.; Smalley, R. E., C60: Buckminsterfullerene. *Nature* **1985**, *318*, 162-163.
130. Zhang, Q. L.; O'Brien, S. C.; Heath, J. R.; Liu, Y.; Curl, R. F.; Kroto, H. W.; Smalley, R. E., Reactivity of Large Carbon Clusters: Spheroidal Carbon Shells and Their Possible Relevance to the Formation and Morphology of Soot. *J. Phys. Chem.* **1986**, *90*, 525-528.
131. Smalley, R. E., Self-Assembly of the Fullerenes. *Acc. Chem. Res.* **1992**, *25*, 98-105.
132. von Helden, G.; Gotts, N. G.; Bowers, M. T., Experimental Evidence for the Formation of Fullerenes by Collisional Heating of Carbon Rings in the Gas Phase. *Nature* **1993**, *363*, 60-63.
133. Heath, J. R., Fullerenes: C60's Smallest Cousin. *Nature* **1998**, *393*, 730-731.
134. Bates, K. R.; Scuseria, G. E., Energetic Analysis of Pentagon Road Intermediates of C60-Buckminsterfullerene Formation. *J. Phys. Chem. A* **1997**, *101*, 3038-3041.
135. Irle, S.; Zheng, G.; Elstner, M.; Morokuma, K., From C2 Molecules to Self-Assembled Fullerenes in Quantum Chemical Molecular Dynamics. *Nano Lett.* **2003**, *3*, 1657-1664.
136. Irle, S.; Zheng, G.; Wang, Z.; Morokuma, K., The C60 Formation Puzzle "Solved": Qm/Md Simulations Reveal the Shrinking Hot Giant Road of the Dynamic Fullerene Self-Assembly Mechanism. *J. Phys. Chem. B* **2006**, *110*, 14531-14545.
137. Irle, S.; Zheng, G.; Wang, Z.; Morokuma, K., Theory-Experiment Relationship of the "Shrinking Hot Giant" Road of Dynamic Fullerene Self-Assembly in Hot Carbon Vapor. *Nano* **2007**, *02*, 21-30.
138. Saha, B.; Shindo, S.; Irle, S.; Morokuma, K., Quantum Chemical Molecular Dynamics Simulations of Dynamic Fullerene Self-Assembly in Benzene Combustion. *ACS Nano* **2009**, *3*, 2241-2257.
139. Irle, S.; Zheng, G.; Elstner, M.; Morokuma, K., Formation of Fullerene Molecules from Carbon Nanotubes: A Quantum Chemical Molecular Dynamics Study. *Nano Lett.* **2003**, *3*, 465-470.
140. Zheng, G.; Irle, S.; Elstner, M.; Morokuma, K., Quantum Chemical Molecular Dynamics Model Study of Fullerene Formation from Open-Ended Carbon Nanotubes†. *J. Phys. Chem. A* **2004**, *108*, 3182-3194.
141. Porezag, D.; Frauenheim, T.; Köhler, T.; Seifert, G.; Kaschner, R., Construction of Tight-Binding-Like Potentials on the Basis of Density-Functional Theory: Application to Carbon. *Phys. Rev. B* **1995**, *51*, 12947-12957.
142. O'Brien, S. C.; Heath, J. R.; Curl, R. F.; Smalley, R. E., Photophysics of Buckminsterfullerene and Other Carbon Cluster Ions. *J. Chem. Phys.* **1988**, *88*, 220-230.
143. Stone, A. J.; Wales, D. J., Theoretical Studies of Icosahedral C60 and Some Related Species. *Chem. Phys. Lett.* **1986**, *128*, 501-503.
144. Murry, R. L.; Strout, D. L.; Odom, G. K.; Scuseria, G. E., Role of Sp3 Carbon and 7-Membered Rings in Fullerene Annealing and Fragmentation. *Nature* **1993**, *366*, 665-667.
145. Murry, R. L.; Strout, D. L.; Scuseria, G. E., Theoretical Studies of Fullerene Annealing and Fragmentation. *Int. J. Mass Spectrom. Ion Processes* **1994**, *138*, 113-131.
146. Wang, C. Z.; Xu, C. H.; Chan, C. T.; Ho, K. M., Disintegration and Formation of Fullerene (C60). *J. Phys. Chem.* **1992**, *96*, 3563-3565.

147. Zhang, B. L.; Wang, C. Z.; Chan, C. T.; Ho, K. M., Thermal Disintegration of Carbon Fullerenes. *Phys. Rev. B* **1993**, *48*, 11381-11384.
148. Kim, E.; Lee, Y. H.; Lee, J. Y., Fragmentation of C₆₀ and C₇₀ Clusters. *Phys. Rev. B* **1993**, *48*, 18230-18234.
149. Kim, S. G.; Tománek, D., Melting the Fullerenes: A Molecular Dynamics Study. *Phys. Rev. Lett.* **1994**, *72*, 2418-2421.
150. Xu, C.; Scuseria, G. E., Tight-Binding Molecular Dynamics Simulations of Fullerene Annealing and Fragmentation. *Phys. Rev. Lett.* **1994**, *72*, 669-672.
151. Openov, L. A.; Podlivaev, A. I., Simulation of the Thermal Fragmentation of Fullerene C₆₀. *JETP Letters* **2006**, *84*, 68-72.
152. Zheng, G.; Wang, Z.; Irle, S.; Morokuma, K., Quantum Chemical Molecular Dynamics Study of "Shrinking" of Hot Giant Fullerenes. *Journal of Nanoscience and Nanotechnology* **2007**, *7*, 1662-1669.
153. Grimme, S., Semiempirical GGA-Type Density Functional Constructed with a Long-Range Dispersion Correction. *J. Comput. Chem.* **2006**, *27*, 1787-1799.
154. Kresse, G.; Joubert, D., From ultrasoft pseudopotentials to the projector augmented-wave method. *Phys. Rev. B* **1999**, *59*, 1758-1775.
155. Blöchl, P. E., Projector augmented-wave method. *Phys. Rev. B* **1994**, *50*, 17953-17979.
156. Bochevarov, A. D.; Harder, E.; Hughes, T. F.; Greenwood, J. R.; Braden, D. A.; Philipp, D. M.; Rinaldo, D.; Halls, M. D.; Zhang, J.; Friesner, R. A., Jaguar: A High-Performance Quantum Chemistry Software Program with Strengths in Life and Materials Sciences. *Int. J. Quantum Chem* **2013**, *113*, 2110-2142.
157. Krishnan, R.; Binkley, J. S.; Seeger, R.; Pople, J. A., Self-consistent molecular orbital methods. Xx. A basis set for correlated wave functions. *J. Chem. Phys.* **1980**, *72*, 650-654.
158. Becke, A. D., Density-functional exchange-energy approximation with correct asymptotic behavior. *Phys. Rev. A* **1988**, *38*, 3098-3100.
159. Lee, C.; Yang, W.; Parr, R. G., Development of the Colle-Salvetti correlation-energy formula into a functional of the electron density. *Phys. Rev. B* **1988**, *37*, 785-789.
160. Stephens, P. J.; Devlin, F. J.; Chabalowski, C. F.; Frisch, M. J., Ab initio calculation of vibrational absorption and circular dichroism spectra using density functional force fields. *J. Phys. Chem.* **1994**, *98*, 11623-11627.
161. Humphrey, W.; Dalke, A.; Schulten, K., Vmd: Visual Molecular Dynamics. *Journal of molecular graphics* **1996**, *14*, 33-38.
162. Kittel, C.; McEuen, P., *Introduction to Solid State Physics*; Wiley New York, 1996; Vol. 7.
163. Calaminici, P.; Geudtner, G.; Köster, A. M., First-principle calculations of large fullerenes. *J. Chem. Theory Comput.* **2008**, *5*, 29-32.
164. Bettinger, H. F.; Yakobson, B. I.; Scuseria, G. E., Scratching the surface of buckminsterfullerene: The barriers for Stone-Wales transformation through symmetric and asymmetric transition states. *J. Am. Chem. Soc.* **2003**, *125*, 5572-5580.
165. Saha, B.; Irle, S.; Morokuma, K., Hot giant fullerenes eject and capture C₂ molecules: QM/MD simulations with constant density. *J. Phys. Chem. C* **2011**, *115*, 22707-22716.
166. Marcos, P. A.; López, M. J.; Rubio, A.; Alonso, J. A., Thermal road for fullerene annealing. *Chem. Phys. Lett.* **1997**, *273*, 367-370.
167. Huang, J. Y.; Ding, F.; Jiao, K.; Yakobson, B. I., Real time microscopy, kinetics, and mechanism of giant fullerene evaporation. *Phys. Rev. Lett.* **2007**, *99*, 175503.
168. Rojas, A.; Martínez, M.; Amador, P.; Torres, L. A., Increasing stability of the fullerenes with the number of carbon atoms: The experimental evidence. *J. Phys. Chem. B* **2007**, *111*, 9031-9035.
169. Cioslowski, J.; Rao, N.; Moncrieff, D., Standard enthalpies of formation of fullerenes and their dependence on structural motifs. *J. Am. Chem. Soc.* **2000**, *122*, 8265-8270.

170. Boese, A. D.; Scuseria, G. E., C2 Fragmentation Energy of C60 Revisited: Theory Disagrees with Most Experiments. *Chem. Phys. Lett.* **1998**, *294*, 233-236.
171. Hansen, K.; Echt, O., Thermionic Emission and Fragmentation of C₆₀. *Phys. Rev. Lett.* **1997**, *78*, 2337-2340.
172. Eckhoff, W. C.; Scuseria, G. E., A Theoretical Study of the C2 Fragmentation Energy of C60 and C70. *Chem. Phys. Lett.* **1993**, *216*, 399-404.
173. Hu, Y. H., Structures, Stabilities, and Equilibrium Contents of C2-Fragmentated C70 Clusters. *Chem. Phys. Lett.* **2008**, *463*, 155-159.
174. Dolgonos, G. A.; Peslherbe, G. H., A Computational Study of the C2 Fragmentation Energy of C80. *Chem. Phys. Lett.* **2004**, *398*, 217-223.
175. Dolgonos, G.; Peslherbe, G., Calculations of the C2 Fragmentation Energies of Higher Fullerenes C80 and C82. *J. Mol. Model.* **2007**, *13*, 981-986.
176. Dolgonos, G. A.; Peslherbe, G. H., The Unimolecular C2 Fragmentation of C82: A Computational Study. *Int. J. Mass spectrom.* **2005**, *241*, 261-269.
177. Díaz-Tendero, S.; Alcamí, M.; Martín, F., Theoretical Study of Ionization Potentials and Dissociation Energies of Cnq+ Fullerenes (N=50–60, Q=0, 1 and 2). *J. Chem. Phys.* **2003**, *119*, 5545-5557.
178. Głuch, K.; Matt-Leubner, S.; Echt, O.; Concina, B.; Scheier, P.; Märk, T. D., High-Resolution Kinetic Energy Release Distributions and Dissociation Energies for Fullerene Ions Cn+, 42 ≤ N ≤ 90. *J. Chem. Phys.* **2004**, *121*, 2137-2143.
179. Merchand, A., Electronic Properties of Doped Carbon. Walker, P. L., Jr., Ed. Marcel Dekker: New York, 1971; p 155.
180. Allardice, D. J.; Walker Jr, P. L., The Effect of Substitutional Boron on the Kinetics of the Carbon-Oxygen Reaction. *Carbon* **1970**, *8*, 375-385.
181. Rodriguez, N. M.; Baker, R. T. K., Fundamental Studies of the Influence of Boron on the Graphite-Oxygen Reaction Using in Situ Electron Microscopy Techniques. *J. Mater. Res.* **1993**, *8*, 1886-1894.
182. Sogabe, T.; Matsuda, T.; Kuroda, K.; Hirohata, Y.; Hino, T.; Yamashina, T., Preparation of B4c-Mixed Graphite by Pressureless Sintering and Its Air Oxidation Behavior. *Carbon* **1995**, *33*, 1783-1788.
183. Way, B.; Dahn, J., The Effect of Boron Substitution in Carbon on the Intercalation of Lithium in Li X (B Z C 1– Z) 6. *J. Electrochem. Soc.* **1994**, *141*, 907-912.
184. Weismiller, M. R.; Duin, A. C. T. v.; Lee, J.; Yetter, R. A., Reaxff Reactive Force Field Development and Applications for Molecular Dynamics Simulations of Ammonia Borane Dehydrogenation and Combustion. *J. Phys. Chem. A* **2010**, *114*, 5485-5492.
185. Weismiller, M. R.; Russo Jr, M. F.; van Duin, A. C. T.; Yetter, R. A., Using Molecular Dynamics Simulations with a Reaxff Reactive Force Field to Develop a Kinetic Mechanism for Ammonia Borane Oxidation. *Proc. Comb. Inst.* **2013**, *34*, 3489-3497.
186. Zhao, Y.; Truhlar, D. G., A Prototype for Graphene Material Simulation: Structures and Interaction Potentials of Coronene Dimers. *J. Phys. Chem. C* **2008**, *112*, 4061-4067.
187. Shirasaki, T.; Derré, A.; Ménétrier, M.; Tressaud, A.; Flandrois, S., Synthesis and Characterization of Boron-Substituted Carbons. *Carbon* **2000**, *38*, 1461-1467.
188. Kendall, R. A.; Dunning, J. T. H.; Harrison, R. J., Electron Affinities of the First-Row Atoms Revisited. Systematic Basis Sets and Wave Functions. *J. Chem. Phys.* **1992**, *96*, 6796-6806.

VITA

Sriram Goverapet Srinivasan

Academic Background

- | | |
|----------------|---|
| 2011 – Present | PhD candidate, Department of Mechanical and Nuclear Engineering,
The Pennsylvania State University, University Park, PA, USA
CGPA: 3.95 |
| 2010 | Master of Science (MS), Department of Mechanical and Nuclear Engineering,
The Pennsylvania State University, PA, USA
CGPA: 3.94 |
| 2008 | Bachelor of Technology (B Tech)
National Institute of Technology, Karnataka, India
Major: Mechanical Engineering
CGPA: 9.58/10 |

Research Experience:

- | | |
|------------------------------------|--|
| 2011 – Present
(PhD ongoing) | Molecular dynamics simulation of the hyperthermal collisions of atomic oxygen with carbon based materials using the ReaxFF reactive force field
Advisor: Dr. Adri C T van Duin, Associate Professor, Department of Mechanical and Nuclear Engineering, The Pennsylvania State University, PA, USA |
| 2013
(Summer Internship) | Extending DFTB method to hydrogen at extreme conditions
Advisor: Dr. Nir Goldman, Staff Scientist, Lawrence Livermore National Laboratory, Livermore, CA, USA |
| 2012
(Summer Internship) | Environment dependent DFTB repulsive potential for carbon at extreme conditions
Advisor: Dr. Nir Goldman, Staff Scientist, Lawrence Livermore National Laboratory, Livermore, CA, USA |
| 2008 – 2010
(Master's Thesis) | Development of a Wet Grid Model for Two – Phase Dispersed Flow Film Boiling Phenomena.
Advisor: Dr. F B Cheung, Professor, Department of Mechanical and Nuclear Engineering, The Pennsylvania State University, PA, USA |
| 2007- 08
(Undergraduate Thesis) | Modeling room air flow phenomenon in mechanically ventilated rooms.
Advisor: Dr. T P Ashok Babu, Head, Mechanical Engineering Department
National Institute of Technology, Karnataka, India |
| 2007
(Summer Project) | Characterization of Inter Wrapper flow in a Fast Breeder Reactor Core.
Advisor: Dr. K Velusamy, Head, Thermal Hydraulics Section,
Indira Gandhi Centre for Atomic Research, Kalpakkam, India |